EFFECT OF RETAINED AUSTENITE TRANSFORMATION ON THE FATIGUE BEHAVIOUR OF ALUMINUM CONTAINING TRIP STEELS

by
PETER I. CHRISTODOULOU

A thesis submitted to the Department of Mechanical Engineering
in conformity with the requirements
for the degree of Doctor of Philosophy

University of Thessaly
Volos, Greece
September, 2017

Examination Committee:

Dr. Alexis Kermanidis (Supervisor), Assistant Professor, Dept. of Mechanical Engineering, University of Thessaly.

Dr. Nikolaos Aravas, Professor, Dept. of Mechanical Engineering, University of Thessaly.

Dr. Spyros Pantelakis, Professor, Dept. of Mechanical Engineering & Aeronautics, University of Patras.

Dr. Spyros Karamanos, Professor, Dept. of Mechanical Engineering, University of Thessaly.

Dr. Michalis Agoras, Assistant Professor, Dept. of Mechanical Engineering, University of Thessaly.

Dr. Antonios Giannakopoulos, Professor, School of Applied Mathematical and Physical Sciences, National Technical University of Athens.

Dr. Paraskevas Papanikos, Associate Professor, Dept. of Product and System Design Engineering, University of Aegean.

Acknowledgements

Foremost, I would like to express my sincere gratitude to my supervisor Assistant Professor A. Kermanidis for the continuous support of my PhD study and research, for his patience, motivation and immense knowledge. His guidance helped me in all the time of research and writing of this thesis.

Besides my supervisor, I would like to thank the rest of my thesis committee, Prof. N. Aravas and Prof. S. Pantelakis for their remarks and suggestions that improved the thesis. I am also particularly grateful to Dr. D. Krizan for the performed magnetization measurements. I would also like to thank for the assistance given by Prof. G.N. Haidemenopoulos, Dr. A. Zervaki and Dr. E. Kamoutsi from the Laboratory of Materials in the Dept. of Mechanical engineering in University of Thessaly.

I am also thankful to my colleagues Dr. A. Tzamtzis, Dr. N. D. Polychronopoulos, Dr. E. Benos and Dr. D. Tsokolis for their help, support and encouragement throughout my studies.

Finally, I must express my very profound gratitude to my family and to K. Tsotsou for providing me with unfailing support and continuous encouragement throughout my years of study and through the process of researching and writing this thesis. This accomplishment would not have been possible without them. Thank you.

Peter I. Christodoulou

EFFECT OF RETAINED AUSTENITE TRANSFORMATION ON THE FATIGUE BEHAVIOUR OF ALUMINUM CONTAINING TRIP STEELS

PETER I. CHRISTODOULOU

University of Thessaly, Department of Mechanical Engineering, 2017

Supervisor: Dr. Alexis Kermanidis, Assistant Professor

Abstract

TRansformation Induced Plasticity (TRIP) steels have been found to offer significant advantages in their mechanical behaviour such as high strength and formability due to a gradual strain hardening mechanism induced by the transformation effect. Their fatigue performance has also been found to be influenced by the TRIP effect, specifically under low cycle fatigue conditions, which are accompanied by cyclic plastic strains assisting retained austenite transformation. Despite the existing research attempts there is still insufficient experimental evidence on the influence of transformation on the mechanical behaviour, specifically under elastic and plastic cyclic strains. In the present Thesis a thorough experimental investigation is carried out to investigate the TRIP effect on the monotonic and cyclic performance of Al-containing TRIP steels. The materials' fatigue behaviour is examined in the Low and High Cycle fatigue regimes and specific attention is given to the fatigue crack initiation problem. The experimental results are supported by measurements of

retained austenite transformation using the saturation magnetization technique. The role of TRIP steel microstructure is considered in the investigation, which includes examination of TRIP steels with differences in heat treatment conditions and/or chemical composition.

The experimental findings suggest that fatigue performance is related to the amount of transformation during cyclic loading and the effect is different under elastic or plastic cyclic straining. Regarding the microstructure, the influence of transformation on mechanical behaviour is mainly related to the particle size of retained austenite and ferrite.

In the second part of the Thesis an analytical approach is developed for the assessment of crack initiation life at the root of a notch under cyclic loading. In the analysis, the localized stress strain field at the tip of the notch is calculated numerically with the use of the finite element method. Consequently, the numerical results are used as input in well established fatigue models, to predict the fatigue cycles for the development of a small crack at the notch root of 250μm length. The analytical results are compared with the experiments to assess the reliability of the method to predict fatigue crack initiation in TRIP steels and the findings are satisfactory.

Table of contents

Chapter 4: Experimental Results

Chapter 5: Estimation of fatigue crack initiation

Nomenclature

A_f : elongation at fracture

A_g : elongation at ultimate tensile strength

b : fatigue strength exponent

c : fatigue ductility exponent

C : parameter of Paris equation

E : Young's modulus

FL : fatigue limit

FL_N : notched fatigue limit

K : strength coefficient

K' : cyclic strength coefficient

K_f : fatigue notch factor

K_{max} : maximum applied stress intensity factor

K_t : elastic stress concentration factor

m : Paris equation exponent

n : strain hardening exponent

n' : cyclic strain hardening exponent

N^* : transition fatigue life

N_f : fatigue life

N_{ini} : number of cycles required for detection of a 250μm crack

q : notch sensitivity factor

r_y : monotonic plastic zone

r_{cy} : cyclic plastic zone

R : stress/strain ratio

Y : geometrical correction factor

α : crack length

α_{in} : initial crack length

α_f : final crack length

$\Delta\sigma$: stress range

$\Delta\varepsilon$: strain range

ε_{ae} : elastic strain amplitude

ε_f' : fatigue ductility coefficient

ε_{ap} : plastic strain amplitude

ε_{atotal} : total strain amplitude

ε_{yy} : normal strain in the loading direction

ε_{zz} : transverse strain

ν : Poisson's ratio

σ : gross section nominal stress

σ_a : stress amplitude

σ_f' : fatigue strength coefficient

σ_{max} : maximum stress

σ_{min} : minimum stress

σ_{UTS} : ultimate tensile strength

σ_{yy} : normal stress in the y direction

σ_{zz} : normal stress in the z direction

$\sigma_{y0.2}$: yield strength (offset 0.2%)

σ_y' : cyclic yield strength

CHAPTER 1

Introduction

1.1 Motivation

Over the last decade, the need for increasing passenger safety, vehicle performance and fuel economy [1] in the automotive industry is growing rapidly. Towards this direction, in the materials sector, the aim is to develop light metallic alloys with attractive mechanical properties, which has led to the rapid development of Advanced High Strength Steels (AHSS) combining superior properties with the ability to produce highly formable structural members.

The multi-phase “TRansformation Induced Plasticity” aided steels, offer high strength and formability which are attractive properties for automotive applications towards a lightweight design structural frame. In the characteristic plot of Fig. 1.1, TRIP steels exhibit a better combination of formability with strength compared to traditional high-strength steels.

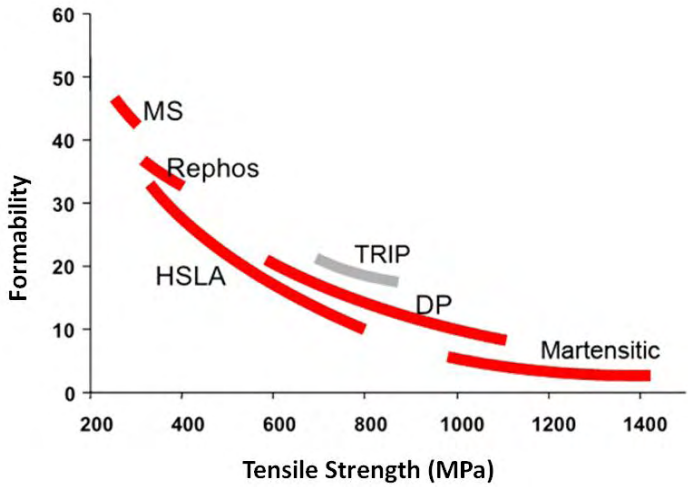

Figure 1.1 Strength - formability balance for TRIP and traditional steels [2].

TRIP steels have a multi-phase microstructure which includes a metastable retained austenite (RA), along with intercritical ferrite and bainitic ferrite. Under deformation the austenite transforms into martensite, which is a stronger phase and the mechanism is associated with energy absorption [3] resulting in a hardening of the material. This hardening effect, combined with the volume increase of the martensite transformation [4-6], delays plastic instability (necking) in the material, resulting in an increase in uniform elongation and ductility (Fig. 1.2), making it suitable for sheet forming procedures. When the austenite transforms during deformation, the resulting microstructure is toughened by the hard martensitic phase. An important parameter related to this transformation is the mechanical stability of RA, which is affected by parameters such as the initial austenite volume fraction, the carbon concentration in the austenite grains and the grain size of RA. Other factors that affect the transformation, are the specific conditions of deformation, such as the strain rate [7, 8], the mode of deformation [9] and the temperature [10, 11].

Because of the increased formability, TRIP steels can be used to produce more complex components than other high strength steels, thus allowing the design of thin metallic parts targeting in weight reduction and optimization of the structural performance.

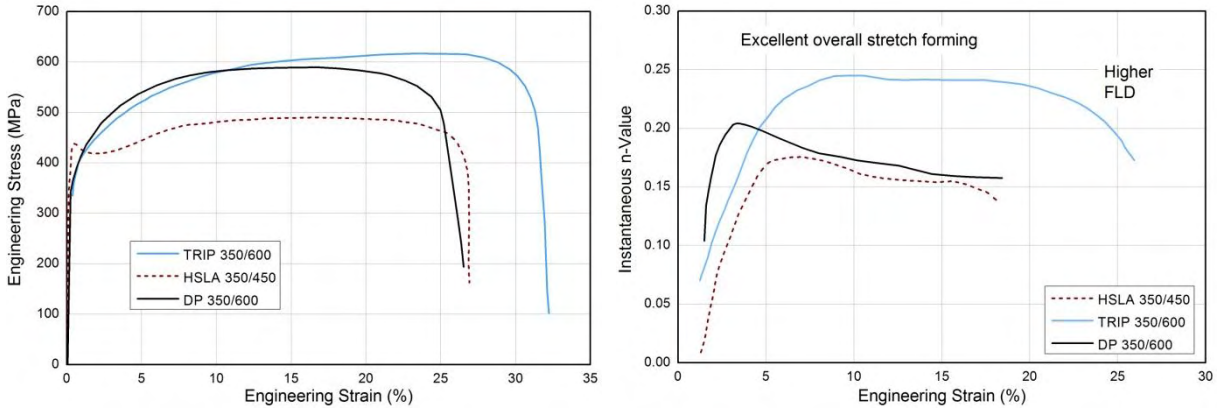

Figure 1.2 Superior mechanical properties of TRIP steels [12].

As a result of their high ductility, energy absorption capacity and strength, TRIP steels are particularly well suited for automotive structural and safety parts such as cross members, longitudinal beams, B-pillar reinforcements, sills and bumper reinforcements [13].

While the development of low alloyed TRIP steels often focuses on microstructural parameters that improve the mechanical strength and ductility, application-wise to expand their potential use to critical structural components is the understanding of the fundamental mechanisms controlling their fatigue behaviour. Specifically, it is important to recognize the role of RA transformation on the cyclic behaviour of TRIP steels, which includes cyclic deformation under elastic and plastic strains as well as fatigue crack initiation aspects. Research efforts on fatigue behaviour of TRIP steels have mainly focused on the Low Cycle Fatigue (LCF) problem, where bulk transformation under plastic cyclic straining is triggered [14-20], while limited are the references concerning the elastic cyclic behaviour of TRIP steels [7, 21-25]. More importantly, a systematic effort to correlate the fatigue behaviour with characteristics of the retained austenite phase and transformation during cyclic deformation is missing. Also, little experimental evidence exists on the fatigue crack initiation behaviour of TRIP steels and how this behaviour is influenced by the transformation effect [26-29].

1.2 Scope of the thesis

The experimental program carried out in the present thesis aims at providing a clearer understanding of the role of RA transformation on the cyclic behaviour of Al-containing TRIP steels. To obtain a wider knowledge of material behaviour, different aspects of mechanical behaviour are examined, which include monotonic material behaviour, cyclic deformation under elastic and plastic strains, notched fatigue behaviour and fatigue crack initiation.

In the second part of the Thesis an analytical methodology is developed for the assessment of fatigue crack initiation. The methodology, which can be applied in notched members to predict the number of cycles for the development of a short crack at the notch root, is compared against experimental results produced in the Thesis to assess its suitability.

The results obtained in the frame of this investigation, provide valuable insights for the mechanical behaviour of Al-containing TRIP steels, regarding the relationship between RA transformation, microstructure and mechanical behaviour.

1.3 Methodology

The dissertation is divided in two main sections. In the first section the experimental program is analyzed and in the second part the analytical methodology for the estimation of fatigue crack initiation life in TRIP steels is developed.

The experimental part of the investigation includes descriptions of the materials, testing procedures and experimental results of the tensile, high cycle (unnotched and notched), low cycle fatigue and fatigue crack initiation experiments. The techniques for material microstructure characterization for the observation and evaluation of microstructural characteristics of the materials are analyzed, along with appropriate non-destructive inspection techniques for fatigue crack growth monitoring.

In the analytical part of the thesis, a methodology for estimation of the fatigue crack initiation life in notched TRIP steel specimens is proposed. The methodology developed, is able to predict the fatigue life required for the formation of a short crack from the notch root of the specimen under mode I type of fracture. For this purpose a numerical model is implemented for the calculation of the local stress-strain response at the notch root during initial loading. The numerical results, which take into account the elastoplastic material behaviour, are incorporated into established notched fatigue models for crack initiation prediction. Apart from the above fatigue analysis, a separate analytical approach based on a fracture mechanics concept is included, for the prediction of fatigue crack initiation. In the final part of the Thesis, the analytical predictions for crack initiation are correlated with the experimental results from the first segment of the dissertation.

A schematic representation of the methodology used and the interactions between the steps in the investigation is shown in Fig. 1.3.

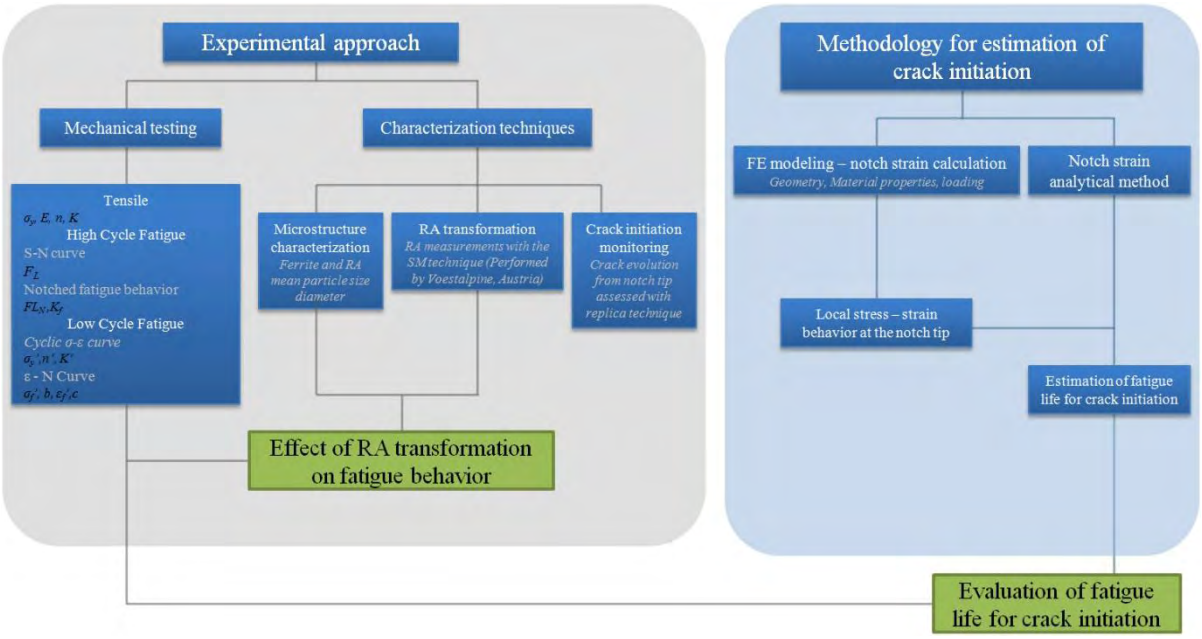

Figure 1.3 Methodology used in the thesis.

1.4 Layout of the dissertation

The dissertation is developed in 6 Chapters. In **Chapter 2** a literature review on TRIP steels is provided, with emphasis paid on the TRIP effect and its influence on mechanical behaviour with respect to the fatigue performance of steels. In **Chapter 3** the details about the materials selection and processing, experimental methodology and characterization techniques are given. The material characterization techniques include metallographic characterization, grain size and aspect ratio measurements with image analysis software and measurements of RA transformation with the saturation magnetization technique. Mechanical testing includes tensile tests, LCF tests, HCF tests in notched and un-notched specimens and fatigue crack initiation tests. The details about crack initiation and growth monitoring, which has been performed with the replica technique, are also discussed here. **Chapter 4** is engaged with the presentation of experimental results and their significance is discussed with respect to existing literature. In **Chapter 5** the analytical concept for fatigue crack initiation assessment of TRIP steels is developed and the analytical results obtained are correlated with the experimental results presented in Chapter 4. The important findings of the investigation as well as suggestions for future work in this field are summarized in **Chapter 6.**

CHAPTER 2

Literature Review

2.1 TRIP steels

2.1.1 Processing and microstructure

TRIP steels, formally referred to as "TRIP-assisted multiphase steels," are materials that contain small volume fractions of RA in a ferrite-bainite matrix in the final microstructure. TRIP steels were first introduced by Matsumura et al. in 1987 [30]. Although in 1970's era Dual Phase steels often contained appreciable quantities of retained austenite and showed some TRIP-like effects, the term TRIP is probably best reserved to steels with intentionally introduced retained austenite, rather than the accidental retained austenite in DP steels.

There are two categories of commercially produced steels that present the TRIP effect. The fully austenitic steels and steels that contain dispersed particles of RA in the microstructure. TRIP steels where the RA is dispersed in a matrix of ferrite and bainite belong in the category of multi-phase TRIP steels, which are of interest in the present study.

To obtain the typical multi-phase TRIP steel microstructure, a two-step heating treatment is required. The heat treatment process consists of intercritical annealing followed by an isothermal bainitic holding and finally quenching to room temperature. The heat treatment procedure and the steel's chemical composition are designed is such a way to promote the formation of carbon enriched austenite, which can be retained in the microstructure when the steel is quenched to room temperature [31] and will be transformed to martensite during straining. A schematic representation of the standard heat treatment procedure in shown in Fig. 2.1.

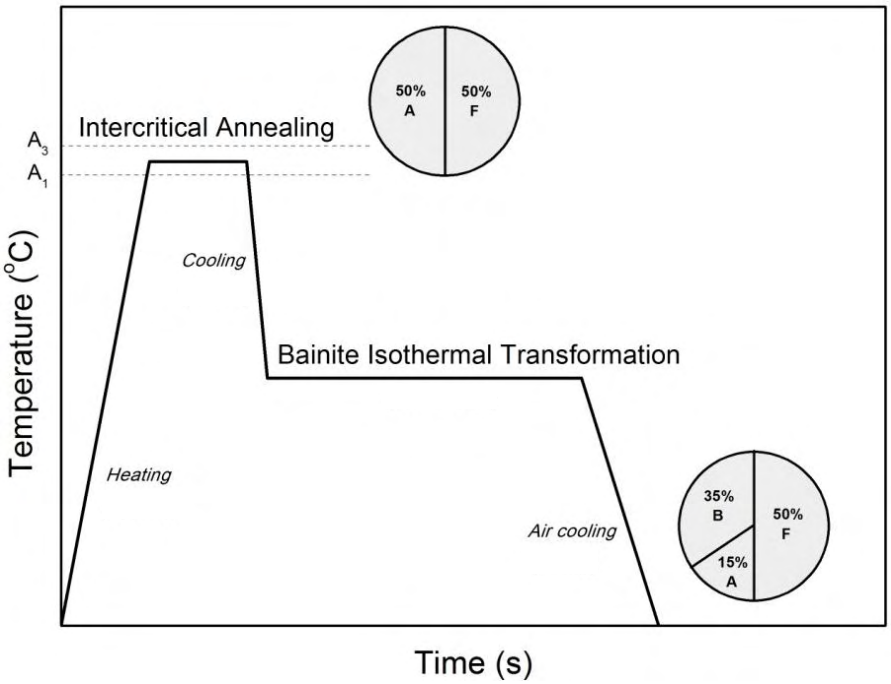

Figure 2.1 Schematic representation of the heat treatment performed for TRIP steels (A:austenite,F:ferrite,B:bainite).

The steel is firstly heated at a temperature range of 700-900^{o}C (in most industrial cases for 3-4 min) where intercritical annealing takes place. The temperature and time of intercritical annealing are chosen in order to result in a mixture of 50% ferrite and 50% austenite in the microstructure. After this step, quenching to an intermediate temperature above the martensite start temperature, M_s, (analyzed in detail in section 2.1.3) is performed, which allows the bainite transformation to occur during isothermal holding. Bainite isothermal transformation (BIT) takes place at a temperature range of 350-450^{o}C for 200-600s

in most cases, leading to the partial transformation of austenite to bainite. The amount of austenite transformed to bainite is strongly influenced by the BIT temperature and time. Therefore, after BIT the steel's microstructure consists of 50% ferrite, 35-45% bainite and 5-15% austenite. In this step, the remaining austenite is further enriched with carbon, which shifts the M_s temperature below the room temperature. However, over-carbon enriched austenite becomes susceptible to cementite precipitation, so an optimum annealing temperature must be found that promotes the best carbon-enrichment levels in the austenite [32, 33]. Finally, the steel is cooled down to room temperature (preferably without austenite transformed to martensite) and the desirable multiphase microstructure with dispersed austenite retained is developed. A typical TRIP microstructure is shown in Fig. 2.2.

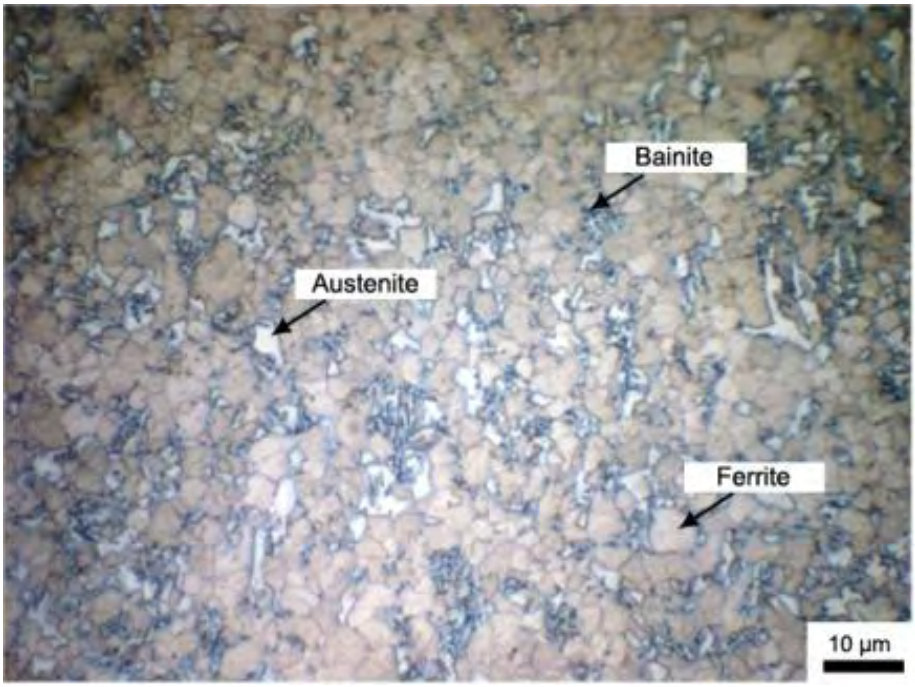

Figure 2.2 Microstructure of TRIP700(A) steel used in the present study.

The alloying elements in TRIP steels play a significant role in the production stages and the resulting mechanical performance [34]. One of the most important alloying elements in TRIP steels is carbon. Carbon acts as an austenite stabilizer, which means that it slows the transformation of austenite to ferrite or bainite [35]. It also slows the transformation to martensite by lowering the M_s temperature and thereby increasing the austenite's thermal

stability. In other words, an increased amount of carbon in the steel would allow for more austenite to be retained in the microstructure. Through alloying, the fraction of retained austenite can be optimized [36] and the precipitation of cementite can be controlled. However, TRIP steels are limited to carbon compositions at or below 0.2wt.% because of weldability issues, as large amounts of carbon make the steel difficult to be welded [37]. Manganese is another austenite stabilizer that is commonly found in all AHSS compositions. It improves the potential for carbon enrichment by increasing the solubility of carbon in the austenite phase and helps to solid-solution strengthen the steel [37].

Other common alloying elements in TRIP steels that act as ferrite stabilizers such as silicon, aluminum, phosphorus and chromium, are generally used to delay carbide precipitation. Traditionally, silicon is used to delay carbide precipitation during the formation of bainite when heat treating. Preventing carbide formation ensures that the carbon is available for stabilizing the remaining austenite [38]. While silicon plays an important role during the processing of TRIP steels, it has detrimental effects on the final product. High levels of silicon lead to poor surface quality on rolled products, which leads to galvanizing problems [39]. To overcome the problems associated with large quantities of silicon [31], new compositions of TRIP steel have been investigated in which silicon is either partially or fully replaced by another element such as aluminum. A general design principle concerning the composition of TRIP steels, where aluminum is partially added with silicon, is based on the formulation: $Si+Al \approx 2wt\%$ in order to suppress the carbide precipitation and shorten the BIT time. While aluminum is insoluble in cementite, it is able to suppress the carbide formation [40]. It also increases the potential maximum carbon concentration that can be reached by increasing the carbon solubility in austenite, thereby further stabilizing the austenitic phase. The most important industrial aspect concerning the addition of aluminum in TRIP steels, is that it offers the advantage of non-forming surface oxides, hence improving the coatability

and galvanizing properties [41], resulting in a significant improvement of structural life of the component.

2.1.2 Applications

The development of high strength steels for the automotive industry is motivated by the need to reduce vehicle weight in order to improve fuel efficiency while continually improving the passengers' safety. The incremental usage of TRIP steels in the chassis of the vehicle (Fig. 2.3), may assist in the production of lightweight car structures and make them competitive materials with regard to new aluminum alloys for use in automotive industry. The reason is that TRIP steels have been shown to have excellent balance of strength-ductility. Their excellent formability and strength properties [42, 43] allow the design of components with complex geometries of reduced thickness, retaining the required strength properties. Moreover they are well suited for the design of structural parts containing geometrical discontinuities which act as stress raisers.

Regarding the fatigue performance, TRIP steels exhibit high cyclic yield strength along with high fatigue limit values. Their superior fatigue performance compared to other conventional high strength steels (Fig. 2.4), may be partly attributed to the TRIP effect, and makes them potential attractive materials for highly stressed components subjected to cyclic loading. Nevertheless their fatigue resistance potential is not yet fully exploited and the present Thesis aims to contribute on this area.

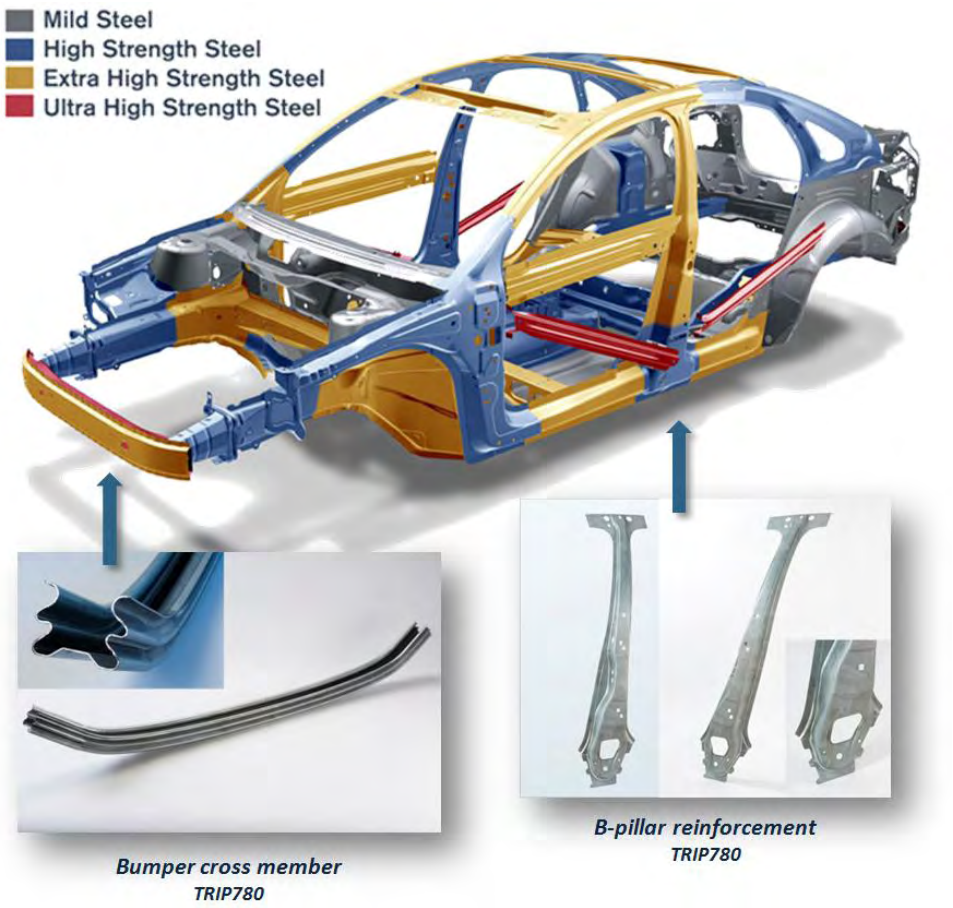

Figure 2.3 TRIP steels in automotive industry.

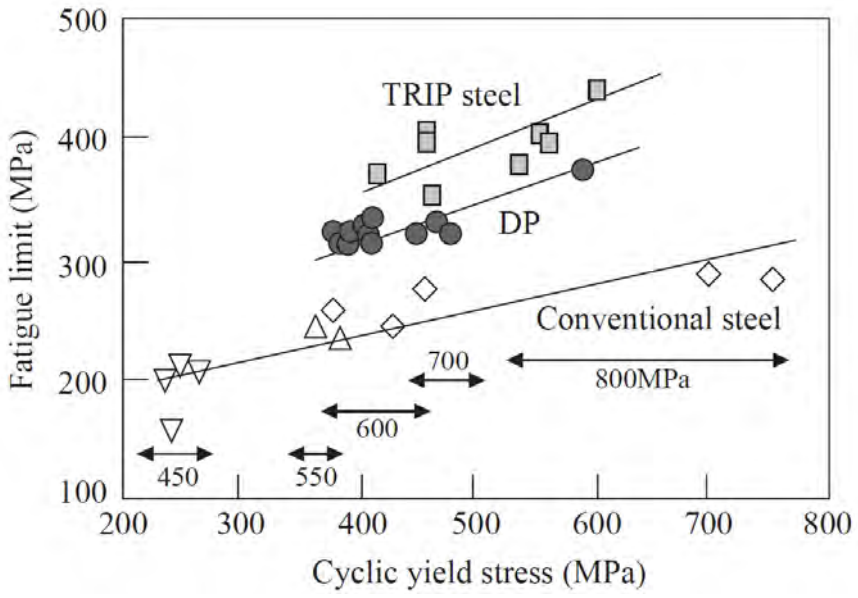

Figure 2.4 Effect of cyclic yield stress on fatigue limit of advanced high strength steels [44].

2.1.3 TRIP effect

The unique properties of TRIP steels are attributed to the RA transformation, a phenomenon known as the TRIP effect. Transformation of the metastable austenitic phase into the hard and brittle martensitic phase is a result of applied stress or strain [45-48], which makes the TRIP steel behave like a unique type of smart material by adjusting its mechanical behaviour during straining.

It is useful here to describe the conditions influencing the martensitic nucleation process under elastic stresses or plastic strains. As indicated schematically in Fig. 2.5, application of a stress not far above the M_s and below the M_s^{σ} temperature can include martensitic nucleation even though the stress may be well below the normal yield strength of the austenitic phase. This transformation is called *stress-assisted* because the existing nucleation sites are simply aided mechanically by the thermodynamic contribution of the applied stress. In other words, the critical driving force for nucleating the sites that normally operate without any external stress at M_s can be attained at temperatures above M_s since the mechanical driving force makes up for the reduced chemical driving force at such higher temperatures. Due to this interrelationship, the higher the temperature stress-induced nucleation requires higher stresses, in accordance with the slope of line AC in Fig. 2.5. It may be mentioned that the transformational- mechanical interactions described above are representative of athermal kinetics. For isothermal kinetics the corresponding effects of elastic stress and plastic strain are described by line A'B.

At a temperature designated as M_s^{σ} , the stress required for nucleation reaches the yield strength of the austenitic phase. Above M_s^{σ} significant plastic flow precedes the transformation, and an additional contribution to transformation can arise from the creation of new and more potent nucleating sites accompanied by plastic deformation. This transformation is defined as *strain-induced*. Under these conditions, the nucleating stresses at

temperatures above M_s^{σ} do not fall on the extension of line AC, but rather along the line CD. The temperature M_s^{σ} thus defines an approximate boundary between the temperature regimes where the two modes of nucleation dominate, while near M_s^{σ} both modes will operate. M_d is the temperature above which the chemical driving force becomes so small that nucleation cannot be mechanically induced, even in the plastic strain regime. Often there is an overlap between the stress-assisted and strain-induced temperature ranges, and so the temperature may not be defined sharply. The line ACE designates the stress temperature conditions where the TRIP phenomenon takes place.

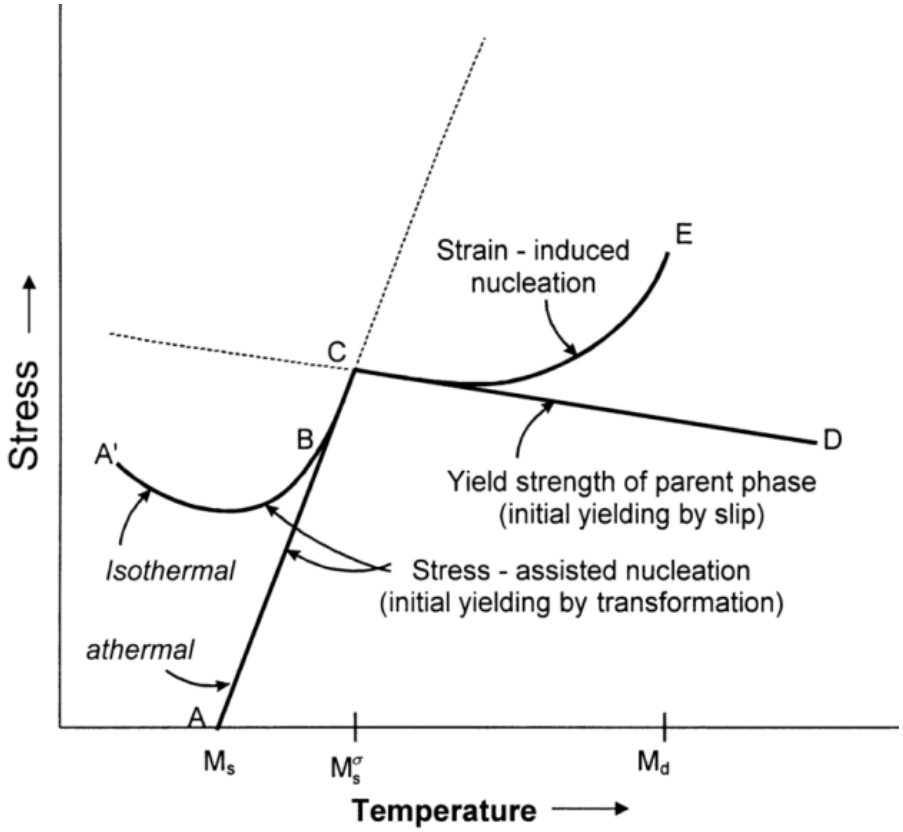

Figure 2.5 Schematic representation of the interrelationships between stress-assisted and strain-induced transformation.

2.1.3.1 Stability of retained Austenite

In general by controlling the morphology, distribution, and stability of the RA, the mechanical properties of the TRIP-assisted steels can be improved to achieve both high strength and high ductility [49-52].

The stability of RA refers to its resistance to transformation with stress, strain and temperature, so that for a given temperature more stable retained austenite will transform to martensite at higher stresses and strains. The RA can also be thermally decomposed into martensite (thermodynamically more stable phase) as a consequence of temperature changes, which is referred to as the thermal stability of RA. The rate at which RA transforms during deformation influences the mechanical behaviour of TRIP steels. An "optimum" stability of austenite may contribute to a gradual strain hardening during straining, thus shifting the necking effect to high uniform elongation values, promoting formability [53]. If the austenite is too stable it will not transform during deformation and thus it will not contribute to the TRIP effect. If the austenite is very unstable it will transform at very low strains and the TRIP effect will be triggered too early to contribute to the delay of necking. Consequently, the RA stability should be such that it transforms progressively during deformation, so that damage can be accommodated at all stages of deformation. According to Reisner et al. [54] for the transformation of austenite to martensite, carbon determines the chemical driving force stress-free transformation strain (via its influence on the lattice parameter) and the flow behaviour of the retained austenite.

As mentioned earlier the most important alloying element affecting the stabilization of RA is carbon which delays the transformation to martensite on cooling, by lowering the M_s temperature [35], while at the same time an increase of the carbon content increases the obtainable amount of RA [55] in the final microstructure. Besides the carbon content, austenite stability is also affected by the RA size [46, 56], where fine RA grain size is found to increase its stability. The effects of RA grain size can be attributed to the probability of martensitic nucleation and the energy barrier to the growth of martensite. Fine RA grains possess fewer pre-existing martensite nucleating sites and therefore a lower probability of transformation. This is due to the absence of substructures in the austenite, for example

stacking faults and other defects that provide nucleation sites for martensitic transformation [15, 57]. RA in TRIP-assisted steels can be found in two forms, isolated austenite grains in ferrite away from the bainitic phase and films of austenite in-between bainitic ferrite plates. The latter type of austenite is generally observed to be more stable during deformation than the former types [58-60]. It is thus thought that isolated small austenite grains dispersed in ferrite actually contribute to the TRIP effect.

The shape of RA grains and the interaction between the phases in the microstructure is another factor affecting the RA stability [61]. Ultrafine RA lamellae grains have been found very beneficial for a steady and gradual martensitic transformation, retarding the initiation of local strain concentrations, hence providing a continuous work-hardening effect, while on contrary the blocky type RA grains may play a significant role for the initiation of voids and cracks, due to the low stability facilitating an abrupt transformation of RA into martensite [49]. The higher RA stability for the lamellar microstructure of an Al-containing TRIP steel examined in [62] is primarily due to the stress shielding effect of RA grains by the surrounding bainite while a secondary contributing factor in the enhanced RA stability was the elongated shape of the RA grains.

Besides the RA microstructural characteristics and the carbon content, the austenite to martensite transformation is also strongly affected by deformation mode [63, 64], stress state [65] and strain rate [7]. Unlike uniaxial tension or compression, deformation-induced martensitic transformation is always known to be suppressed by hydrostatic pressure. The stability of RA can therefore be enhanced by applying hydrostatic pressure during tensile test, resulting in higher uniform elongation [9]. This may be an important aspect in hydro-forming operations where the RA in the microstructure in such a case would not be fully transformed during forming, thereby allowing the TRIP effect to be utilized for crash-worthiness in finished components.

Moreover, at a macroscopic level, the hardening of TRIP steels significantly depends on the stress state. The transformation behaviour of RA under different deformation modes for low alloyed TRIP steels was examined in [66]. It was demonstrated that the strain-induced martensitic transformation is promoted under plain-strain and biaxial conditions relative to uniaxial loading. Furthermore, faster transformation rates -corresponding to higher hardening levels at smaller strains, were obtained for stress states at an intermediate stage between uniaxial and biaxial tension in [63]. In [67] it has been proposed that by a properly adjustment of the stability of RA with respect to the stress state that will be present in the forming application, a remarkable strength/ductility balance can be attained.

2.2 TRIP effect and mechanical behaviour

2.2.1 Monotonic behaviour

The plasticity that accompanies martensitic transformation in the presence of applied stress has been found to influence the mechanical behaviour of the material. The effect is mainly influenced by the amount of retained austenite and its stability controlling the amount of transformation, which amongst other factors, depends mainly on the carbon content [68]. In [34], the strength-ductility balance was found to increase with the amount of RA and its carbon content. Important aspects influenced by the stability of retained austenite are the strain hardening behaviour and the onset of necking, which are significant parameters controlling the formability of the material. In [31] it was demonstrated that the uniform elongation, a mechanical property related to the onset of necking, is dependent on the strain-induced transformation of retained austenite to martensite. Also as it has been shown in [3] the work-hardening capacity of the steel can be improved due to the energy absorbed during transformation. In [31, 37, 69] it was found that the TRIP effect was responsible for generating new sources of dislocations through the dilatational deformation in the surrounding

ferritic matrix, increasing the strain hardening capacity during straining and finally provoking higher uniform and total elongation to the material. Furthermore, work-hardening rate is directly compared with the volume fraction of retained austenite [56]. Confirming the above influences on the material behaviour, in [24] it has been shown that increased austenite stability is associated with a progressive strain hardening behaviour during plastic deformation and a delay of onset of necking in Al-containing TRIP steels.

To summarize, the strain-induced transformation of retained austenite has been considered to be a significant factor influencing the mechanical performance and a moderately stable austenite appears to be the key to optimize ductility [42] along with chemical composition aspects such as carbon content, which influences retained austenite stability controlling the mechanical performance [70].

2.2.2 Low cycle fatigue behaviour

Under cyclic loading, the austenite to martensite transformation has been found to influence the material's performance especially under LCF conditions, where strain induced transformation occurs under cyclic plastic strains. In numerous studies it has been reported that when the plastic strain component is dominant the TRIP effect influences the fatigue behaviour [7, 14, 16-20, 28, 71-79].

Regarding the transformation mechanism, in [77] it has been found that the formation of martensite at a given plastic strain amplitude leads to a substantial cyclic hardening and to a decrease of the fatigue life of a stainless steel. The above result confirms the findings of a previous work of Franke et al. [80], where the austenitic stainless steels which exhibited high amounts of transformation demonstrated inferior fatigue life compared to steels with less transformation potential. Fatigue life has been shown to be dependent also on the volume fraction of RA. In [28] high levels of retained austenite lead to an increase in fatigue life, due

to a delay in crack initiation and the retardation of crack propagation, both resulting from the strain-induced transformation of austenite to martensite.

With regard to the cyclic hardening/softening behavior of TRIP steels there are mixed results reported in literature depending on the material. In the austenitic cast TRIP steels examined in [17] it was found that with increasing strain amplitude the amount of martensite inside the deformation bands increases, resulting in significant cyclic hardening, and in a recent study performed by Ackermann et al. [72] the pronounced cyclic hardening observed was found to be dependent on the martensite formation rate and dependent on the plastic strain amplitude.

In several of the aforementioned studies [14, 16, 79] it was reported that cyclic hardening or softening phenomena in TRIP steels, are not necessarily related to the strain induced austenite to martensite transformation. The TRIP590 and TRIP980 steels were examined in [14] and showed initial cyclic hardening followed by cyclic softening until failure at various strain amplitudes. It was concluded that the high initial cyclic hardening with increasing strain amplitude observed in TRIP980 despite the lack of austenite transformation may be attributed to the larger ferrite size compared to other TRIP materials. In the TRIP780 steel, initial cyclic hardening also occurred and was followed by cyclic softening during further fatigue loading at higher strain amplitudes. However, at lower strain amplitudes, cyclic softening occurred from the very first cycle up to failure. In [18] the non aluminum TRIP590 steel exhibited increasing cyclic hardening for strain amplitudes 0.2% - 0.25% followed by a cyclic stable behaviour for strain amplitudes of 0.3% - 0.4%, while cyclic softening occurred at strain amplitudes above 0.4%. This cyclic softening at higher strain amplitudes has been attributed to the relaxation of local internal stress due to the transformation of retained austenite to martensite. A similar behaviour was observed in [79] for a TRIP780 steel, but with cyclic softening diminishing with decreasing strain amplitude.

In [19, 20] it was demonstrated that the martensite volume fraction increases and the rate of phase transformation decreases with increasing number of fatigue cycles while the strain-induced transformation of retained austenite to martensite contributes to initial cyclic hardening, but almost having no effect on the subsequent cyclic stable/softening behavior. The strain-induced martensitic transformation generated during fatigue loading was considered to contribute to initial cyclic hardening in [5, 14, 16, 79, 81].

The role of dislocations density and mobility has also an immediate effect on the cyclic hardening of TRIP steels. The formation and spreading of dislocation sources were assumed to be the major cause for the initial cyclic softening, whereas cyclic softening after the initial cyclic hardening was presumed to be due to the decreased dislocation density and the re-arrangement of dislocations in [14, 16, 79]. Expanding the latter studies, Zhou et al. in [71] concluded that the major cause for the initial cyclic hardening was neither the strain-induced martensitic transformation nor the increase in dislocation density but the initial high density of dislocations, which were pre-existent and mobile in the initial microstructure.

The proximity of the phases has been also considered to influence the cyclic behavior of TRIP steels. Sugimoto et al. in [82-84], examined the effect of microstructure on the fatigue properties of TRIP-aided steels and concluded that the cyclic behaviour was controlled not only by the RA characteristics and the matrix microstructure, but also by the long range internal stresses arising from the difference in flow stress between matrix and the other phases.

By examining the above literature results it is obvious that the transformation effect is significant for the LCF behavior of TRIP steels, but interactive mechanisms such as the RA transformation, the martensite as the product of the transformation, the interaction/proximity of constituting phases and the dislocation density and mobility are also influencing the

material performance. In the present study it is attempted to provide a better understanding of the role of RA transformation on the cyclic hardening/softening of the TRIP steels examined.

2.2.3 High cycle fatigue behaviour

The High Cycle Fatigue (HCF) performance of TRIP steels has received limited attention due to the predominantly elastic cyclic behaviour which does not promote bulk transformation. Nevertheless, deformation induced transformation which occurs in microstructural scale, still takes place and has been found to result in an improvement of fatigue strength [24, 25, 85]. In a work of Yokoi et al. [21] it was demonstrated that the presence of RA in the microstructure can enhance the fatigue properties of TRIP steels. It was shown that a TRIP steel containing 10% initial volume fraction of RA exhibited higher fatigue resistance compared with conventional HSLA and DP steels, effect which might be attributed to the compressive residual stress in the surface region caused by the austenite-to-martensite transformation retarding the propagation of the nucleated micro-cracks.

Haidemenopoulos et al. [24] examined the effect of austenite stability on HCF of low alloyed Al-containing TRIP steels with same chemical composition but different initial RA content and stability. Their findings suggested that the RA stability is a significant parameter affecting the fatigue performance of TRIP steels especially at high cyclic stresses. Furthermore, it was demonstrated that under elastic alternating stresses the transformation effect still exists and fatigue limit values close to the material's yield strength have been reported. Experimental evidence of fatigue limit values close or above the materials' yield strength has also been reported in other investigations [22, 86].

In [87] the high fatigue limit of a quenched and partitioned TRIP steel was attributed to a delay in crack propagation caused by phase transformation, while the fatigue strength was found to be dependent on the initial RA volume fraction. Similar observations were reported in [88], where it was shown that the transformation of RA to martensite is triggered ahead of

the fatigue crack tip, leading to a delay in fatigue crack growth, which is directly related to high endurance limit value.

Another study that associates the improvement of fatigue limit by the increasing volume fraction of RA was performed by Abareshi et al. [23]. During the fatigue loading, stress-induced phase transformation of retained austenite to martensite takes place ahead of the crack tip and affects the propagation of crack. SEM observations revealed that when the crack tip approaches a hard martensitic phase, it changes its direction towards a neighboring ferrite grain. This repeating process was found to be the key for the increased fatigue life. Hence, higher amounts of RA create more barriers for fatigue crack growth and therefore fatigue life can be improved, which has been possibly attributed to the formation of very fine martensite particles in the area of local plasticity in adjacent of crack, which effectively block the dislocation motion [89].

Similar to this, Roth et al. [90] examined the influence of RA transformation of a metastable stainless steel in the high cycle fatigue regime. Their work demonstrated that while the martensite formation results in an increase of the specific volume and gives rise to compressive stresses, that leads to premature contact of the crack surfaces and hence to a retardation of the short crack growth.

2.2.4 Crack initiation and propagation

Another significant fatigue problem associated with the design of structural components is the material's fatigue crack initiation resistance. At locations with stress concentrations (e.g. holes, notches), the local material behaviour at the notch tip controls the onset of cracking, while local plasticity at the root of the geometrical discontinuity will favor RA transformation influencing fatigue behaviour. These issues have received limited research attention and most investigations focus on the notch effect on fatigue limit. In [4, 22], it has been reported that the formation of hard martensite due to strain induced transformation, suppresses the crack

initiation and growth in TRIP steels. In [86] the notched fatigue limit of TRIP-aided bainitic ferrite steels with 10-13.7% initial RA volume fraction increased with increasing hardness, while the notch sensitivity decreased. Retained austenite to martensite transformation has been also found to be beneficial on the rate of the growing crack. In [88, 91] the transformation ahead of the crack tip was found to reduce the energy absorption leading to high fatigue crack growth resistance in a low alloy TRIP steel.

The above studies suggest that austenite transformation influences the fatigue behaviour of TRIP steels, however a quantitative and qualitative assessment of its contribution under high and low cycle fatigue conditions is missing.

For this purpose the LCF and HCF performance is correlated in the present Thesis with the amount of martensitic transformation during straining for different Al-containing TRIP steels with slight variations in chemical composition and microstructural characteristics. The results present useful insight on the contribution of RA transformation on mechanical behavior under different loading conditions.

CHAPTER 3

Experimental Program

In this chapter the experimental methodology is presented, with description of the TRIP materials and their microstructures, experimental procedures for the static and fatigue experiments, and techniques used for the RA measurements and crack initiation monitoring.

3.1 Materials

The materials used in the investigation are Al-containing low alloy TRIP steel sheets, with chemical composition, condition and thickness given in Table 3.1.

Table 3.1 State and chemical composition (wt.-%) of TRIP steels.

Steel	Condition	Thickness (mm)	C	Mn	Al	Si	P
TRP700(A)	Hot rolled	1.75	0.18	1.61	1.45	0.7	-
TRIP700(B)	Cold-rolled	1.45	0.202	1.99	1.07	0.35	0.009
TRIP(HT2I) TRIP(HT3I)	Cold-rolled	0.72	0.2	1.8	1.33	0.04	0.016
TRIP(HT2D) TRIP(HT3D)	Cold-rolled	0.72	0.246	1.73	1.43	0.036	0.013

TRIP700(A) steel sheet was received in hot rolled condition while TRIP700(B) steel sheet in cold rolled condition. The HT steels with minimal differences in chemical composition were received as cold rolled steel sheets after being treated by a two stepped heat treatment process consisting of two different heating schedules for each material. In that way, four different TRIP materials were produced. Specifically, TRIP(HT2I) and (HT2D) steels were annealed at 890^{o}C for 60s and subsequently cooled down to 400^{o}C and held for 420s, while TRIP(HT3I) and (HT3D) steels were annealed at 890^{o}C for 60s and subsequently cooled down to 460^{o}C and held for 120s.

The percentage vol.-% RA values in as-received condition were measured using the saturation magnetization (SM) technique, which is described in more detail in section 3.2.2. Three SM measurements from each material in as-received condition were performed and the averaged values of the vol.-% initial RA content are shown in Table 3.2.

Table 3.2 Initial RA volume fraction (vol.-%).

Steel	**(%)**
TRP700(A)	11.8
TRIP700(B)	15.8
TRIP(HT2I)	11.2
TRIP(HT3I)	14.3
TRIP(HT2D)	13.5
TRIP(HT3D)	13.8

3.2 Material characterization techniques

An extensive analysis of the constituting phases was performed in order to assess the characteristics of TRIP microstructures. To this end, the basic microstructural characteristics were evaluated with standard optical microscopy and further examination with image analysis software. Moreover, the retained austenite volume fraction was measured with the SM technique. The SM measurements were performed in the steel division department of

Voestalpine in Austria. A brief description of the performed techniques is presented in the following sections.

3.2.1 Microstructure evolution

3.2.1.1 Etching solution and procedure

The materials' microstructures in as-received condition were assessed using optical microscopy. Small samples were cut using a high precision cutter to ensure that minimal deformation occurred during the cutting process and standard metallographic techniques of grinding and polishing were applied.

The samples were first mounted in bakelite using a mounting press. The mounted samples were then grinded successively using finer grits of silicon carbide paper, starting with #120 grit and finishing with #2400 grit. Diamond polish was then used to polish the samples' surface starting with 3μm diameter diamond particles, followed by 1μm. Consecutively, a stepped color tint-etching procedure was employed using the De- etching method [92] in order to reveal the steels' microstructures. The samples were first dipped into a 3% Nital solution for 3-4s and then placed into a solution of 10% $Na_2S_2O_5$ for 60s. After etching in both solutions, they were immediately washed with water, immersed in ethanol and then were blown dry in hot air. Optical microscopy was used to obtain a representative picture of the microstructure. The mounted samples were re-polished with 3μm-1μm diamond pastes and re-etched. With this process multiple images at different sections (through thickness) were produced and examined.

The results obtained with the tint etching technique are very sensitive to the composition of the steel and etching agents as well as the etching time. Despite the sensitivity of the method to the above parameters, the color etching technique produces a reliable result of the different micro-constituents. A disadvantage of the method is that when these or similar

etching techniques are used, the RA and martensite cannot be separated as they both appear in white. The use of an improved etching technique (tint etching after tempering) to reveal the existence of martensite in the multiphase steels proposed in [93], did not give satisfactory results because of its extreme sensitivity to the etching time in the second etching agent, leading not only to excessive tinting of the martensite but also to the darkening of the ferrite. Because of the complexity in revealing the martensitic phase in the microstructure, it is assumed that the steels examined did not contain martensite in as-received condition.

3.2.1.2 Quantitative image analysis

The ferrite and retained austenite grain characteristics were determined using an image analysis software with data taken from several micrographs at different depths of the sample to avoid estimation errors due to the large dispersion of the phases. The grain characteristics examined include the average grain size diameter as well as the aspect ratio of the measured grains.

The micrographs from each material were processed with a photo editing software to create a binary image with isolated grains (phase mapping). Then, the phase mapped images were examined with the Image-Pro Plus5 software and the average grain size of austenite and ferrite was measured. To increase the accuracy of measurements the average grain diameter measured at 2 degree intervals passing through the particle's centroid was calculated. This method is recommended in cases where high grain shape irregularity exists in the structure [94].

Another grain characteristic of TRIP steels measured is the grain aspect ratio ($A_r=d_{min}/d_{max}$). The aspect ratio, as a shape factor, is a dimensionless quantity used to describe the shape of a particle, independent of its size. The normalized aspect ratio ranges from approaching zero value for elongated particles, to near unity for equiaxed grains.

Approximately 2000 retained austenite and 200 ferrite grains from each material were used for the quantification of the above microstructural characteristics.

3.2.2 Saturation magnetization method (SM)

The SM measuring equipment is depicted schematically in Fig. 3.1. It consists of a magnetic yoke, which produces a high and homogeneous magnetic field between its poles. A magnetic flux sensing coil mounted in the centre of this magnetic field is used as the measurement coil. The specimen used for measurement is positioned through the measurement coil with its axis aligned to the direction of magnetic field. The amount of retained austenite is calculated from the measured integral of the voltage pulse induced in the coil [95].

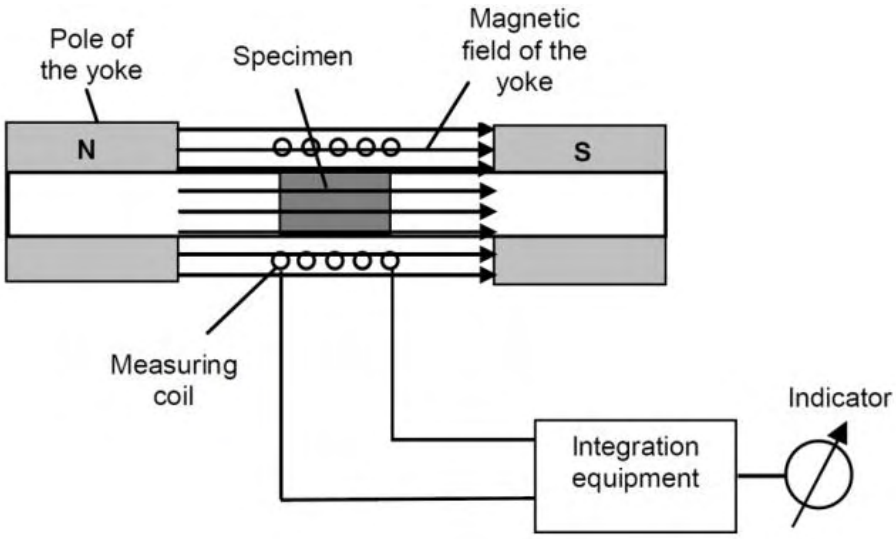

Figure 3.1 Schematic representation of the SM method.

Ferrite and austenite differ in their magnetic behaviour, with ferrite being ferromagnetic and austenite paramagnetic. For this reason, only the amount of ferrite of the sample contributes to the induced voltage pulse in the measurement coil. The saturation magnetization decreases with arising amount of austenite, which cannot be magnetized in the case of a two phase mixture of ferrite and austenite. The addition of alloying elements also causes a change of the saturation magnetization. The volume fraction of retained austenite was calculated as follows:

$$V_g = \frac{\left[J_S^{Fe} - \sum_n (\alpha_n A_n) \right] - J_m}{J_S^{Fe} - \sum_n (\alpha_n A_n)} 100\% \quad (1)$$

where α_n and A_n (in vol.-%) are related to the effect of the alloying element n on the saturation magnetization in the specimen. J_s^{Fe} represents the saturation magnetization of the pure ferrite and J_m is the saturation magnetization of the specimen calculated based on the following formula:

$$J_m = \frac{\int U_{ind} dt}{\frac{N}{L} V} \quad (2)$$

where U_{ind} is a voltage-pulse in the coil, V is the volume of the specimen, N, the number of windings of the pick up coil, and L, the length of the measured coil.

This method has the advantage that the entire volume of the sample can be measured. The method shows higher precision compared to other methods [49] for determination of RA volume fraction and exhibits good repeatability in the performed measurements [95]. Small uncertainties may exist due to the presence of alloying elements, which can cause a small change of the saturation magnetization. Despite its advantages, certain scatter in RA volume fraction measurements, should always be taken into consideration.

3.2.3.1 Sampling of specimens

The initial RA volume fraction was measured from small samples with dimensions 14mmx3.5mm, which were extracted from the bulk (as-received) material, using the SM technique. In order to account for possible scatter in the results, three samples from each material were measured and the values presented in Table 3.2 are averaged. To evaluated the %RA transformed, the initial measured value of the bulk material was used and correlated with each value measured from the different loading condition, as:

$$\%RA_{transformed} = \frac{initial(vol.-\%) - final(vol.-\%)}{initial(vol.-\%)} x100$$

The vol.- %RA transformation was measured from samples extracted from the gauge area of the tensile specimen after fracture (Fig. 3.2(c)). In similar manner, retained austenite transformation under cyclic loading was evaluated by performing RA measurements on small samples extracted from the fatigue specimens after failure. The specimen location where the samples have been extracted from was adjacent to the fracture area as shown in Figs. 3.2(a) and (b). Samples were extracted approximately 2 mm away from the fracture location, inside the gauge section of the specimen, to avoid additional transformation effects caused by localized plastic deformation due to necking. In the specimens with continuous radius of curvature, the non uniform distribution of stresses inside the gauge section in the longitudinal axis of the sample, was taken into account for the calculation of average stress values along the axis at the position of the extracted sample.

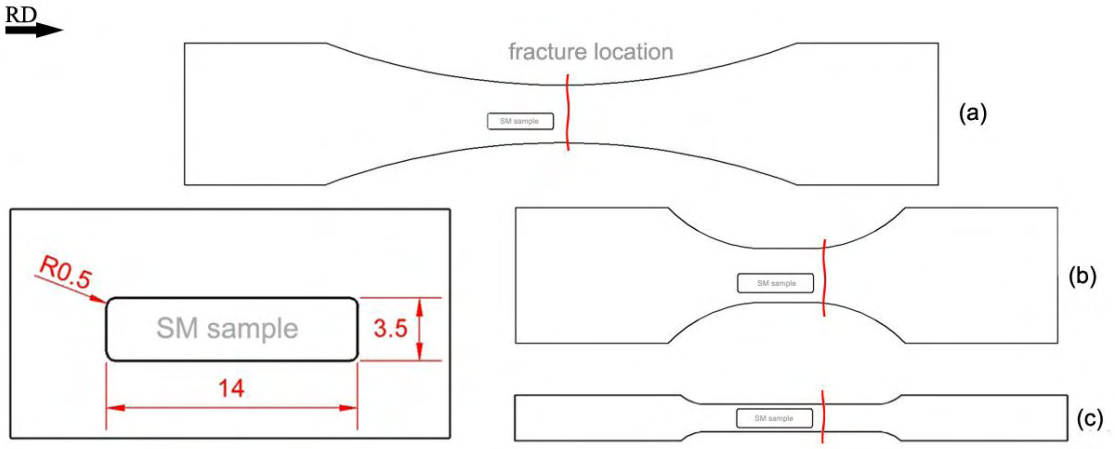

Figure 3.2 Location of extracted sample for RA measurements in (a) HCF, (b) LCF, (c) tensile test specimen (dimensions in mm).

3.3 Mechanical Testing

The mechanical behaviour of the TRIP materials was evaluated under tensile and fatigue testing. The complete experimental program, including the different types of testing and associated RA measurements is presented in Table 3.3.

Table 3.3 Type of mechanical tests and RA measurements performed for each material.

Steel	Mechanical testing					RA measurements		
	Tensile	HCF	LCF	HCF_{notch}	Crack initiation monitoring	Tensile *(at fracture)*	HCF conditions	LCF conditions
TRIP700(A)	●	●	●	●	●	●	●	●
TRIP700(B)	●	●	●	●	●	●	●	●
TRIP(HT2I)	●	○	●		●	●	○	●
TRIP(HT3I)	●	○	●		●	●	○	●
TRIP(HT2D)	●		●			●		
TRIP(HT3D)	●		●			●		

○ Results taken from [24]

3.3.1 Tensile testing

Uniaxial tensile tests were conducted to determine the mechanical properties of the TRIP steels. The tensile tests were carried out using an INSTRON 8801 servo-hydraulic machine with 100 kN load capacity. Mechanical properties were determined in accordance with ASTM E8M at a constant crosshead velocity of 0.5 mm/min. The specimens were tested in the longitudinal (L) direction using a 25- mm gage length clip-on extensometer. The geometry of the specimen used for the tensile tests is depicted in Fig. 3.3.

The strain hardening exponent (n) and the strength coefficient (K) were assessed using the Ramberg–Osgood equation [96]:

$$\varepsilon = \frac{\sigma}{E} + \left(\frac{\sigma}{K}\right)^{1/n} \tag{3}$$

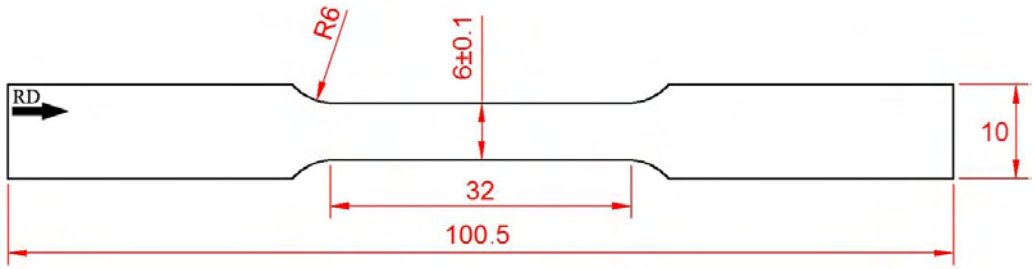

Figure 3.3 Sub-size specimen configuration according to specification ASTM E8M (dimensions in mm).

3.3.2 Fatigue testing

3.3.2.1 Strain controlled fatigue tests

Fully reversed (R= -1) cyclic tests were performed in accordance with SEP 1240 [97] specification. Strain amplitudes in the range of 0.002 - 0.02 were applied using a 10- mm gage length clip-on extensometer at a frequency range of 0.1 - 3 s^{-1}. The specimens were tested in the longitudinal (L) direction. To prevent buckling during testing, an anti-buckling device from ultra high strength steel (compressive strength >1000MPa) was designed (Fig. 3.4), constructed and attached to the specimen surfaces (Fig. 3.5). The geometry of the LCF specimen used is shown in Fig. 3.6.

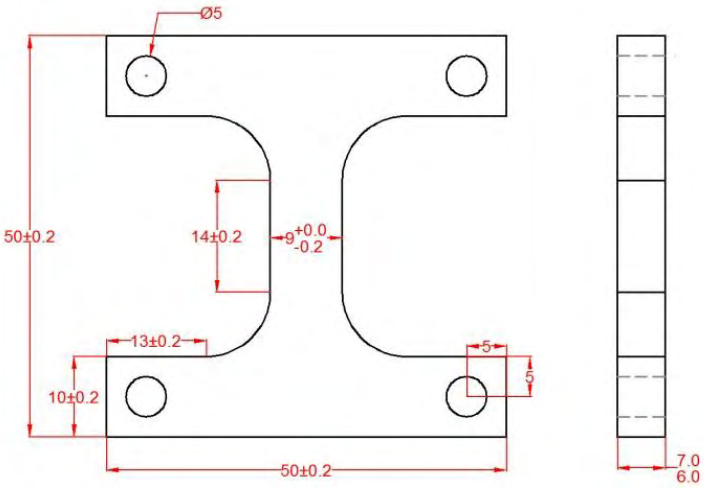

Figure 3.4 Anti-buckling device used in LCF tests (dimensions in mm).

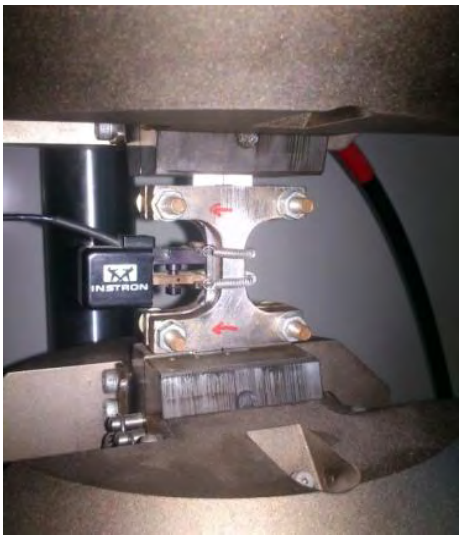

Figure 3.5 Strain controlled fatigue test setup with the use of anti-buckling device.

The stabilized hysteresis loop was determined from the half number of cycles required for onset of crack initiation. Crack initiation corresponds to the number of cycles where a 10% change of the maximum cyclic load [97] is observed. For determining the total fatigue life N_f, as failure criterion the final fracture of the specimen was considered.

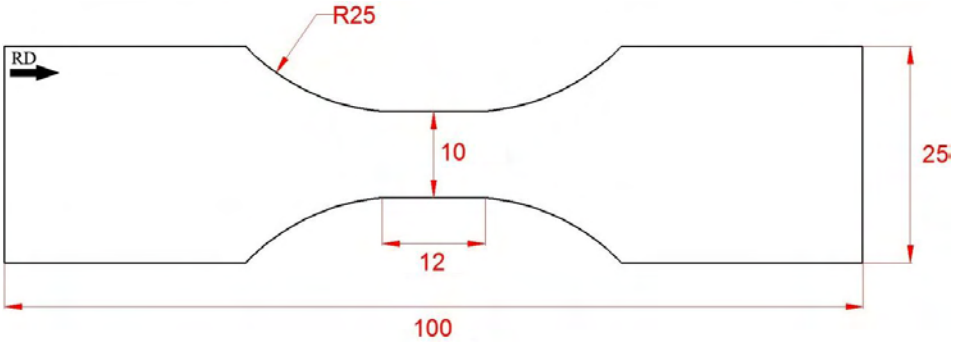

Figure 3.6 Geometry of LCF test specimen (dimensions in mm).

3.3.2.2 Stress controlled fatigue tests

Constant stress amplitude tests were carried out to determine the fatigue S-N curves on smooth and notched specimens at a stress ratio R= 0.1 and a frequency of 25 Hz. Smooth fatigue specimens were prepared according to ASTM E466 with a geometry shown in Fig. 3.7. To investigate the notched fatigue behaviour, specimens with a single, 60^o V-shape notch were used (Fig. 3.7(b)) with an elastic stress concentration factor of K_t = 3.5, calculated from the Noda et al. approach [98].

In order to examine the potential influence of austenite transformation effect taking place during machining of the notch, which is relevant for fatigue crack initiation, the 60^o V-shaped side notch was introduced in the specimens using two different machining methods. Except from the Regular Machining method (RM) using a milling angle cutter tool, the sinker Electrical Discharge Machining (EDM) method was also implemented. The EDM method, as a non-deforming cutting process, has the advantage of not plastically deforming the steel during removal of material. Although, as it will be explained in section 4.5.1, no significant transformation effect at the notch root caused by the machining process is expected, the above investigation was performed to ensure the reliability of experimental results.

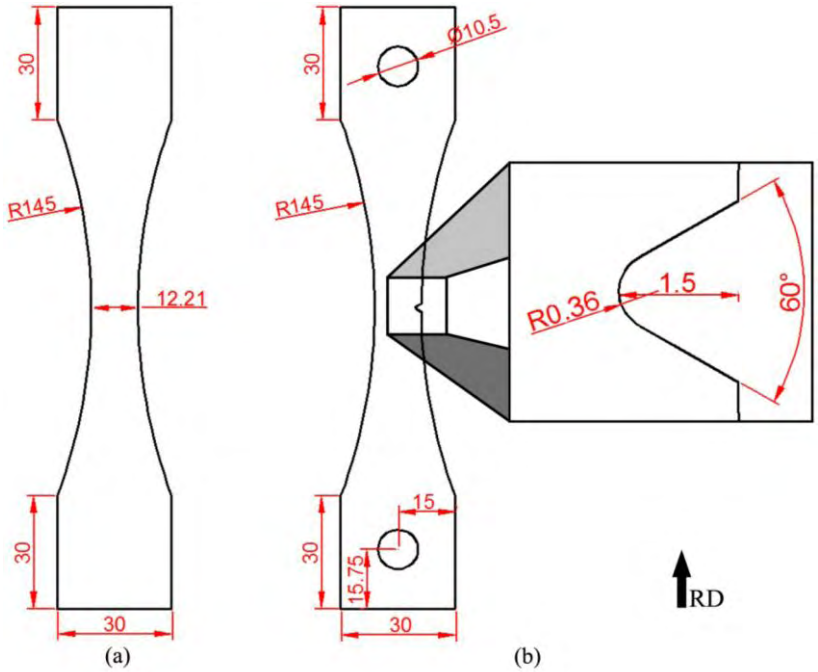

Figure 3.7 Geometry of (a) smooth and (b) notched fatigue test specimen (dimensions in mm).

3.3.3 Crack initiation Monitoring

Fatigue crack initiation and propagation at the notch root was monitored using the replica technique. Careful preparation of the notch area was conducted in order to remove imperfections (burrs) from the machining process by grinding with fine #1000-4000# grit papers, to ensure that no surface effects are induced on crack initiation. The notched fatigue tests were interrupted at regular cycle intervals and a small tensile load was applied to open the crack surfaces. Extreme care was taken into applying this tensile load, in order not to exceed the test's maximum cyclic load (P_{max}), which could possibly introduce an overload in loading history. Special replica foils of 0.1 mm thickness wetted with acetone, were used to take replicas from both sides of the notch root and were examined in an optical microscope. Cyclic stressing was continued for a small interval of cycles and the above procedure was repeated until a first short crack was observed in the replica through the microscopic observation. When the first short crack was observed the procedure was continued by making the interruption intervals more frequent. The length of the fatigue crack was measured using the replica images taken from microscope and processed with an image analysis software.

CHAPTER 4

Experimental Results

4.1 Microstructural characteristics

Basic microstructural features that were examined include RA distribution as well as RA and ferrite average grain size, parameters which are influencing the TRIP effect.

Characteristic microstructures of the investigated TRIP materials are presented in Fig. 4.1. Based on the etching solution used the tinting effect resulted in ferrite- straw brown, bainite- dark and retained austenite- white color. Two images for each material are indicatively shown in Fig. 4.1 with the phases presented in green (RA) and red color (ferrite). The masked micrographs were used as input in the image analysis software to evaluate the average grain size of the materials as well as the aspect ratio. The grain measurements of ferrite and retained austenite characteristics are presented in Table 4.1.

Table 4.1 Grain characteristics of TRIP steels.

Steel	Ferrite avg. size (μm)	Ferrite aspect ratio	RA avg. size (μm)	RA aspect ratio
	[Standard deviation]			
TRIP700(A)	3.62 [0.92]	0.63 [0.15]	1.03 [0.73]	0.33 [0.19]
TRIP700(B)	9.47 [2.48]	0.53 [0.14]	0.7 [0.34]	0.47 [0.18]
TRIP(HT2I)	4.77 [1.72]	0.55 [0.15]	1.25 [0.77]	0.31 [0.16]
TRIP(HT3I)	6.36 [2.4]	0.56 [0.13]	1.32 [0.75]	0.34 [0.18]
TRIP(HT2D)	4.21 [1.27]	0.60 [0.14]	1.03 [0.62]	0.29 [0.17]
TRIP(HT3D)	5.15 [1.75]	0.58 [0.13]	1.4 [0.77]	0.34 [0.17]

The TRIP steels examined can be characterized as fine grained materials with high RA dispersion in the ferritic matrix. The average size of RA particles was found 1.03μm and 0.7μm, while the average ferrite grain size was 3.62μm and 9.47μm, in TRIP700(A) and TRIP700(B) steel respectively. Regarding the TRIP(HTxx) materials, the average ferrite and RA size was found to be in the order of 5μm and 1.25μm, respectively. The smallest RA particle size belongs to TRIP700(B), which has also the largest ferrite grain size (9.47μm), while the largest RA particle size belongs to TRIP HT3D with 1.4μm. The ferrite grain size of TRIP HTxx steels does not present significant variations and is in the order of 4.2-6.3μm. TRIP700(A) has the smallest ferrite particle size with an average size of 3.6μm.

Examining the shape of ferrite grains in the as-received condition, not significant dissimilarities were observed between the TRIP materials, as the values of aspect ratio ranges from 0.53-0.63. The aspect ratio analysis of RA revealed that TRIP700(B) steel possesses a relatively higher diameter ratio (0.473), indicating that the RA's shape is more equiaxed compared to the other materials.

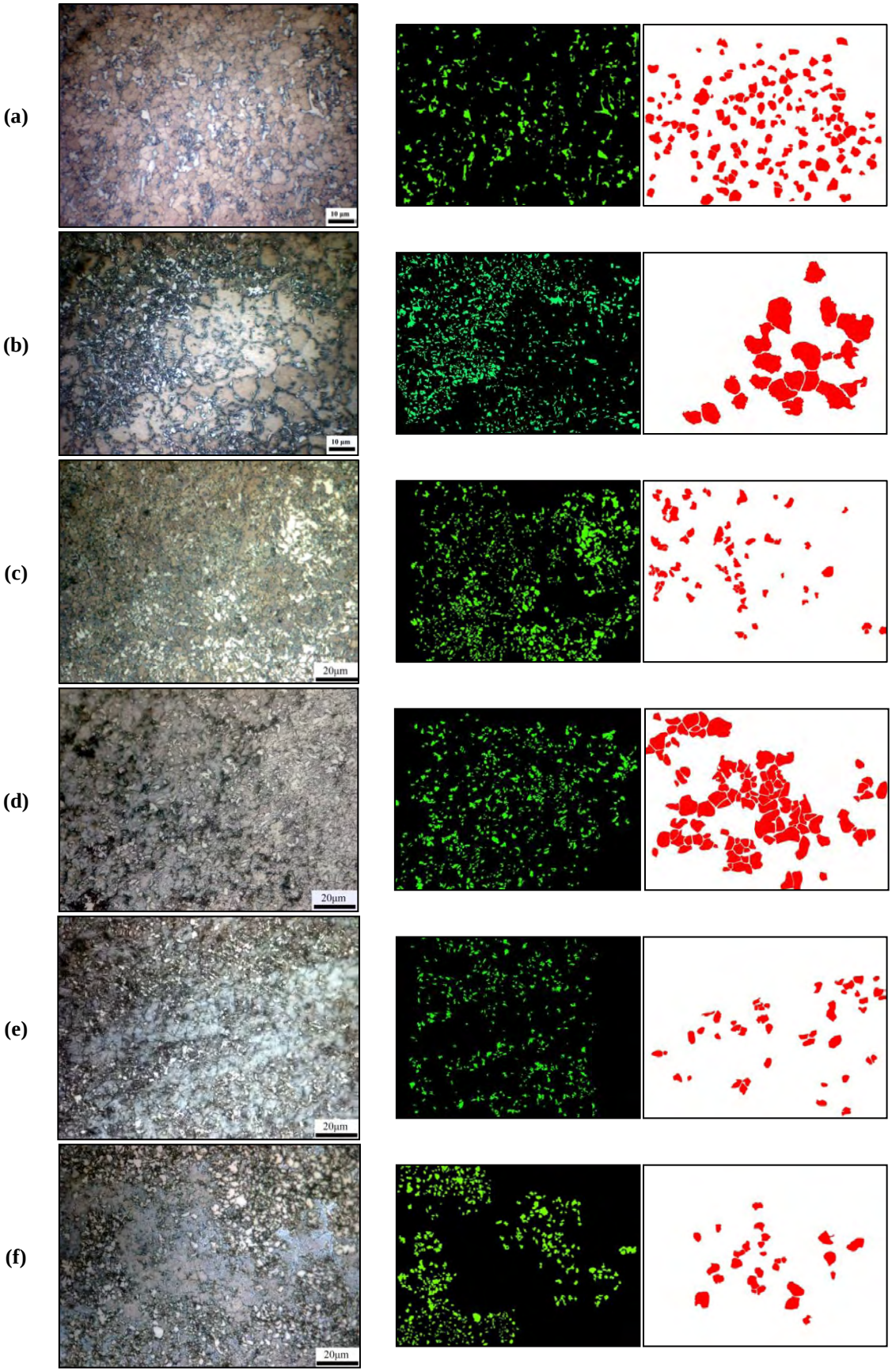

Figure 4.1 Microstructure and phase mapping of the investigated TRIP steels. (a) TRIP700(A), (b)TRIP700(B), (c) TRIP(HT2I), (d) TRIP(HT3I), (e) TRIP(HT2D), (f) TRIP(HT3D) steel (two images with ferrite and RA grains masked for each material is shown on the right).

A careful microscopic observation revealed that the RA grains in TRIP700(A) are located adjacent to ferrite grains, whereas in the other steels the RA grains are located adjacent and within ferrite grains.

A more detailed examination of the RA size variation was performed using image analysis software and is shown in Fig. 4.2. TRIP700(B) presented the most uniform particle size distribution, as indicated by the lower standard deviation value (0.34), whereas TRIP700(A) and the TRIP(HTxx) series presented less uniform RA grain size distributions.

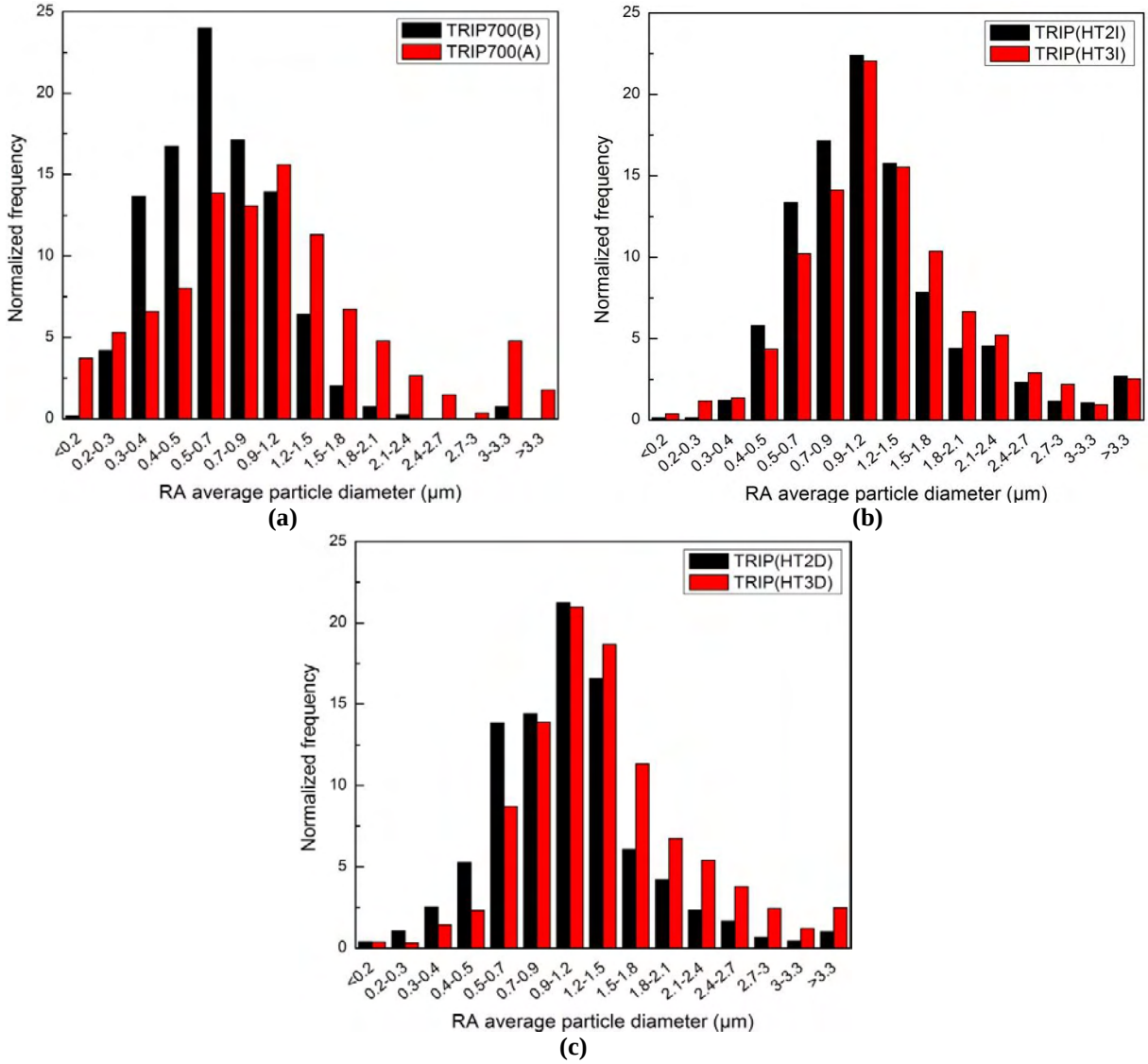

Figure 4.2 Histogram of RA grain size variance in, (a) TRIP700(A) and TRIP700(B), (b) TRIP(HT2I) and TRIP(HT3I), (c) TRIP(HT2D) and TRIP(HT3D) steels.

4.2 Tensile behaviour

The mechanical properties have been evaluated from the engineering tensile stress-strain curves (Fig. 4.3) and are given in Table 4.2. In general the TRIP materials combine high strength with ductility, and at the same time their behaviour is characterized by pronounced strain hardening. TRIP700(A), which is the only hot rolled steel in the group, exhibits the highest yield strength, lowest strain hardening potential and ductility compared to the other steels.

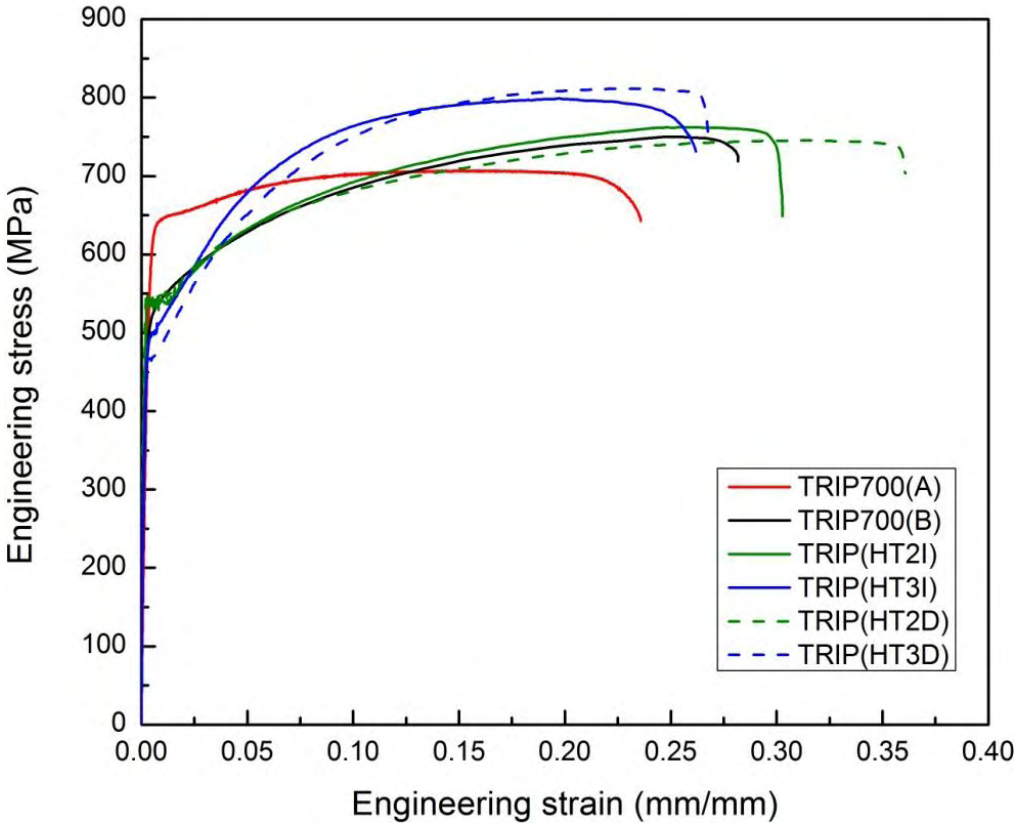

Figure 4.3 Engineering stress-strain curves of the investigated TRIP steels.

Table 4.2 Mechanical properties of TRIP steels.

Steel	$\sigma_{y0.2}$ (MPa)	σ_{UTS} (MPa)	$\sigma_{y0.2}/\sigma_{UTS}$	A_f (%)	A_g (%)	n	K (MPa)
TRIP700(A)	606	707	0.86	23.2	16.2	0.1132	1012
TRIP700(B)	515	749	0.69	28.2	24.9	0.196	1312
TRIP(HT2I)	537	762	0.7	30	26	0.2164	1289
TRIP(HT3I)	470	800	0.59	26	20	0.2357	1448
TRIP(HT2D)	540	744	0.73	36	31	0.203	1238
TRIP(HT3D)	462	817	0.57	26.7	23	0.2647	1529

4.2.1 Yield strength

It is well known that manufacturing conditions such as Hot/Cold Rolling as well as heat treatment processing of TRIP steels may influence the mechanical properties of the resulting material [99]. In hot rolled materials, which have generally little directionality in their mechanical properties due to recrystallization, the average grain size of the material can be reduced while maintaining a certain soft microstructure. Cold rolling on the other hand occurs with the material below its recrystallization temperature (usually at room temperature). Here, the increase in yield strength and hardness is obtained by introducing defects into the crystal structure of the steel, creating a hardened microstructure which prevents further slip [100]. The hot rolling process and small average grain diameter of ferrite and RA may therefore explain the high yield strength value obtained in TRIP700(A) [101]. The lowest yield strength belongs to HT3x steels, which have the largest ferrite particle size in the HTxx group.

The dependency of yield strength on the size of ferrite, which is the phase with the largest volume fraction, as described by the Hall–Petch effect [102] is confirmed by observation of the results in Fig. 4.4.

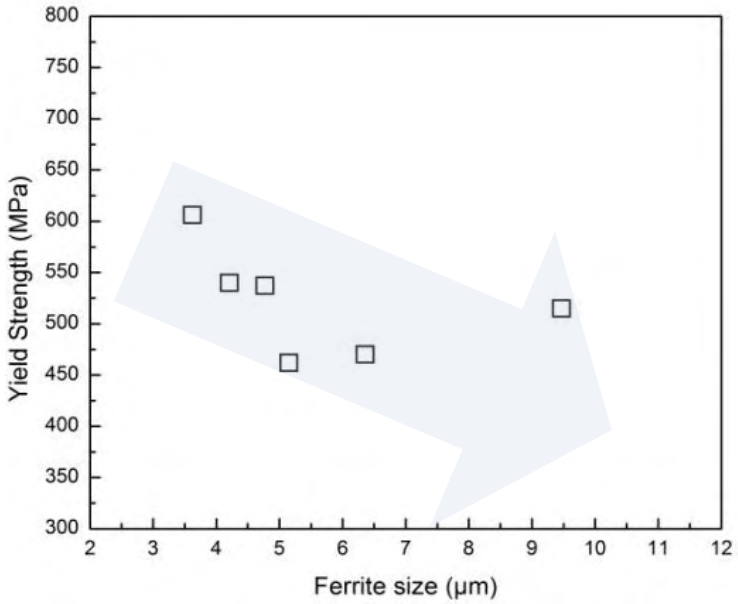

Figure 4.4 Effect of ferrite grain size on yield strength of the examined materials.

4.2.2 Strain hardening

Comparing materials with different rolling process, the finer ferrite grain size of steel (A) is expected to contribute also in the strain hardening behaviour, however the amount of strain hardening is higher in steel (B). This is a result of both the lower yield strength, which promotes higher initial work hardening, and the TRIP effect, which is controlled by the RA content and its stability [103]. The above contributes to a higher strain hardening exponent n=0.196 for steel (B) compared to n=0.102 for (A). The HT3x materials exhibit the highest strain hardening exponents of all steels, which as explained above is assisted by the lower yield strength of the specific steels.

4.2.3 Elongation

Comparing steels TRIP700(A) and (B) it can be observed that the uniform elongation is higher in steel (B) compared to (A) with values 24.9% and 16.2% respectively. That may be related to the slow and progressive work hardening capacity till necking (more stable behaviour regarding austenite transformation), the combination of high initial volume fraction of RA [23, 104] and the relatively fine and more equiaxed RA grains of TRIP (B).

A more clear understanding of the effect of transformation on mechanical properties may be obtained by examining materials with the same chemical composition and variations in microstructure as the HT2 and HT3 materials in the HTxx series. The different heat treatment processing results in changes in the size and initial content of RA particles as shown in Table 4.1. The HT2x materials present a more stable behaviour against transformation compared to HT3x, which is reflected in higher uniform elongation values and less strain hardening (Fig. 4.5) as described in the previous paragraph.

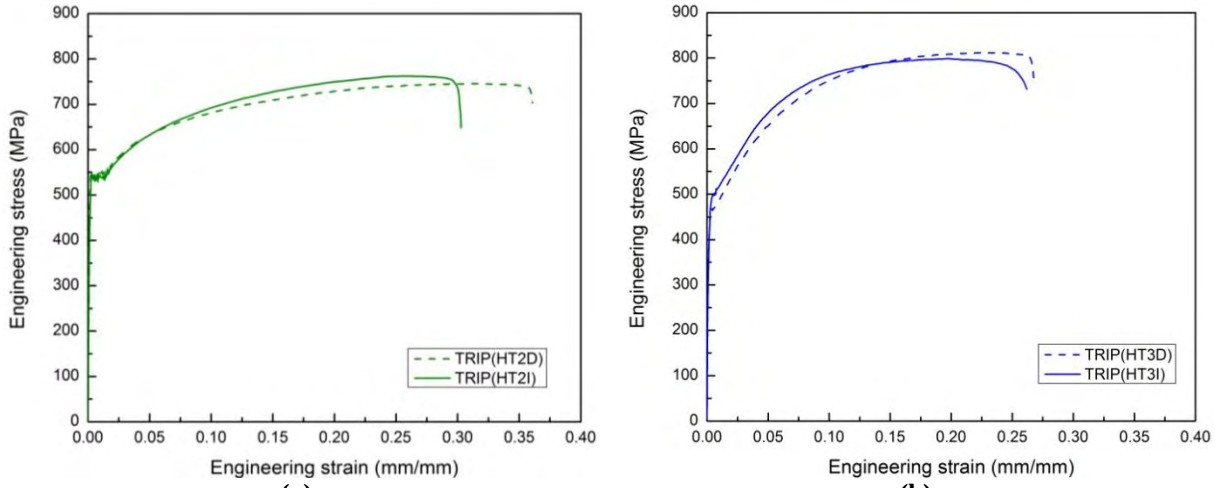

Figure 4.5 Engineering stress-strain curves of steels with same heat treatment process but small differences in chemical composition. (a) HT2 and (b) HT3 conditions.

The stress-strain behaviour in HT2x steels, is indicative of a more gradual austenite transformation occurring under increasing plastic deformation so that damage can be accommodated at all stages of deformation [62, 105]. The more "stable" transformation behaviour of HT2 compared to HT3 is confirmed also by the transformation measurements in Table 4.3, shown in section 4.2.4, from where it is observed that HT2 treatment leads to less amount of transformation compared to HT3. The smaller RA particle size induced by HT2 assists the observed behaviour, as direct experimental evidence presented in [106] showed that the stability of the RA is controlled not only by the local carbon level but also by the RA grain size.

4.2.4 RA transformation during tensile testing

Ex-situ magnetic measurements were conducted on fractured tensile specimens to determine the amount of RA transformation that took place during the tensile test. The measured RA volume fraction was correlated with the initial RA of the bulk material and the %RA transformed was evaluated.

In general the amount of transformation depends on the RA content and its stability. The stability of the phase against transformation is controlled by the carbon content [49], the RA

particle size and shape and the strength of the surrounding phases. In some cases the small RA particles have been associated with enhanced ductility against transformation [46, 105]. Stability may also be influenced by the shape of RA phase [49, 61, 62, 107] with "film like" or lamellar grains being more stable than blocky type or equiaxed RA grains. Furthermore a high content of alloying elements Al and Si makes the precipitation of carbides more difficult enriching the carbon content in austenite, contributing to a more stable RA phase [40].

The results shown in Table 4.3 reveal that the HT3x materials presented the highest amount of transformation (>79%), while (B) and HT2x steels exhibited moderate amounts of transformation (56-72%). TRIP700(A) steel presented the lowest amount of transformation with only ~50% of the initial vol.-%RA transformed during tensile testing.

Table 4.3 RA transformed at fractured tensile specimens.

Steel	%RA transformed (avg.)	
TRIP700(A)	44.9 57.6	(51.3)
TRIP700(B)	68.3 75.9	(72.1)
TRIP(HT2I)	54.9 58.3	(56.6)
TRIP(HT3I)	84.1 83	(83.6)
TRIP(HT2D)	63.7 75	(69.3)
TRIP(HT3D)	77.2 79.4	(78.3)

Regarding steels (A) and (B) the differences in chemical composition and microstructures due to the different rolling process, result in highly dissimilar tensile behaviour. Hot rolled TRIP700(A) exhibits a highly stable behaviour with the less amount of transformation amongst all steels examined (Table 4.3), the smallest strain hardening exponent and uniform elongation but at the same time the less ductile behaviour. On the other hand cold rolled steel TRIP700(B) shows high uniform elongation, moderate strain hardening potential combined

with a high amount of RA transformation due also to the higher initial %RA, which are indications of a more balanced transformation behavior under deformation.

The sensitivity to transformation during a tensile test cannot be explained based upon one single parameter. TRIP700(B) with the finer RA grains should exhibit relatively low amounts of transformation. Despite the finer RA grains of TRIP700(B) steel, the larger surrounding ferrite grains may impose a larger dilatational deformation provoking large mechanical driving force for transformation. In Fig. 4.6(a) an attempt is made to provide a correlation between the ferrite size and transformation potential of the materials by excluding other influencing factors such as the size of RA. The results are interesting and indicate that if the ferrite size would have significant influence on transformation behaviour, the latter would increase when the ferrite size becomes large. TRIP700(B) seems to take advantage of the small RA size and larger ferrite to provide a more balanced stress strain behaviour combining good strength and high uniform elongation.

Another aspect relating the amount of RA transformation to the mechanical response is the strain hardening behaviour. In Fig. 4.6(b) the %RA transformed at fracture is strongly correlated with the strain hardening exponent, which increases with the increase in RA transformation [108].

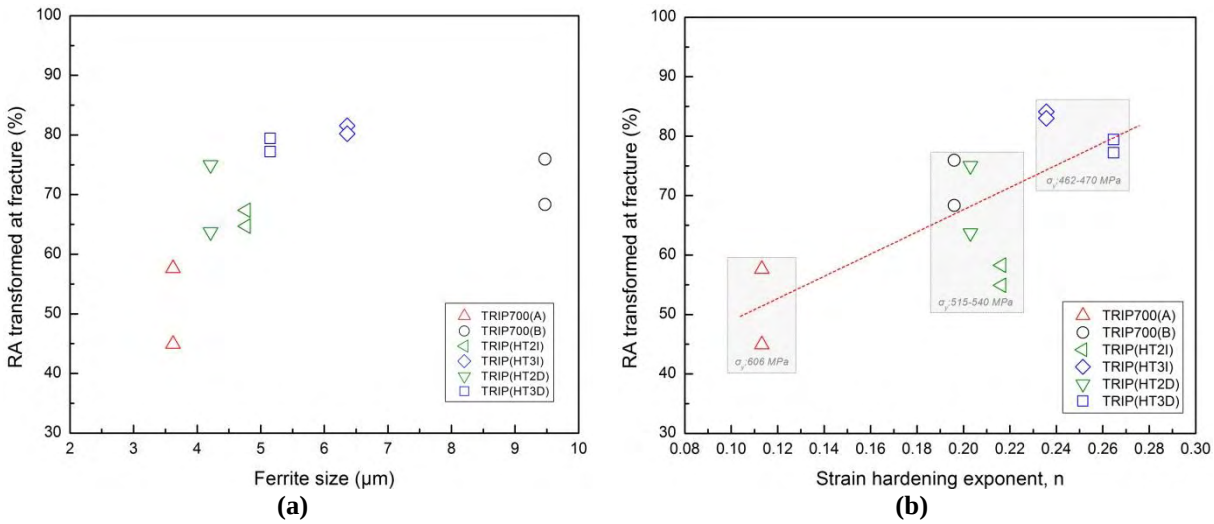

Figure 4.6 Correlation of %RA transformed at fracture during monotonic loading with (a) ferrite size and (b) strain hardening exponent.

Other aspects that contribute to the mechanical behaviour is the rate of strain-induced transformation [8] and the role of martensite. In [109] it has been shown that martensite can accommodate up to ~8% plastic strain during tensile plastic deformation. In general, when the material starts to deform plastically, the soft phases (ferrite and retained austenite) exceed their yield point while the hard martensite remains in the elastic state, thus the deformation continues with the soft phases transferring the stress to the hard martensite. The martensite starts to deform plastically when the transferred stress is large enough to reach its elastic limit. The latter leads to a high stress increment in the bulk material due to the high initial strain hardening of the martensite (Fig. 4.3). After the martensite flow curve levels off, its contribution to the strain-hardening rate of the material declines leading to lower rates.

4.3 Cyclic stress-strain behaviour

In this Chapter the low cycle fatigue performance and cyclic behaviour of the TRIP steels is assessed and the role of RA transformation on the mechanical behaviour is evaluated.

4.3.1 Strain-life data

The cyclic strain-life curves of the materials are presented in Fig. 4.7 and are compared in Fig. 4.8. The total strain amplitude is given as the sum of elastic and plastic parts, in the form:

$$\varepsilon_{a_{total}} = \varepsilon_{a_e} + \varepsilon_{a_p} = \frac{\sigma'_f}{E}\left(N_f\right)^b + \varepsilon'_f\left(N_f\right)^c \quad (4)$$

which is resolved as a sum of the Basquin's equation (ε_{ae}) and Manson-Coffin relationship (ε_{ap}).

The cyclic material parameters $\sigma'_f, b, \varepsilon'_f, c$ as evaluated from the strain-life data are given for each material in Fig. 4.7. At first sight, the materials present similar cyclic performance, however after more careful examination differences can be distinguished at fatigue regions where either the plastic or elastic component is dominant in the total strain amplitude.

Examining Fig. 4.8(b), TRIP700(A) and TRIP700(B) steels present an overall good cyclic behaviour with (A) prevailing in the plastic and (B) in the elastic range. The HTxx materials show in general an inferior performance compared to (A) and (B) steels, with HT3 variant showing an improved behaviour compared to HT2 except for very high plastic strain amplitudes.

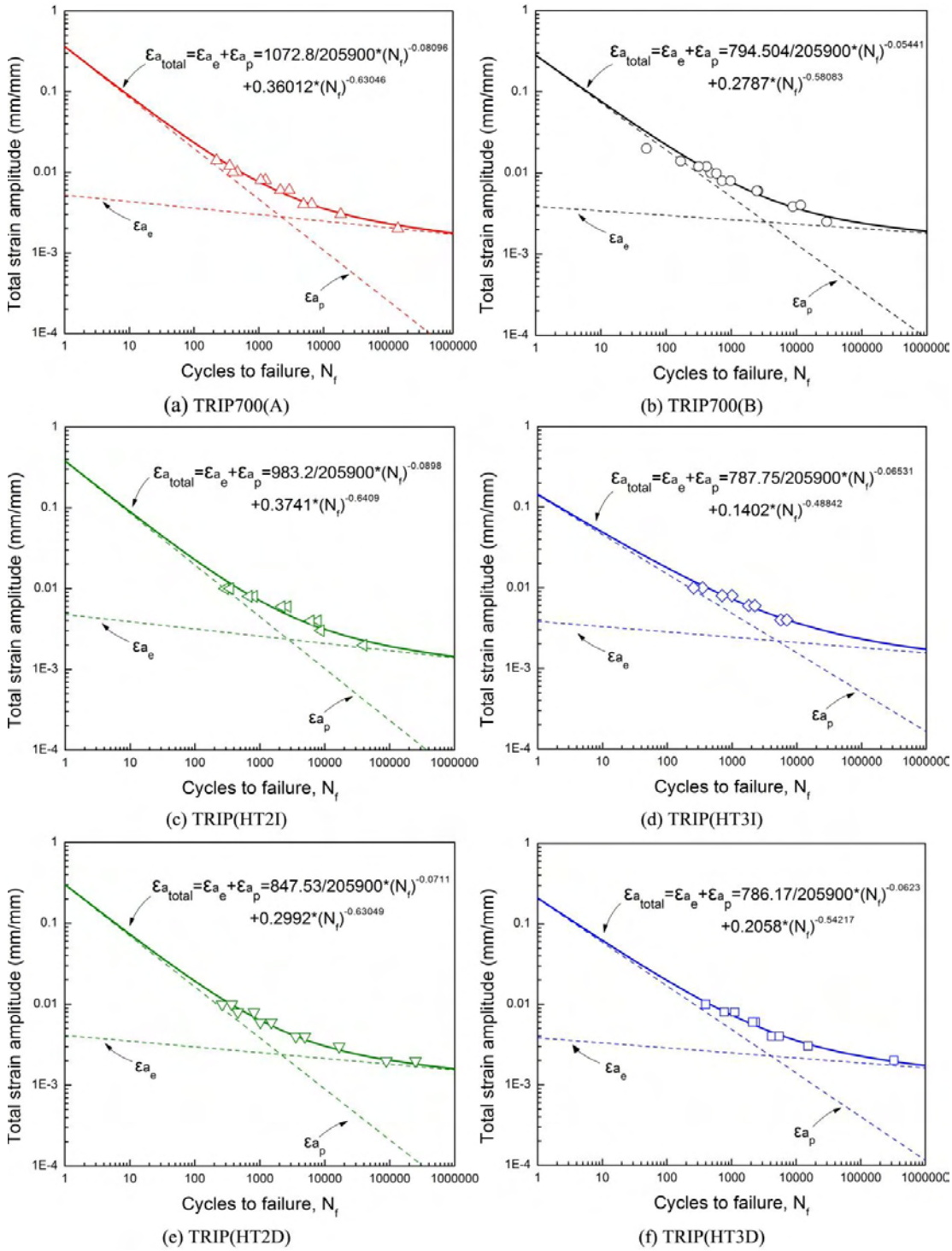

Figure 4.7 Strain-life curves showing total, elastic and plastic components for the investigated TRIP steels.

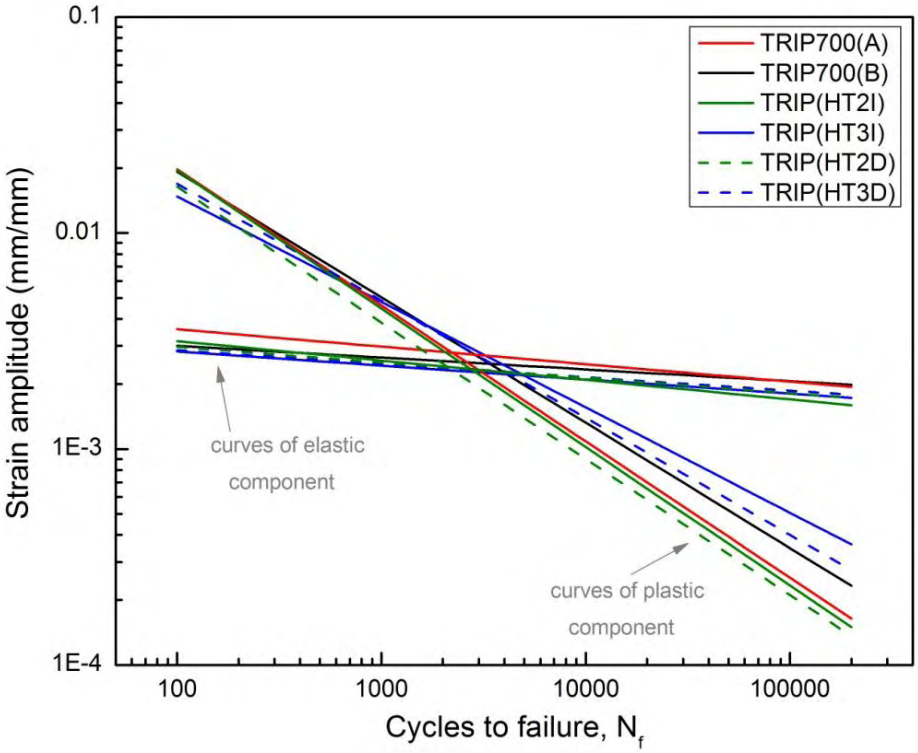

(a)

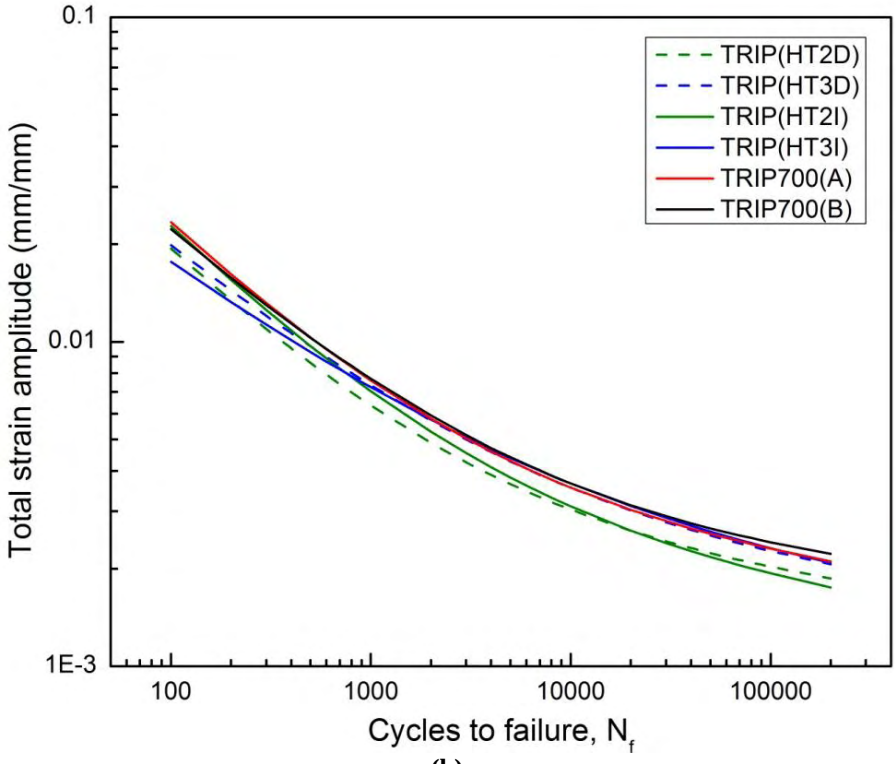

(b)

Figure 4.8 Strain-life curves of TRIP steels. Comparison of (a) elastic/plastic components and (c) total strain amplitude.

The transition fatigue lives (equal elastic and plastic strain components) are presented in Table 4.4. Transition life of HT3x steel is superior to HT2x with 4500 cycles and 2500 cycles

respectively. By comparing steels (A) and (B) from Table 4.4, steel (A) has a smaller LCF region characterized by a small transition life value, with regard to steel (B).

Table 4.4 Transition life of the investigated TRIP steels.

Steel	N^* (cycles)	ε_{atotal} (%)
TRIP700(A)	2320	0.2775
TRIP700(B)	3390	0.2497
TRIP(HT2I)	2750	0.236
TRIP(HT3I)	4900	0.218
TRIP(HT2D)	2140	0.2419
TRIP(HT3D)	4100	0.227

4.3.2 Cyclic stress-strain curves

The cyclic stress-strain curves were determined from the stabilized hysteresis loops and are presented in Figs. 4.9 - 4.11. The cyclic material parameters such as the cyclic strain hardening exponent, n' and cyclic strength coefficient, K' were assessed with the Ramberg–Osgood equation (Eq. 5) [110] and are given in Table 4.5.

$$\varepsilon_{a_{total}} = \frac{\sigma_\alpha}{E} + \left(\frac{\sigma_\alpha}{K'}\right)^{1/n'} \quad (5)$$

Table 4.5 Cyclic properties of TRIP steels.

Steel	Cyclic properties						
	$\sigma'_{y0.2}$	n'	K'	σ'_f	b	ε'_f	c
TRIP700(A)	554	0.1189	1160	1073	-0.08096	0.3601	-0.6305
TRIP700(B)	456	0.1971	1551	794	-0.0544	0.2787	-0.5803
TRIP(HT2I)	473	0.1368	1107	983	-0.08975	0.3741	-0.64092
TRIP(HT3I)	444	0.1425	1080	788	-0.06531	0.1402	-0.48842
TRIP(HT2D)	486	0.1125	980	848	-0.0711	0.2992	-0.63049
TRIP(HT3D)	461	0.133	1056	786	-0.0623	0.2058	-0.5422

Between the HTxx materials, (HT2D) steel exhibited the highest cyclic yield strength (486MPa) accompanied with the lowest cyclic strain hardening exponent (0.1125). The highest n' value of 0.1425 belongs to (HT3I) material, which however shows the lowest cyclic yield strength (444MPa). The behaviour is consistent with the monotonic behaviour of the steels.

In Fig. 4.12 the fitted cyclic stress-strain curves are displayed based on the cyclic stress strain parameters, n' and K' of Eq. (5) to obtain a clearer, comparative picture of the material behaviour. Material (B) has the highest strain hardening potential, while the lowest belongs to material (A). The HTxx materials cyclic strain hardening ability lies between TRIP (B) and (A) materials with HT3 variant showing higher cyclic strain hardening ability.

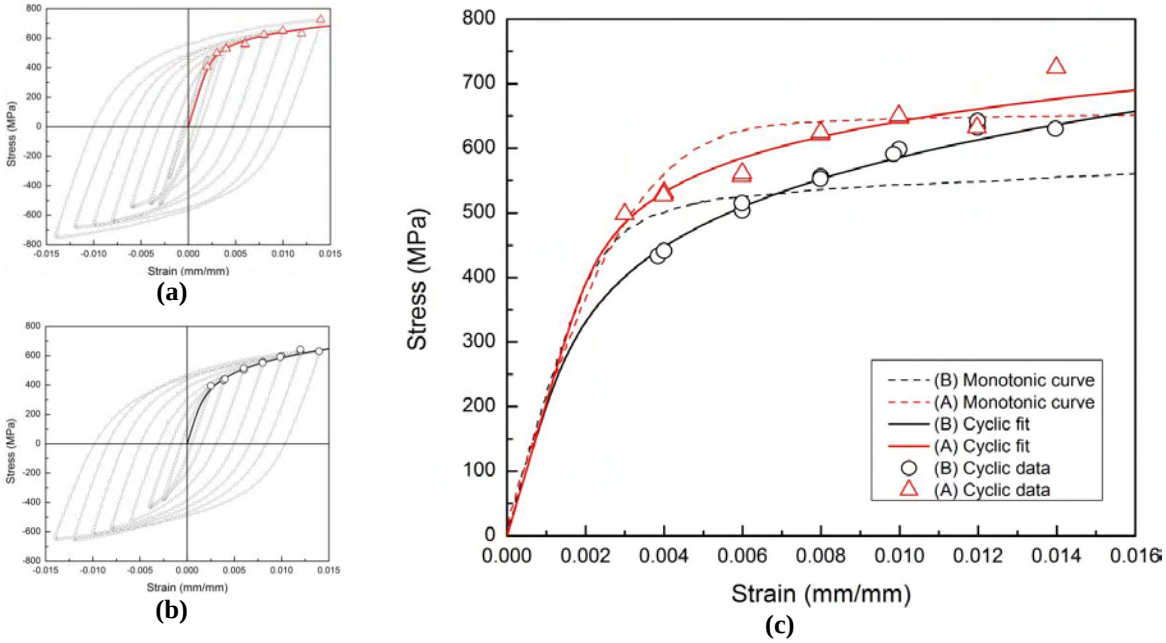

Figure 4.9 Stable hysteresis loops for determining the cyclic σ-ε curve of (a) TRIP700(A) and (b) TRIP700(B) steel. (c) Comparison of monotonic and cyclic σ-ε curves.

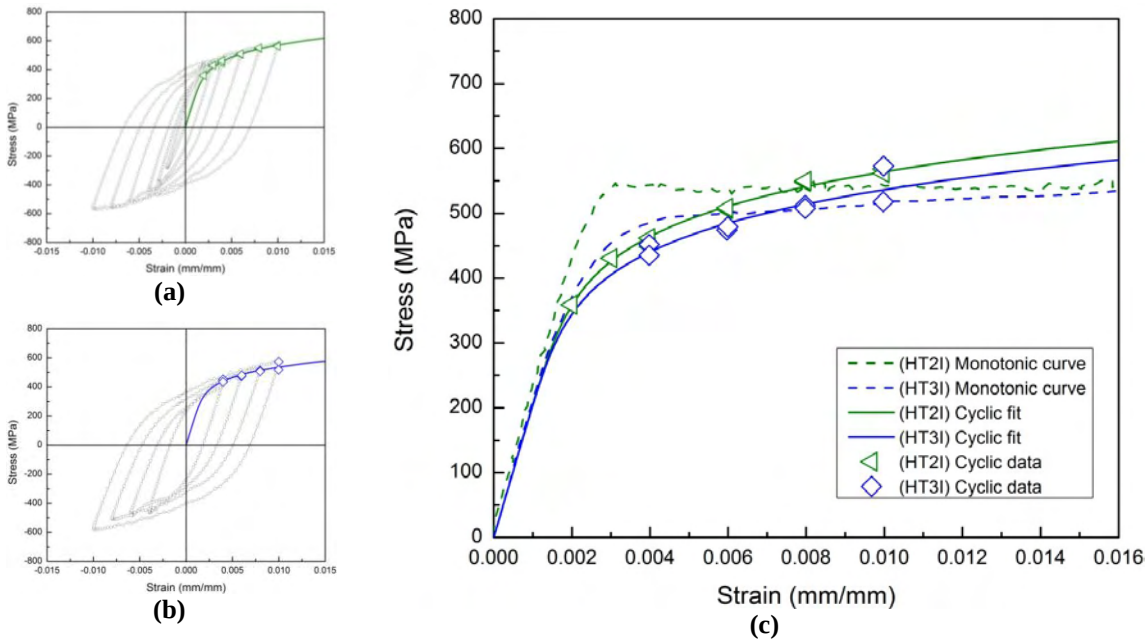

Figure 4.10 Stable hysteresis loops for determining the cyclic σ-ε curve of (a) TRIP(HT2I) and (b) TRIP(HT3I) steel. (c) Comparison of monotonic and cyclic σ-ε curves.

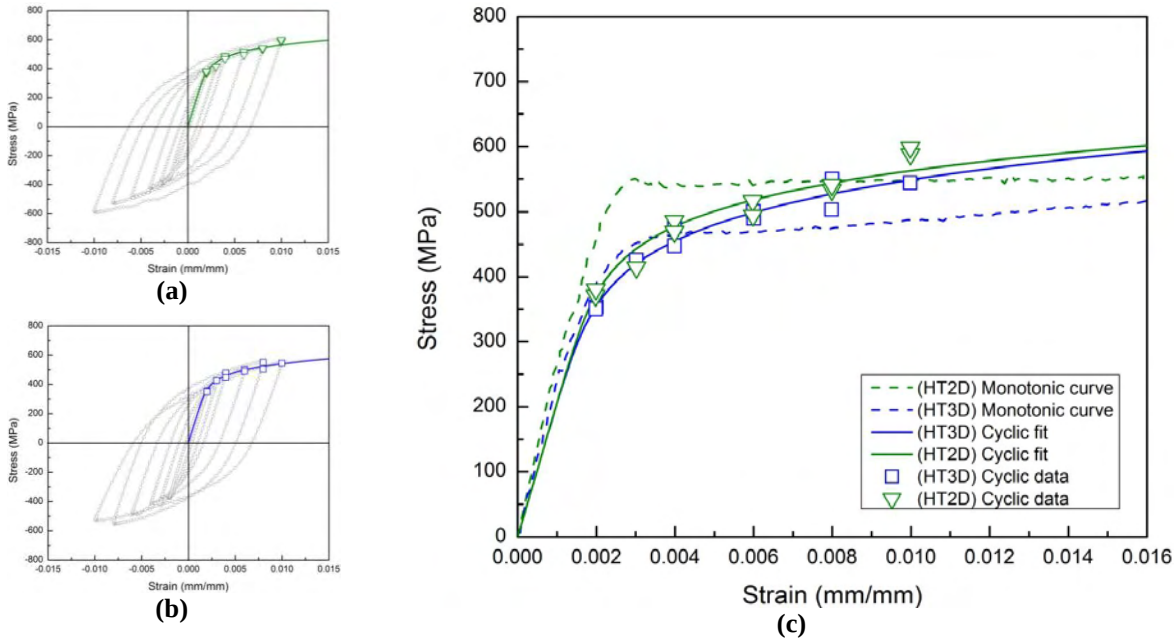

Figure 4.11 Stable hysteresis loops for determining the cyclic σ-ε curve of (a) TRIP(HT2D) and (b) TRIP(HT3D) steel. (c) Comparison of monotonic and cyclic σ-ε curves.

Lucas and Gerberich in [111] showed that larger ferrite grains can result in a higher cyclic strain hardening exponent. The observation is in good agreement with the results obtained in the present study, where a linear type relation between the ferrite size and cyclic strain hardening exponent is observed (Fig. 4.13).

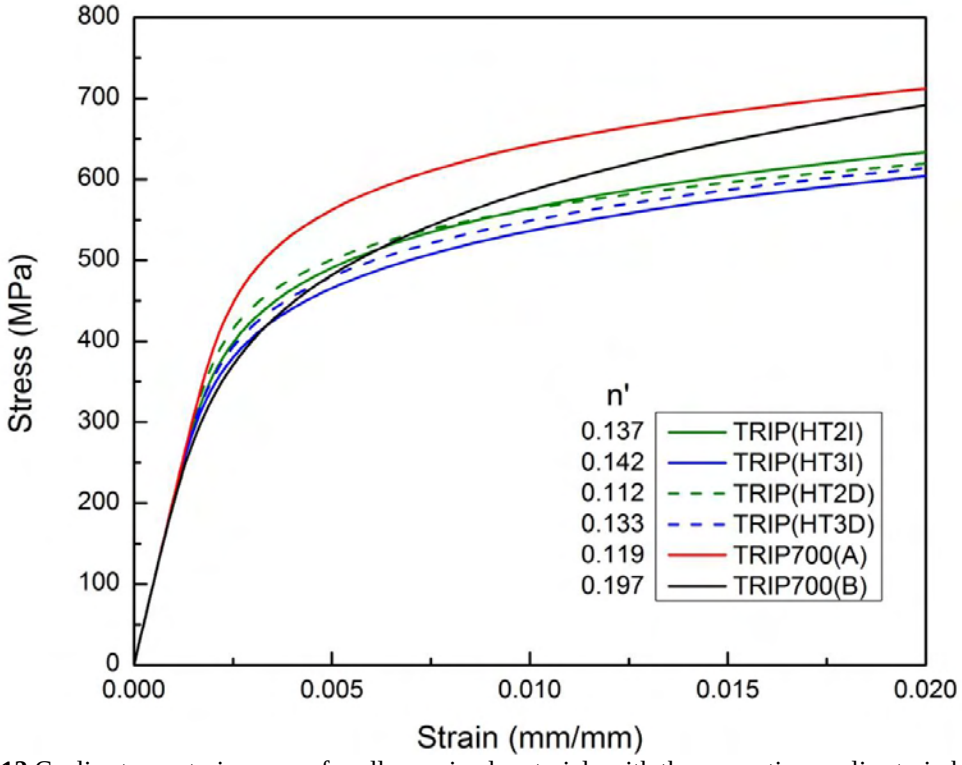

Figure 4.12 Cyclic stress-strain curves for all examined materials with the respective cyclic strain hardening values.

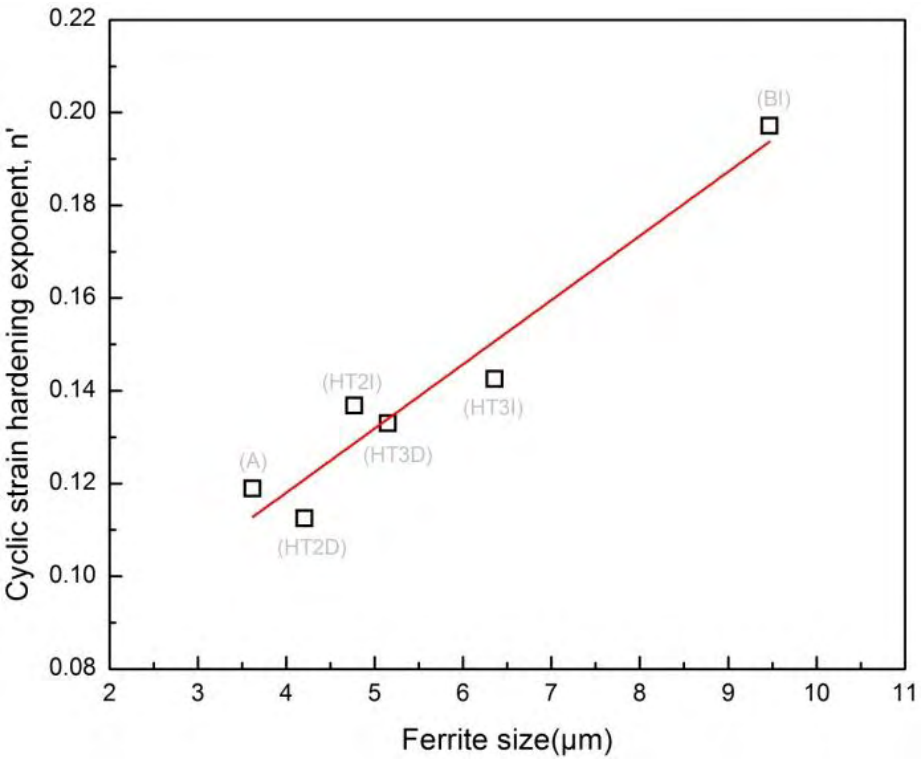

Figure 4.13 Dependence of ferrite size on cyclic strain hardening exponent, n'.

4.3.3 Cyclic hardening/softening

By comparing the cyclic stress-strain curves with the respective monotonic behaviour it can be noticed that most materials present a mixed type of cyclic behaviour including softening at small strain amplitudes, followed by cyclic hardening at higher amplitudes when the plastic strain component becomes more significant in the material behaviour. At strain amplitudes lower than 0.6%, all materials exhibit cyclic softening up to the final fracture, with HT2x and (A) steels showing extensive softening behaviour at larger strain amplitudes. The variation in tensile peak stress vs. the number of cycles during the strain controlled test, is presented in Figs. 4.14 - 4.16.

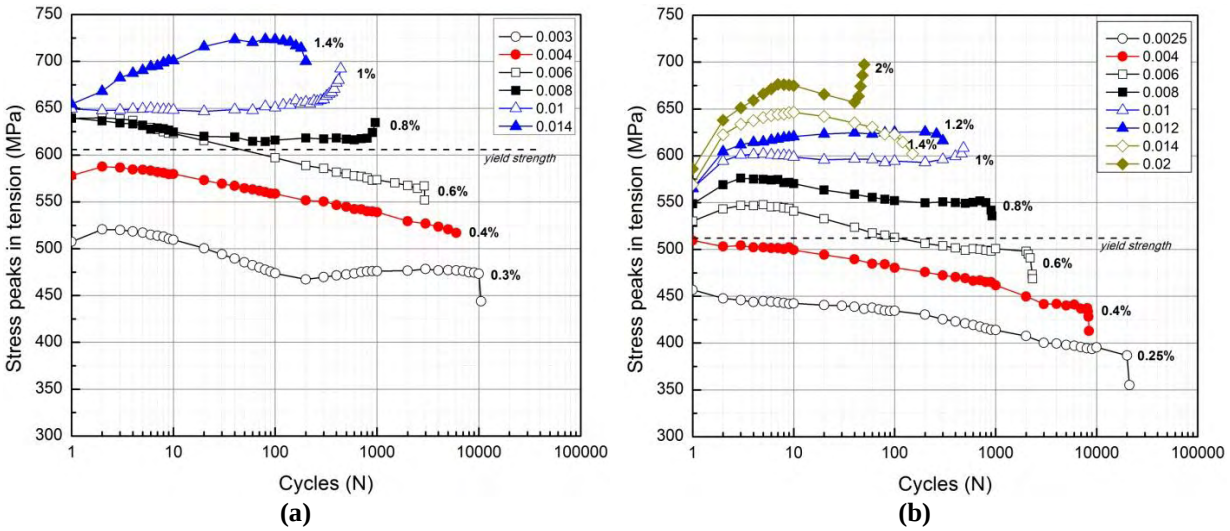

Figure 4.14 Cyclic stress peaks in tension of (a) TRIP700(A) and (b) TRIP700(B) steels.

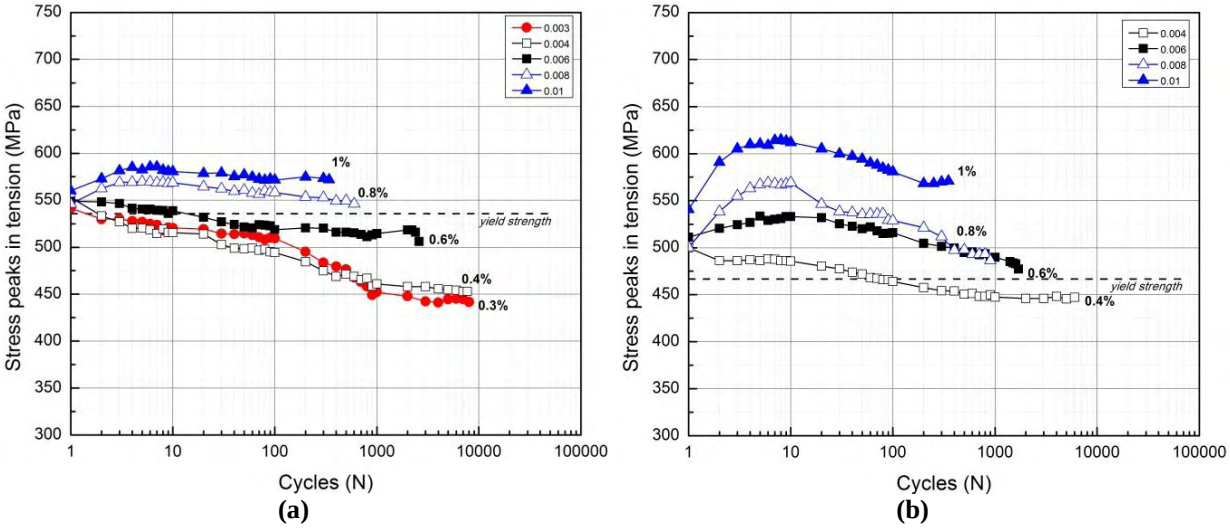

Figure 4.15 Cyclic stress peaks in tension of (a) TRIP(HT2I) and (b) TRIP(HT3I) steels.

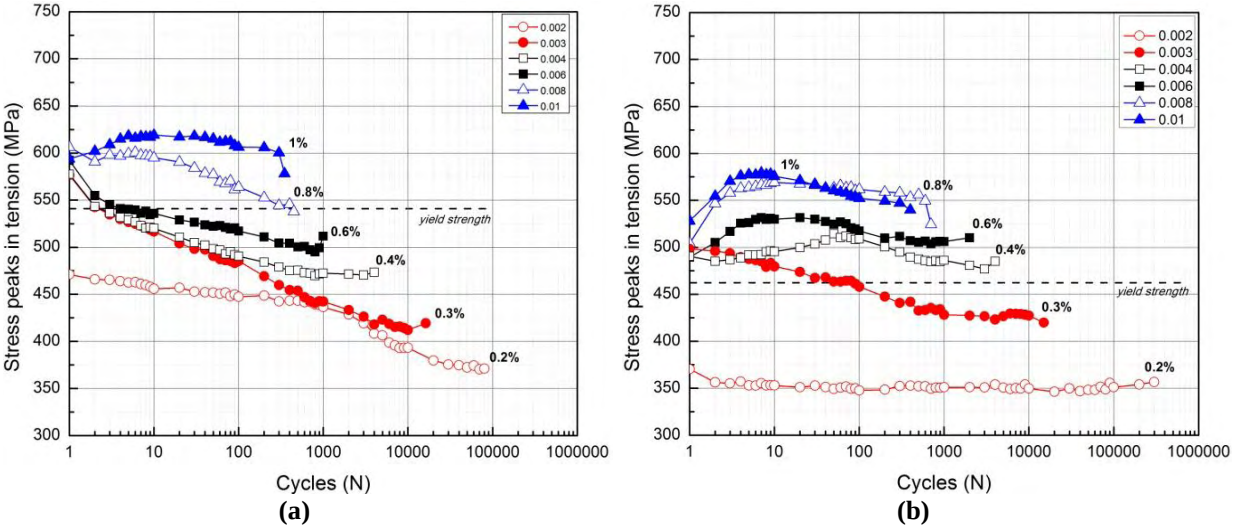

Figure 4.16 Cyclic stress peaks in tension of (a) TRIP(HT2D) and (b) TRIP(HT3D) steels.

In TRIP700(A) and (B) steels a gradual transition from cyclic softening to cyclic hardening with increasing strain amplitude is observed (Fig. 4.14). The gradual shift to cyclic hardening is observed when the plastic strain amplitude increases. In particular at strain levels above 1% a clear hardening effect is observed, which becomes more pronounced when strain amplitudes reach the value of 2%. The change from cyclic softening to cyclic hardening may be associated with the increase of RA transformation with increasing strain amplitude [5, 21, 75]. Under strain amplitudes with very small plastic component (0.25% - 4% total strain amplitude) cyclic softening occurs in both materials. When the plastic strain component becomes significant, steel (B) presents reduced softening compared to (A). For strain levels above 1% strain hardening controls the materials' behaviour with the amount of hardening being higher for steel (B). Contributing to this behaviour is the general trend of TRIP700(B) steel for higher RA transformation compared to (A) , as shown from the RA measurements of Fig. 4.17 presented in the following section. It is apparent from Figs. 4.15 - 4.16 that heat treatment processing influences the materials' cyclic response. TRIP(HT2I) and (HT2D) materials exhibit small amounts of initial cyclic hardening for strain amplitudes in the order of 0.8-1% whereas significant cyclic softening is observed for strain amplitudes below 0.6%. On the contrary, TRIP(HT3I) and (HT3D) materials exhibit higher amounts of initial cyclic hardening for strain amplitudes in the order of 0.6-1%, while the cyclic softening rate for strain amplitudes below 0.6% is decreased compared to HT2x materials.

All materials present a transitional behaviour from cyclic softening to cyclic hardening. The degree of hardening increases with increasing applied strain amplitude, which has been observed in a numerous studies in steels containing RA [14, 16, 20, 112]. The steels exhibit cyclic softening at strain amplitudes below 0.6% except HT3x materials where softening is evident at lower strain amplitudes. In some cases at low strain amplitudes where

cyclic softening prevails, a small initial hardening at an early stage was observed (<10 cycles) (e.g. steel B at strain amplitude 0.4%).

4.3.4 Cyclic behaviour and RA transformation

Steel (B) levels of transformation during cyclic straining prevail by a small amount compared to (A). Taking the heat treatment influence into account the (HT3I) steel's cyclic behaviour is accompanied by extensive transformation, exceeding by far the levels of the other materials (see Fig. 4.17), while in the (HT2I) steel's transformation amounts are small even below the levels of (A) and (B) steels. The transformation behaviour agrees with the respective behaviour under static loading presented in section 4.2.4.

Taking the above into account with regard to the LCF test results it may be observed that HT3 condition showing higher transformation than HT2, exhibits better LCF performance in the fatigue region where the elastic and plastic components are comparable, suggesting that there is a favorable link between RA transformation potential and LCF life.

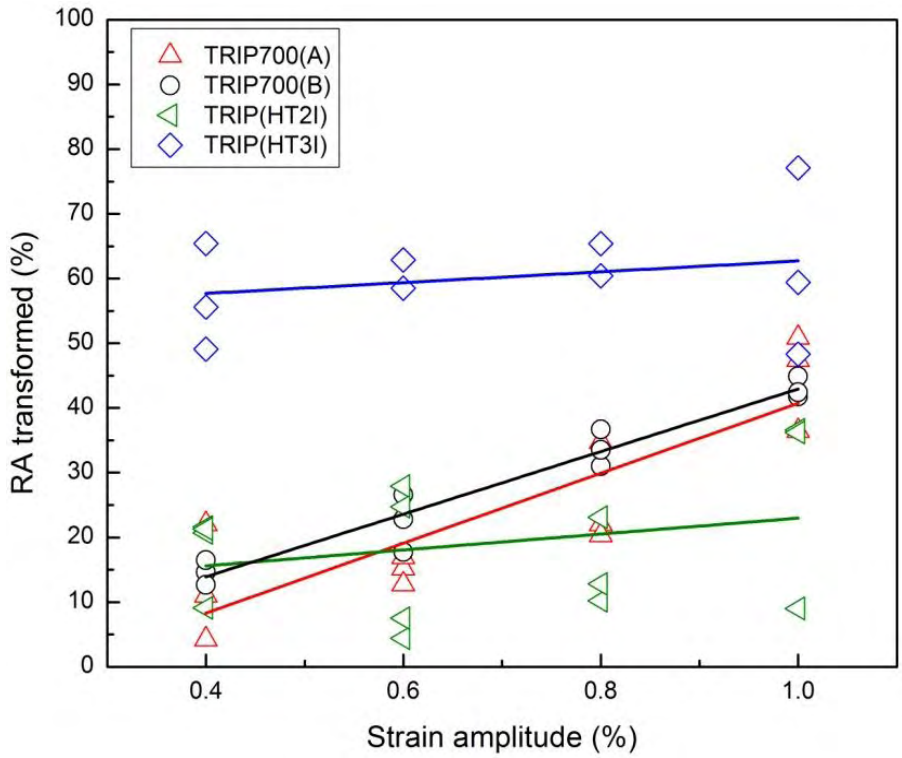

Figure 4.17 Percent RA transformed with regard to the applied strain amplitude.

Concerning the cyclic behaviour the results reveal that HT3 condition, which promotes higher transformation based on Fig. 4.17 is associated with higher cyclic strain hardening potential compared to HT2, while the low transformation levels of HT2 in Fig. 4.17 may be linked with the cyclic softening behaviour observed in Figs. 4.15(a) and 4.16(a). The above behaviour is also confirmed by the larger cyclic strain hardening exponent of the (HT3I) material compared to (HT2I) as shown in the results of Table 4.5.

4.4 High cycle fatigue behaviour

In order to investigate in more detail the elastic cyclic behaviour of the materials, the HCF performance of selected TRIP steels was conducted. In line with the previous investigation the effect of RA transformation on the HCF behaviour was assessed by measuring the RA value of the fractured fatigue specimens with the SM technique. The unnotched and notched S-N curves of (A) and (B) steels are shown in Fig. 4.18.

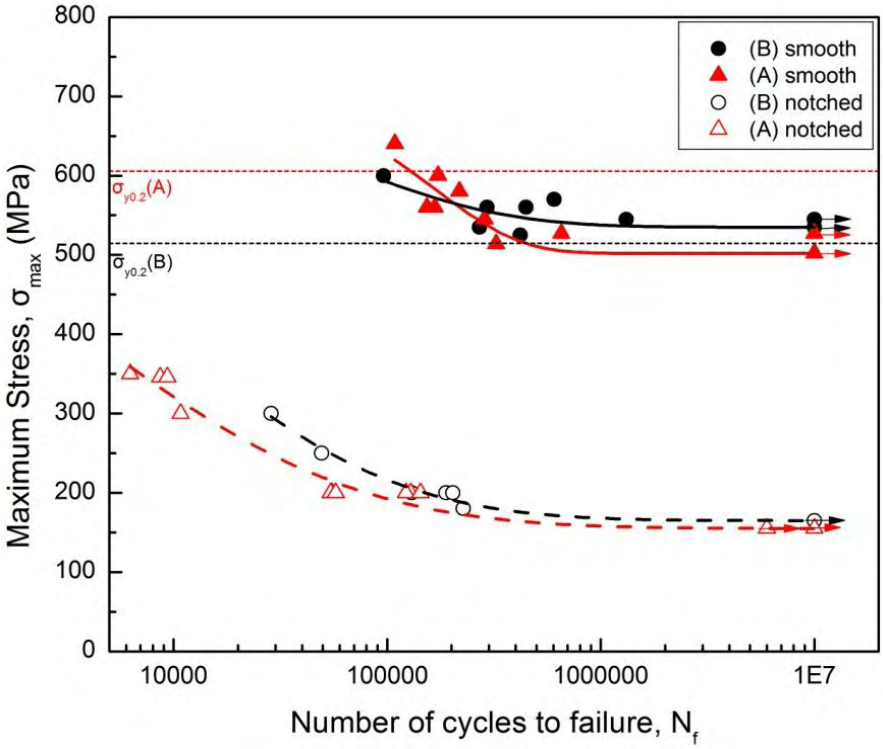

Figure 4.18 S-N curves of TRIP700(A) and (B) steels (arrows indicate run out tests).

The fixed fatigue limits (N=10^7 cycles), were approximated with the 4- parameter Weibull function of Eq. (6), with the fitting parameters C1, C2, C3 and C4 given in Table 4.6. For the calculation of the fitting parameter C_2 in both notched and unnotched specimens, the σ_{UTS} value of the materials was used. It is assumed that due to the ductile behaviour the presence of the notch does not significantly affect the σ_{UTS} value. For the fitting parameter C_1, the lower bound of the maximum stress at 10^7 cycles was used. Fitting parameters C_3 and C_4 are independent variables.

$$\sigma_{max} = C_1 - (C_1 - C_2) e^{-((\ln N)/C_3)^{C_4}} \quad (6)$$

Table 4.6 Weibull equation fitting parameters.

Steel		Fitting parameters			
		C_1	**C_2**	**C_3**	**C_4**
TRIP700(A)	smooth	502	707	12.0923	14.00281
	notched	155	707	8.7557	3.61503
TRIP700(B)	smooth	535	749	11.03327	6.53394
	notched	165	749	9.33309	4.22789

TRIP700(B) exhibits excellent unnotched fatigue performance with the fatigue limit (535MPa) lying close to the material's yield strength (515MPa). Steel (A) exhibits a slightly lower fatigue limit (502MPa) and a tendency for improved fatigue resistance at higher fatigue stresses, which is in agreement with the good LCF behaviour of steel (A) presented in section 4.3.1. The high tensile strength of TRIP700(B) assists the superior HCF performance compared to TRIP700(A) and the higher fatigue limit value.

The notched fatigue behaviour was evaluated with assessment of the fatigue notch factor, K_f and the notch sensitivity parameter q from the experimental curves of Fig. 4.18. The notch parameter values, which are presented in Table 4.7 indicate a detrimental notch effect on fatigue crack initiation in both steels, which translates in a drastic decrease in fatigue limit in both steels, which was found 165MPa for (B) and 155MPa for steel (A). The reduction in fatigue strength is 69% with regard to the unnotched specimens. At higher

stresses the curves tend to deviate with steel (B) showing better fatigue performance. It is an indication of steel (B) exhibiting better crack initiation resistance. The crack initiation behaviour of both steels is evaluated in section 4.5.

Table 4.7 Fatigue notch factors.

Steel	FL (MPa)	FLN (MPa)	K_t	K_f	$q=\frac{K_f-1}{K_t-1}$
TRIP700(A)	502	155	3.5	3.238	0.895
TRIP700(B)	535	165	3.5	3.24	0.896

4.4.1 RA transformation under HCF conditions

Transformation of retained austenite during high cycle fatigue was evaluated by measuring the RA volume fraction after the fatigue tests and the results are given in Fig. 4.19. Steel (A) transforms more in the elastic fatigue region compared to (B) for all stress levels examined and the transformation rate of steel (A) is higher compared to steel (B).

The trend in transformation potential is opposite to the behaviour observed under cyclic plastic strains examined in Fig. 4.17. This transition, may be explained by closer examination of RA microstructural features contributing to RA transformation. In [113-115] it has been shown that in a tensile test under small plastic strains the larger RA particles have the tendency to transform first, while the smaller particles transform at higher strains. In [113] the transformation behaviour of steel (B) revealed that the smaller the RA particle size the higher is the amount of plastic deformation required to enable transformation. The role of RA particle size on transformation has also been discussed in [70, 116]. In [116] it was found that retained austenite with a grain size smaller than 0.01μm will not transform to martensite, while RA particles with grain size larger than 1μm (which is the case for steel (A) in the present study), will immediately transform to martensite upon application of small stress. More specifically under elastic strains (HCF) the larger RA particles of steel (A) have more transformation potential compared to the smaller RA particles of steel (B). As plastic strains become larger (LCF) they provide the required driving force for the smaller particles of steel

(B) to transform. Hence, the % amount of transformation of steel (B) increases and combined with the higher initial RA content exceeds the transformation levels of steel (A). The RA measurements from the monotonic tests shown in Table 4.3 confirm this trend showing that at fracture, after the materials have undergone severe plastic deformation, steel (B) exhibits higher RA transformation. The transformation dependency on particle size under cyclic plastic staining has been reported in [87]. Under cyclic stresses, as expected, the amount of RA transformation increases with increasing maximum stress as shown in Fig. 4.19.

The effect of RA transformation on the fatigue limit is examined next for the different steels. Fatigue strength has been found to benefit from deformation induced transformation in [24, 25, 87]. The S-N fatigue results from [24] on TRIP(HT2I) and (HT3I) steels are used here for completeness of the investigation. Combining the results from [24] and experimental tests from the current Thesis on (A) and (B) steels the S-N curves of materials are presented in Fig. 4.20, while in Fig. 4.21 the %RA transformation in the HCF regime is plotted against the maximum cyclic stress.

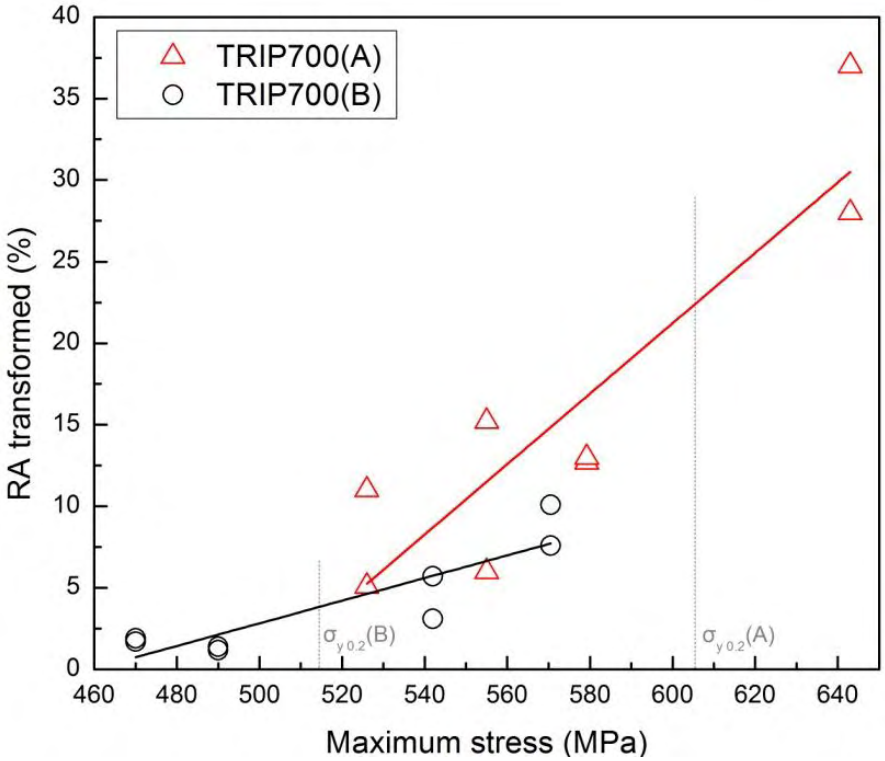

Figure 4.19 RA transformed with regard to the applied maximum stress.

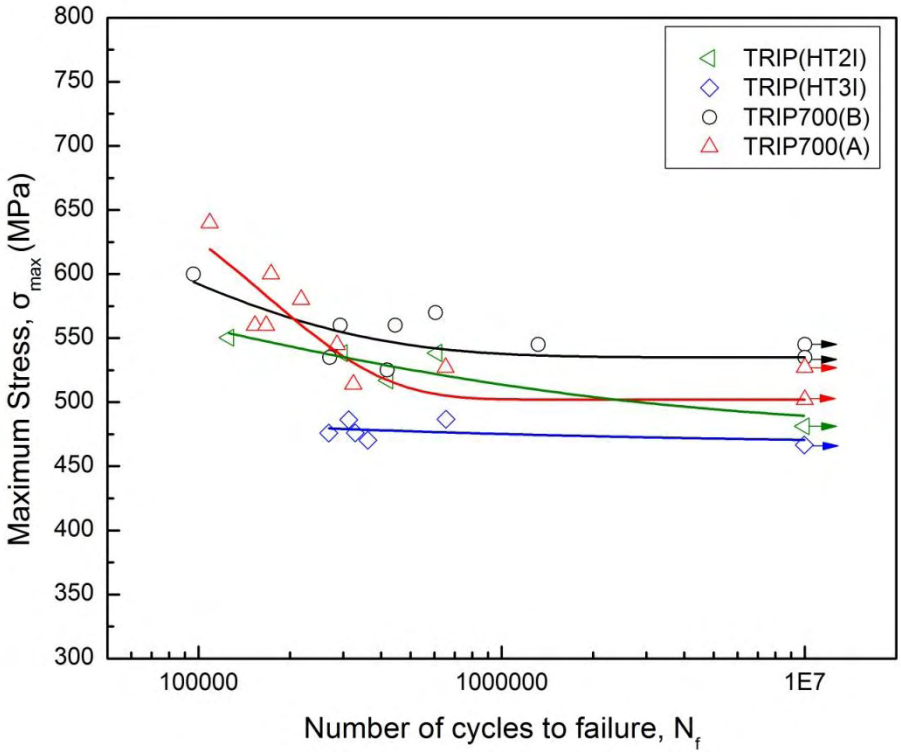

Figure 4.20 HCF behaviour of TRIP steels.

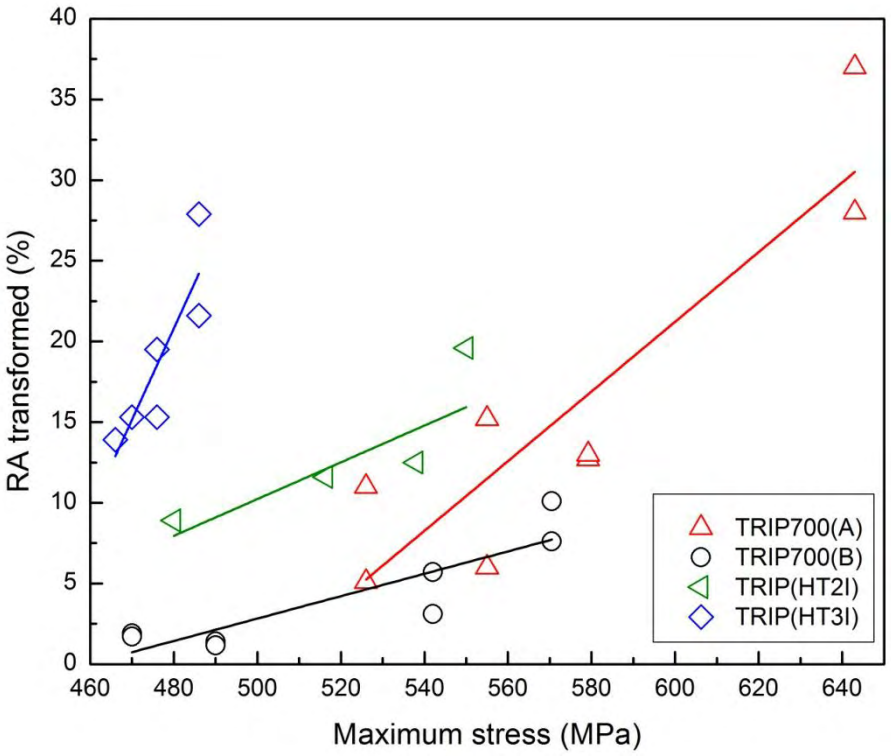

Figure 4.21 RA transformed with regard to the applied maximum stress.

Steel (B) with the highest fatigue limit exhibits the lowest amounts of transformation as shown in Fig. 4.21. On the other end steel (HT3I) with the lowest fatigue limit shows the highest transformation levels. By examining Figs. 4.20 and 4.21, a clear tendency of

increasing fatigue limit with decreasing transformation levels is obtained. In [24], the higher fatigue limit of (HT2I) steel was associated with higher austenite stability. Evaluation of the above findings suggests that in contrary to the LCF behaviour, under HCF conditions high transformation potential of metastable austenite to martensite degrades the fatigue performance of materials.

4.5 Fatigue crack initiation

In this chapter the fatigue results of the crack initiation behaviour of TRIP steels are presented. In the investigation fatigue crack initiation is considered as the fatigue stage where the length of the growing crack at the notch root reaches 250μm. With the length of 250μm the crack is significantly larger than the grain size of materials and the assumption that it propagates in a homogenous and isotropic field where application of fundamental fatigue and fracture theory is feasible (Fig. 4.22).

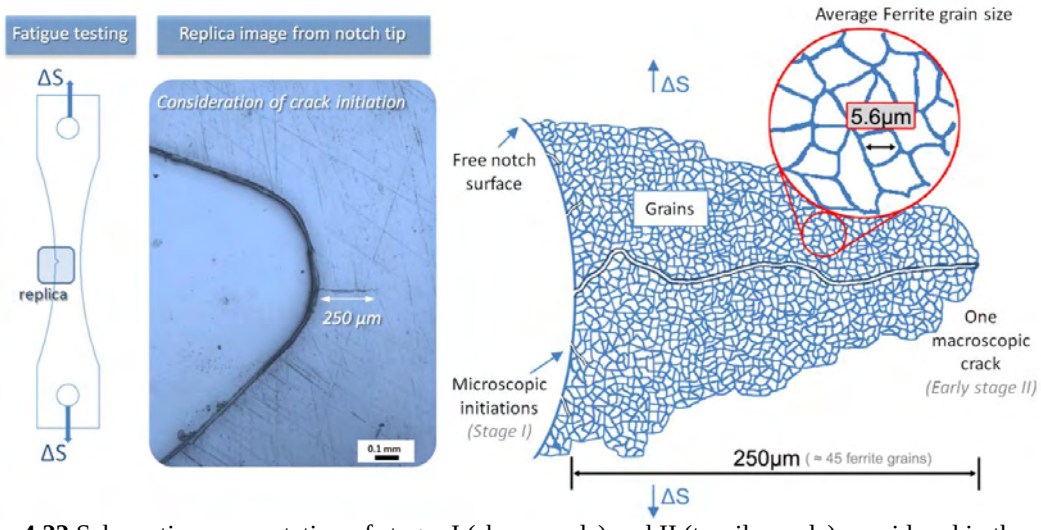

Figure 4.22 Schematic representation of stages I (shear mode) and II (tensile mode) considered in the present study for the assumption of crack initiation.

In the findings of Jacques et al. [63], in-situ measurements of stress and strain partitioning in TRIP steels during monotonic loading revealed that a representative microstructural "element" typically involves ~100 grains and at that level of magnification the average mechanical properties of the constituent phases are relevant.

In Fig. 4.23, characteristic images of the initiating crack and its progressive advance from the notch tip are displayed for (A) and (B) steels, while in Fig. 4.24 the fatigue crack growth curves for materials (A), (B) and HTxI are displayed. The case examined in the figure, refers to fatigue experiments with maximum stress σ_{max}=200MPa and R=0.1.

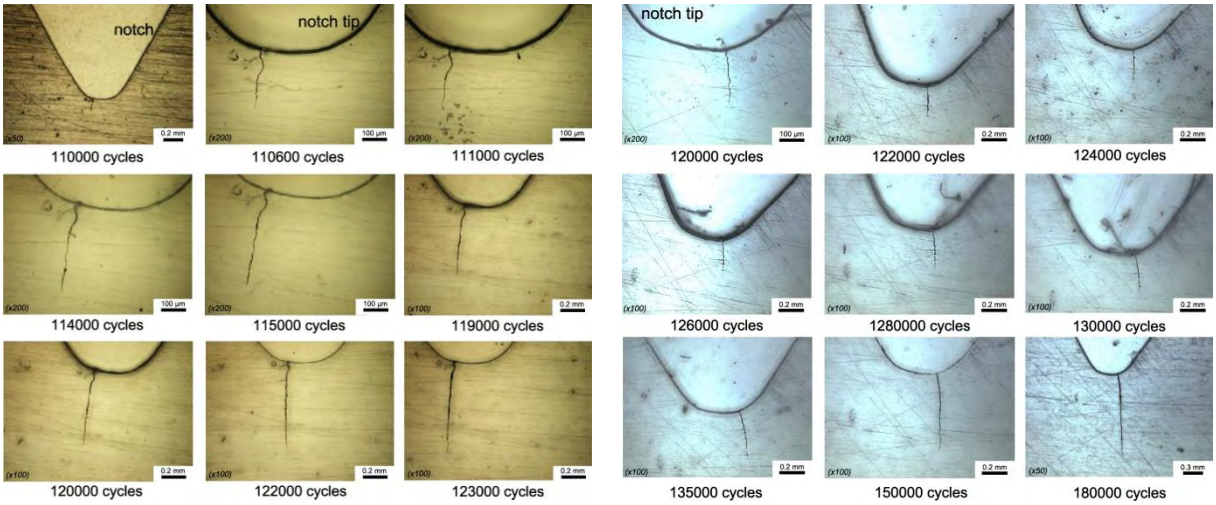

(a) **(b)**

Figure 4.23 Replica images showing crack evolution from notch tip in (a) TRIP700(A) and (b) TRIP700(B) steel using RM method (loading axis is in the horizontal direction).

The number of cycles corresponding to crack initiation life (N_{ini}) are presented in Table 4.8 as the average number of cycles at which the first 250μm crack at the free surface is detected.

Table 4.8 Fatigue crack initiation with EDM method (σ_{max}= 200MPa).

Steel	N_f (cycles)		N_{ini} (cycles)	
TRIP700(A)	87300 140420	113860	53080 79000	66040
TRIP700(B)	168860 181450	175150	106060 111870	108970
TRIP(HT2I)	164790 158910 122090	148600	87190 66470 55240	69630
TRIP(HT3I)	184840 181990 192850	186560	82300 95100 96000	91130

From the results of Table 4.8 it can be noticed that steel (HT3I) is the most damage tolerant material with 186560 cycles, followed by steel (B) with 175150 cycles before failure.

The average fatigue life for the other materials was 113860 cycles for steel (A) and, 148600 cycles for steel (HT2I).

Regarding the fatigue crack initiation stage, steel (B) exhibits the highest crack initiation resistance, which corresponds to an average number of 108970 cycles. The worst crack initiation behaviour with 66040 cycles belongs to steel (A), while (HT3I) and (HT2I) showed crack initiation lives of 91130 and 69630 cycles respectively.

Crack initiation resistance is primarily associated with microstructural aspects controlling the start of cyclic slip or twinning mechanisms under cyclic strains, which is macroscopically associated with the materials fatigue limit [117]. In notched fatigue problems, it may also be relevant to the materials LCF behaviour since at the root of the notch an elementary material volume may be assumed to undergo LCF type conditions [18, 118, 119]. Additionally, the transformation mechanism due to the localized plastic strains at the root of the notch is also expected to have an impact on crack initiation [22, 86, 91]. For the above reasons providing an explanation for the differences in crack initiation behaviour of TRIP steels can be superficial. In the following paragraph it is attempted to isolate specific characteristics, which may contribute to the observed behaviour.

Comparing the results between the HTxI variants, steel (HT3I) shows better crack initiation resistance compared to (HT2I). Although (HT3I) exhibits a lower smooth fatigue limit compared to (HT2I), it has superior LCF performance under cyclic strains with the plastic component being comparable to the elastic component. Furthermore, the HT2 variant exhibits more pronounced cyclic softening compared to HT3. Steel (A) also exhibits extended cyclic softening behaviour and a transition to cyclic hardening only at large strain amplitudes. (Figs. 4.14 - 4.16). Steel (B), has the highest fatigue limit, exhibits a very good LCF behaviour and a microstructure with moderate stability against RA transformation, where transformation develops gradually with increasing plastic strains.

In general it may be observed that materials showing cyclic softening accompanied with low amounts of transformation under LCF conditions, present a less damage tolerant behavior and resistance to fatigue crack initiation is assisted by a microstructure with a moderate RA transformation behaviour under cyclic strains, which promotes the gradual cyclic hardening mechanism, while cyclic softening associated with less transformation potential is not advantageous for damage tolerance.

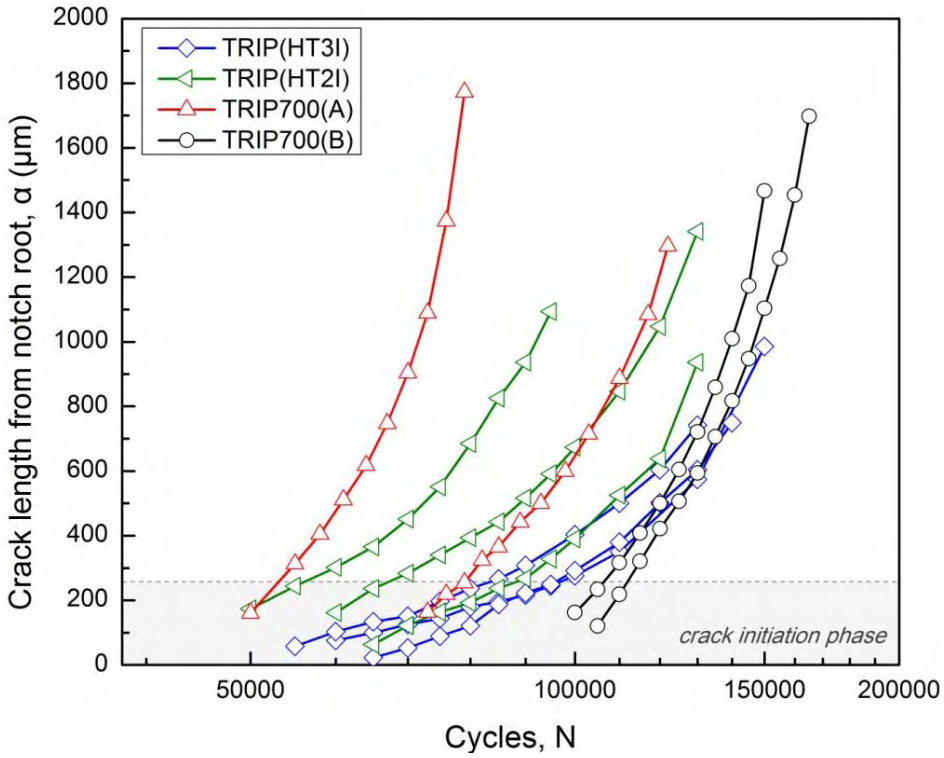

Figure 4.24 Fatigue crack growth curves of the examined TRIP steels with EDM method (σ_{max} = 200MPa).

4.5.1 Effect of notch machining on fatigue crack initiation

Crack initiation behaviour can be influenced by the cutting process during notch preparation due to the localized plastic deformation induced at the notch surfaces by the machining process. In order to evaluate the possible influence on crack initiation of localized RA transformation during machining, the plastic deformation field ahead of the notch tip induced by the machining process has to be assessed. The magnitude of deformation depends on various parameters such as material, processing and conditions of machining (lubrication, wear state of machining tool etc.). From the limited information available the large amount of

subsurface plasticity occurs in the material at an average scale length of 10μm [120-122] from the machining surface. At larger depths, plastic strains are reduced rapidly within a length scale of 50-100μm. This length scale is significantly smaller compared to a) the length scale examined from the notch root for crack initiation, b) the magnitude of plastic strains at the notch root induced by the external loading of 200MPa. This is expected to reduce the influence of the machining deformation effect since it is embedded inside a locally, more extended plasticity caused by the external loading during the first cycle.

In order to validate the effect of notch machining on crack initiation, an additional experimental investigation was carried out. Specifically, the fatigue crack initiation tests were repeated for steels (A) and (B) on new specimens having the notch introduced with the EDM (Electro Discharge Machining) method. In Fig. 4.25 the fatigue crack growth curves are compared with the RM and EDM methods and the evaluation of results is presented in Table 4.9.

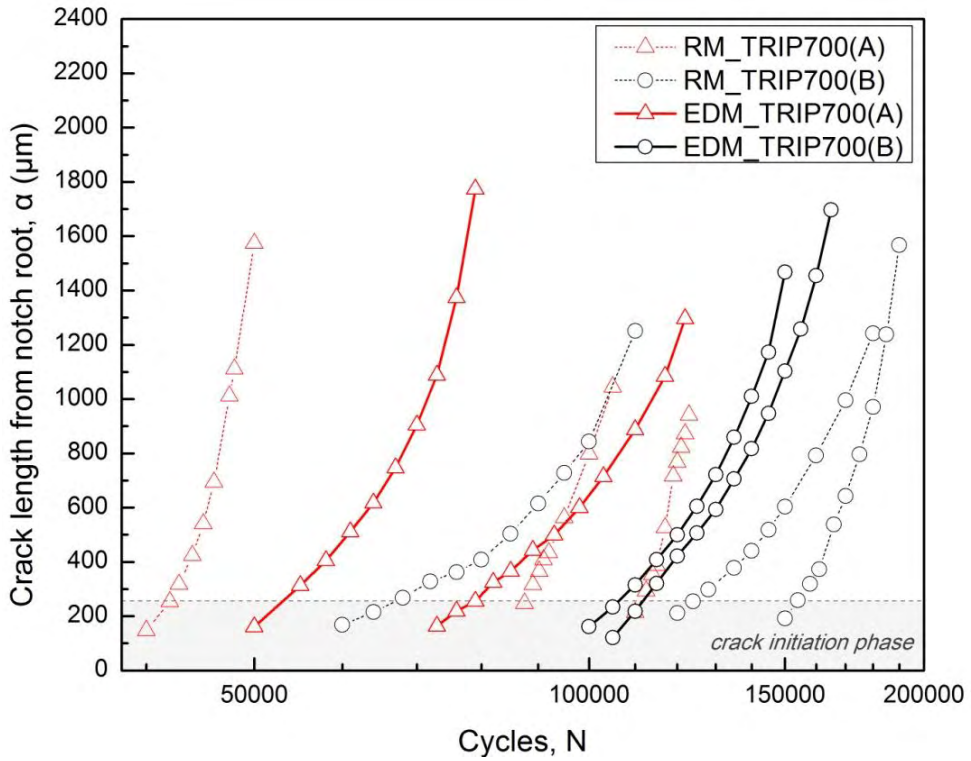

Figure 4.25 Fatigue crack growth curves of TRIP700(A) and (B) steel. Effect of notch machining on crack initiation (RM: Regular machining, EDM: Electro discharge machining).

Table 4.9 Fatigue crack initiation with RM method (σ_{max}= 200MPa).

Steel	N_f (cycles)		N_{ini} (cycles)	
TRIP700(A)	122420	107770	87700	80300
	143380		111500	
	57510		41700	
TRIP700(B)	188800	174010	124000	114660
	202950		154000	
	130280		66000	

Comparing the results with EDM and RM (Table 4.8 and Table 4.9) , it may be observed that the machining method has minor effects on crack initiation. Both materials exhibit similar fatigue lives ((A):113860 cycles with EDM-107770 cycles with RM, (B):175150 cycles with EDM-174010 with RM). The average fatigue life for crack initiation was estimated at 80300 and 114660 cycles for TRIP700(A) and (B) steel, respectively. These average values are in quite good agreement with the values presented in Table 4.8, taking into account the dispersion of the fatigue crack growth results presented in Fig. 4.25.

4.5.2 Fractographic observations

Stereoscopic observations of the fracture surface of notched specimens revealed that fatigue cracks (in the majority of the specimens tested) initiate at the free edge adjacent to the notch, most probably due to less constraint for development of slip systems. In Fig. 4.26 a specimen with typical fatigue segment characteristics including the crack initiation section, fatigue crack growth regime and fast fracture region are shown. In the fracture surface of Fig. 4.26 the crack initiates at the free edge surface of the notch area and is advancing radially from the corner edge, towards the mid-thickness direction.

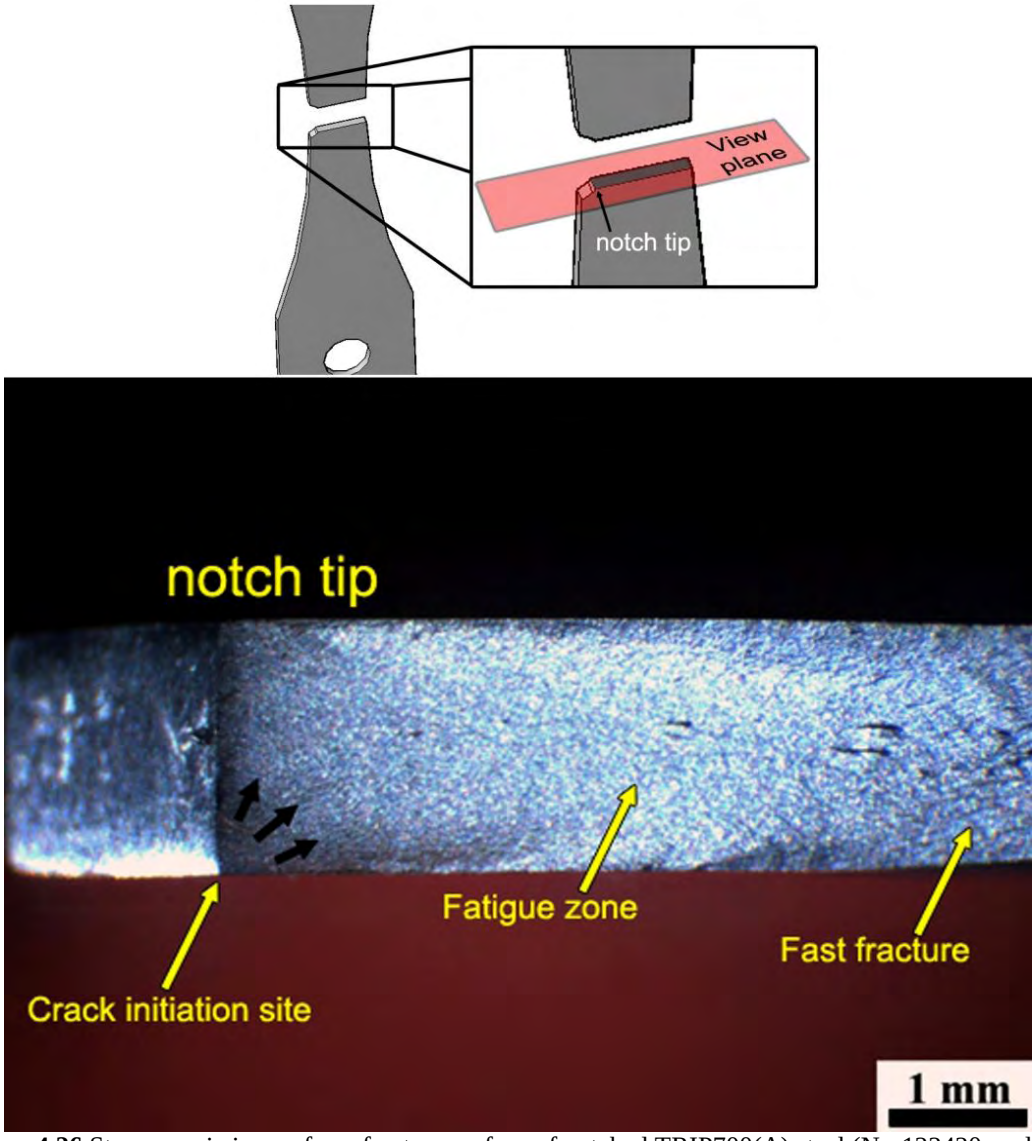

Figure 4.26 Stereoscopic image from fracture surface of notched TRIP700(A) steel (N_f=122420 cycles at σ_{max}=200MPa, the 250μm crack detected at 87700 cycles).

The fractographic details of Fig. 4.26 are characteristic for the majority of specimens examined. The first crack was observed at one specimen surface and after a certain number of cycles a second crack on the other edge was observed, propagating through thickness and leading eventually to crack coalescence and the formation of a single through thickness crack that propagates until failure of the specimen. A characteristic example is shown in Fig. 4.27 where replica observations in TRIP700(B) steel specimen at 120000 cycles revealed the existence of a 211μm crack only at one side (side A) of the specimen.

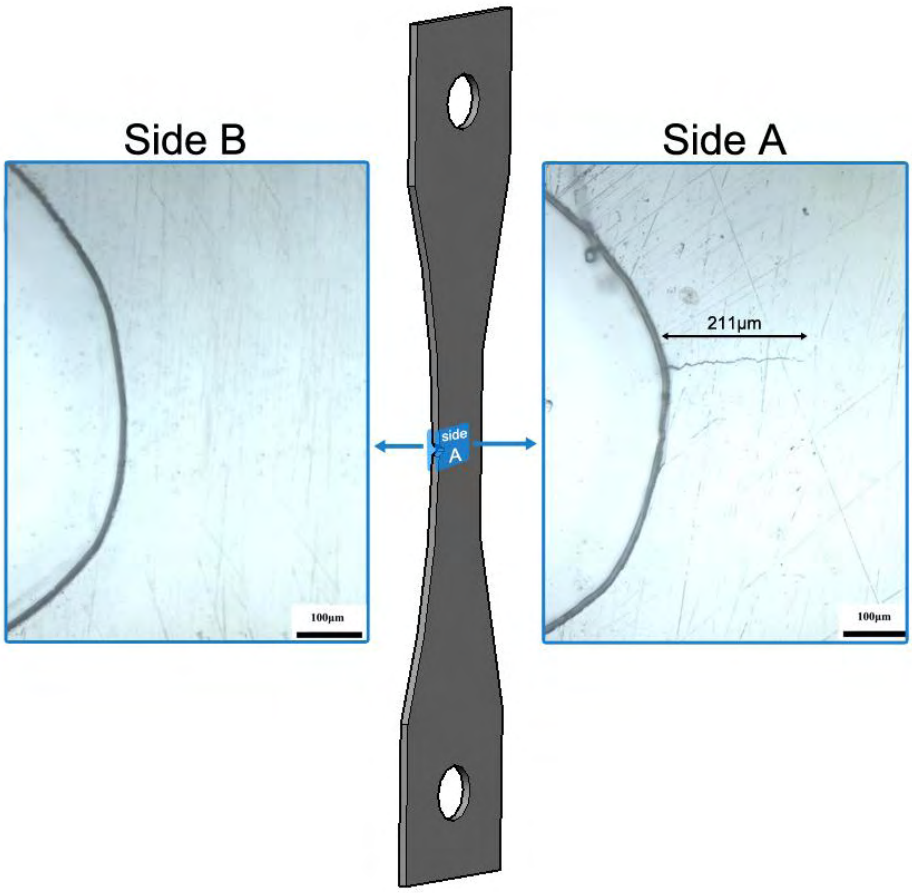

Figure 4.27 Lateral replica images in TRIP700(B) steel at 120000 cycles showing the onset of an edge surface crack (N_f=188800cycles at σ_{max}=200MPa).

CHAPTER 5

Estimation of fatigue crack initiation

In the present Chapter a methodology for the prediction of fatigue crack initiation in notched TRIP steel specimens is proposed. The methodology takes into account the local elastoplastic stress-strain behavior at the notch root during the first loading event in the cyclic history and predicts the life for crack initiation using the cyclic material properties of the material based on established models for notched fatigue analyses (Neuber Rule, SED criterion). A case study for prediction of crack initiation based on a fracture mechanics approach is also considered and the analytical results are compared against experimental data produced in section 4.5 in order to assess which methodology presents more reliable predictions. In the analysis, discussion is included for the influence of RA transformation effect in the obtained results.

5.1 Problem Definition

Methodologies for estimation of notched fatigue crack initiation usually rely on empirical fatigue concepts and the use of simplified assumptions to encounter the complex problem of multiscale fatigue damage leading to onset of cracking. A common, logical assumption used for crack initiation problems is that a material element volume at the root of the notch is subjected to low cycle fatigue conditions and that fatigue damage at the material element is equivalent to the damage of a macroscopic specimen when subjected to similar cyclic conditions.

In the case of TRIP steels, assessment of crack initiation becomes even more complex due to the phase transformation effect and requires a thorough understanding of how damage accumulates and initiates in a multiscale perspective, since RA transformation is strongly affected by the deformation mode [64], stress state [65], strain rate and slight variations in the chemical composition [7]. While limited experimental and analytical research exists on this problem, from the available research findings it was shown that the transformation of RA in front of the crack tip, inside the monotonic plastic zone [91], acts in favor of suppressing the fatigue crack initiation and/or propagation through the plastic relaxation induced by the transformation [26-29]. Fatigue crack initiation in TRIP steels is also considered to be affected by many other parameters such as the stress state, the transformation rate, the initial volume fraction of RA, the carbon content of RA and martensite, the initial defects (e.g. voids), the locations of the neighboring austenite grain and martensitic islands and the amount of martensite produced [123].

Although such effects are important in crack initiation analyses, they are very difficult to simulate since available theories fail to combine satisfactorily damage at a multiscale level (atomic/microscopic and macroscopic). In the proposed methodology the transformation effect is at first stage considered indirectly through the cyclic material parameters of the

materials as evaluated in Chapter 4. Subsequently, a more sophisticated method is discussed using a fracture mechanics approach to include the phase transformation effect on fatigue crack initiation of TRIP steels.

5.2 Notch strain analysis: The strain-life approach

Common approaches to notched fatigue behaviour are generally known as local stress–strain approaches. Their principle is based on relating the crack initiation life at the notch root to the crack initiation life of smooth laboratory specimens. The analysis of notched fatigue behavior with the local approach usually includes two steps. The first step involves the estimation of the local damage using a parameter such as stress, strain or plastic energy density at the notch root. The second step is to predict crack nucleation life based on uniaxial smooth specimen tests, where it is assumed that smooth and notched specimens encounter the same number of cycles to failure since they have the same local damage history. Therefore, predicting the local stress-strain behaviour is essential to the understanding of notch fatigue behaviour and of fatigue life prediction.

Two commonly used notch stress-strain models are the Neuber's rule and the Strain Energy Density criterion (SED). A review of these models was performed in [124], where the elasto-plastic stress-strain behaviour at notch roots under monotonic and cyclic loading was examined. Regarding multiaxial cyclic loading conditions, a unified expression of elastic-plastic notch stress-strain calculations in solid bodies was also proposed in [125].

5.2.1 Local strain approach

The LS approach was developed to overcome some of the problems inherent in the nominal stress (NS) approach, which uses the constant amplitude S-N fatigue curves to calculate the fatigue damage based on the nominal stress in the specimen. The principle

behind the LS approach, depicted in Fig. 5.1, is that smooth specimens tested under cyclic strain-control (LCF conditions) can simulate the fatigue damage at the notch root of an engineering component. Equivalent fatigue damage is assumed to occur at the notch root and in the smooth specimen when both are subjected to identical stress-strain histories. This is known as the *principle of equivalence*.

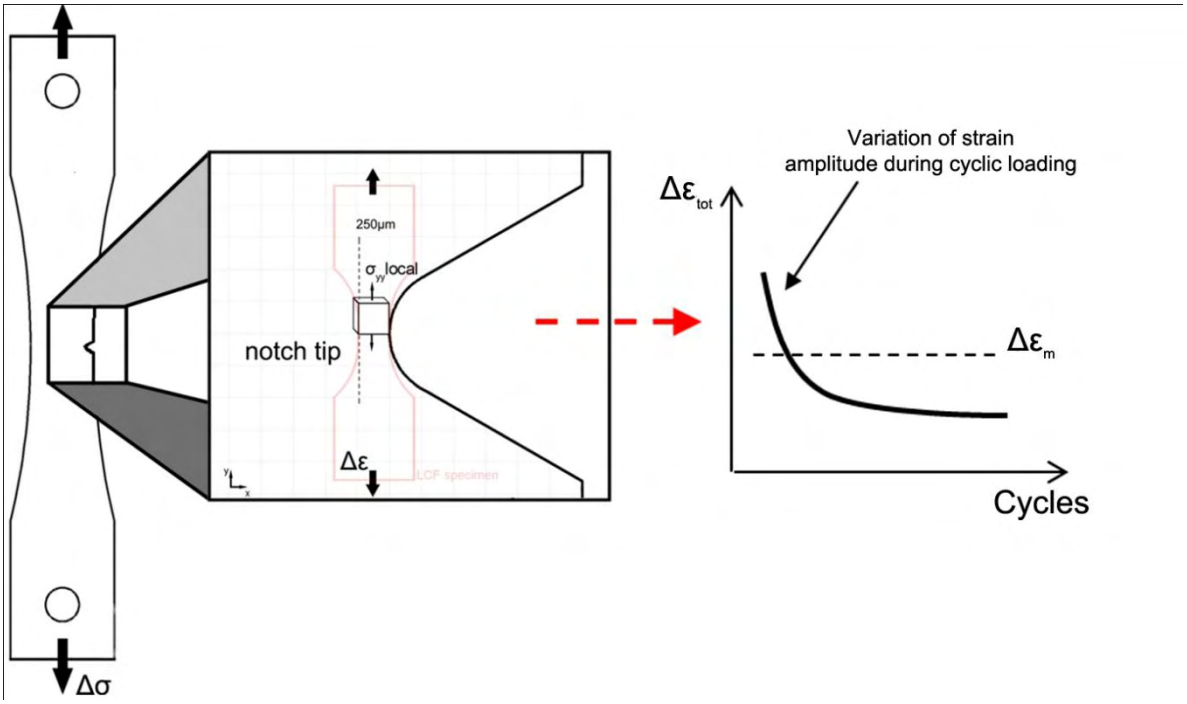

Figure 5.1 Material element ahead of the notch tip subjected to LCF conditions.

Since smooth specimens are tested under strain control, the LS approach uses the strain-life or ε-N curve for the prediction of life cycles. Estimation of crack initiation life is considered when the smooth specimen fails by assuming an equivalent stress state of the material volume in the notched specimen. Therefore, cycles to failure of the smooth specimen is considered to be equal to cycles to crack initiation of the notched specimen. This assumption although introducing specific limitations in the analysis, is considered acceptable to approach this type of problems.

5.2.2 Notch stress-strain estimation

The local stress-strain history at the root of a notch under external loading is not easy to assess analytically when the material is elastoplastically deformed. If the loading is fully elastic, then the material behaviour at the vicinity of the notch can be evaluated using the elastic stress concentration factor K_t. However, when -yielding at the notch takes place, the resulting behaviour is not known and numerical solutions provide a more accurate analysis of the local response. Approximate relationships such as the Neuber method or the Strain Energy Density (SED) criterion may be used to determine the local strain at the notch. In the following paragraphs a brief description of these two methods is given, which are used later in the analytical prediction of fatigue crack initiation life of TRIP steel specimens.

5.2.2.1 Neuber method

Neuber showed that for a shear-strained prismatic body with an arbitrary non-linear stress-strain law, the geometric mean of the stress and strain concentration factors (K_σ and K_ε) is equal to the theoretical stress concentration factor, K_t. This is expressed as follows:

$$K_t^2 = K_\sigma K_\varepsilon \tag{7}$$

The stress concentration factor, K_σ is the ratio of the notch root stress, σ, and the gross-section nominal stress, S:

$$K_\sigma = \frac{\sigma}{S} \tag{8}$$

The strain concentration factor, K_ε, is the ratio of the notch root strain, ε and the gross-section nominal strain, e:

$$K_\varepsilon = \frac{\varepsilon}{e} \tag{9}$$

Combining Eqs. *(7)-(9),* Neuber's rule can be re-written as:

$$\sigma\varepsilon = K_t^2 Se \tag{10}$$

For nominal elastic behaviour where e=S/E, Neuber' s rule is reduced to:

$$\varepsilon\sigma = \frac{\left(K_t S\right)^2}{E} \tag{11}$$

Generally, this is re-written in terms of stress and strain ranges for the case when the stress range remote to the notch is linear elastic:

$$\Delta\sigma\Delta\varepsilon \cong \frac{\left(K_t \Delta S\right)^2}{E} \tag{12}$$

Eq. (12) is widely used in fatigue life calculations using the LS approach. It shows that the product of the notch stress and strain ranges can be estimated by knowing the theoretical stress concentration factor, the applied stress range, and the elastic modulus of the material. Topper et al. in [126] were the first to refer to Neuber's work as "Neuber's rule". They showed that smooth specimen fatigue data could be used to adequately predict fatigue lives of notched members made from 2024 and 7075 aluminum alloys under fully reversed loading. They suggested the use of fatigue notch factor, K_f, instead of the theoretical stress concentration factor, K_t, for cyclic loading, modifying Eqs. (11) and (12) as:

$$\varepsilon\sigma = \frac{\left(K_f S\right)^2}{E} \tag{13}$$

$$\Delta\varepsilon\Delta\sigma = \frac{\left(K_f \Delta S\right)^2}{E} \tag{14}$$

Although Neuber's rule was derived for monotonic loading, it was applied to fatigue loading by Manson and Hirschberg in [119]. They suggested using for fatigue loading the cyclic stress-strain curve instead of the monotonic curve. Thus, solving simultaneously Eq.(13) for maximum stress and strain (ε_{max},σ_{max}) and Eq. (5) for ε_{max} and σ_{max}, the notch root stress-strain at maximum loading can be estimated.

Modifying the Ramberg-Osgood relationship (Eq. (5)) by replacing the strain and stress with the strain and stress ranges, respectively and assuming a masing factor of 2 (symmetric deformation behaviour in tension and compression), Eq. (5) yields in:

$$\Delta\varepsilon = \frac{\Delta\sigma}{E} + 2\left(\frac{\Delta\sigma}{2K'}\right)^{1/n'} \tag{15}$$

Solving simultaneously Eqs. (14) and (15) the cyclic notch stress and strain amplitudes can be estimated. With the evaluation of σ_{max}, ε_{max}, $\Delta\sigma$, $\Delta\varepsilon$ the values of σ_{min},σ_m,ε_α,σ_α can also be estimated.

5.2.2.2 Strain energy density criterion (SED)

An alternate approximate method is the Strain Energy Density (SED) criterion proposed by Molski and Glinka [127]. In this approach, it is assumed that the strain energy density at the notch root does not change significantly if the localized plasticity is surrounded by predominantly elastic material (Fig. 5.2).

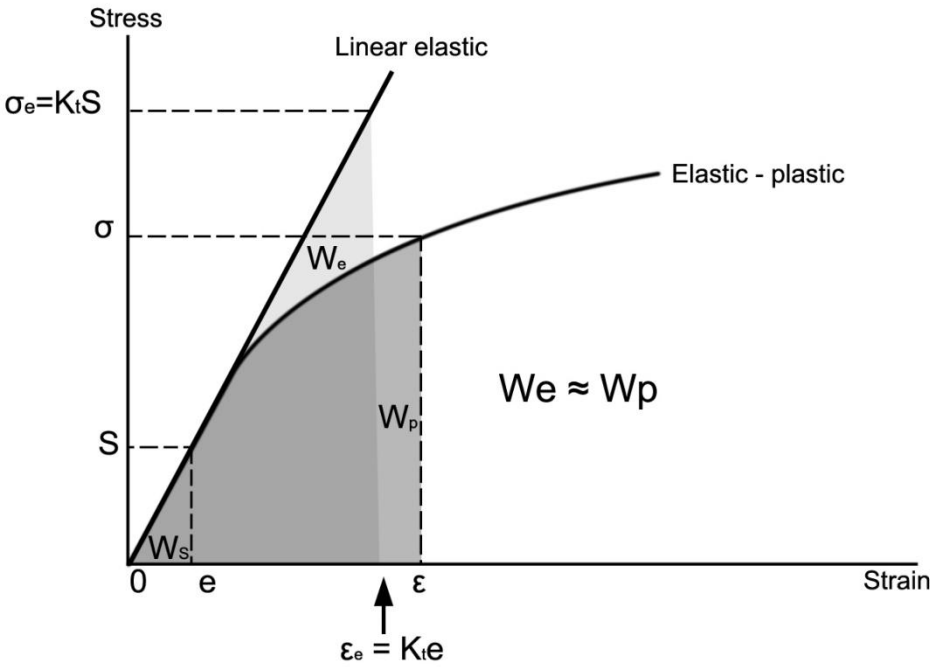

Figure 5.2 Graphical representation of the SED criterion.

Based on this assumption, computation of the strain energy density at the notch root will yield identical results for either the elastic or the elastic-plastic material law. The SED criterion has the following form:

$$W_e = W_p \Rightarrow \frac{1}{2}\frac{\left(K_t S\right)^2}{E} = \int_0^{\varepsilon} \sigma_{(\varepsilon)} d\varepsilon \Rightarrow \frac{\left(K_t S\right)^2}{E} = \frac{\sigma^2}{E} + \frac{2\sigma}{n+1}\left(\frac{\sigma}{K}\right)^{1/n} \quad (16)$$

where S is the gross-section nominal stress and $\sigma_{(\varepsilon)}$ is the notch root stress as a function of ε. For a given nominal stress S, the notch stress and strain during monotonic loading can be calculated solving simultaneously Eqs. (5) and (16).

With the use of Eq. (5) for maximum stress and strain (ε_{max},σ_{max}) and Eq. (16) for $\sigma=\sigma_{max}$ and $S=S_{max}$, the notch root stress-strain at maximum load can be calculated.

For cyclic loading, Eq.(16) can be re-written in terms of stress and strain ranges, while the material monotonic deformation properties (K and n) can be replaced by the cyclic deformation properties (K' and n') resulting in the following equation:

$$\frac{\left(\Delta\sigma\right)^2}{E} + \frac{4\Delta\sigma}{n'+1}\left(\frac{\Delta\sigma}{2K'}\right)^{1/n'} = \frac{\left(K_t \Delta S\right)^2}{E} \quad (17)$$

Solving simultaneously Eqs. (15), (17) the cyclic notch stress and strain amplitudes can be calculated.

According to [128] the SED model is more reliable compared to Neuber' s rule when predicting elastic-plastic notch stresses and strains. On the other hand Sharpe et al. [129] claim that Neuber' s rule provides better results in cases where plane stress conditions are present. In some cases local strain solutions extracted from finite element analyses or experimentally determined values, lie between the predictions from the SED criterion and Neuber' s rule, with the latter giving unconservative estimations for a given value of K_tS (e.g. [127, 129]). In these instances, it is difficult to determine which model describes better the experimental data. It has been suggested in [129] that estimations made from SED criterion

and Neuber' s rule will give lower and upper limits on the local strain, which can be used to bound an uncertainty field for the life prediction.

The analytical expressions provided above, consider the notch stress-strain response for completely reversed straining, $R=\varepsilon_{min}/\varepsilon_{max}=-1$. In strain-histories with a mean strain, usually mean stress relaxation occurs due to the presence of plastic deformation. To account for the mean stress effect in fatigue life prediction for the elastic strain component the Smith-Watson and Topper parameter (SWT parameter) or the Morrow's mean stress method are oftenly used [130]. The SWT parameter [131] which is used in the present thesis is:

$$\sigma_{\max}\varepsilon_a = \frac{\left(\sigma_f^{'}\right)^2}{E}\left(2N_f\right)^{2b} + \sigma_f^{'}\varepsilon_f^{'}\left(2N_f\right)^{b+c} \tag{18}$$

where $\sigma_{max}=\sigma_m+\sigma_\alpha$ and ε_α is the alternating strain. Eq. (18) is based on the assumption that for different combinations of strain amplitude, ε_α and mean stress, σ_m, the product $\sigma_{max}\varepsilon_\alpha$ remains constant for a given fatigue life. If σ_{max} is zero, then Eq. (18) predicts infinite life, which implies that tensile loading must be present for fatigue fracture to occur.

5.3 Fatigue crack initiation analysis

Calculations of the local stress-strain history may be combined with an appropriate notched fatigue analysis in order to estimate fatigue crack initiation as the number of cycles required to initiate the crack at the location of interest (notch tip). In this approach, the calculated fatigue life is strongly dependent on the material length scale at the notch root and the values of notch strains, which usually lack certain accuracy when elastoplastic material behaviour is involved due to the complex stress state occurring at the tip of the notch. For this purpose appropriate numerical analyses in order to obtain greater accuracy of strains at the local elastoplastic material region are usually adopted.

Under this viewpoint, in the Thesis a suitable finite element model was developed for the determination of the local strains and stresses of a material element volume at the notch tip during a far-field loading. The criteria for the selection of length of the material volume are analyzed in the following section. The numerical results are then incorporated in the notched fatigue models described previously, to obtain the critical number of cycles for fatigue crack initiation. The methodology, which is presented in the flow chart of Fig. 5.3 includes the following steps for prediction of the number of cycles for fatigue crack initiation for a single side V-notch specimen:

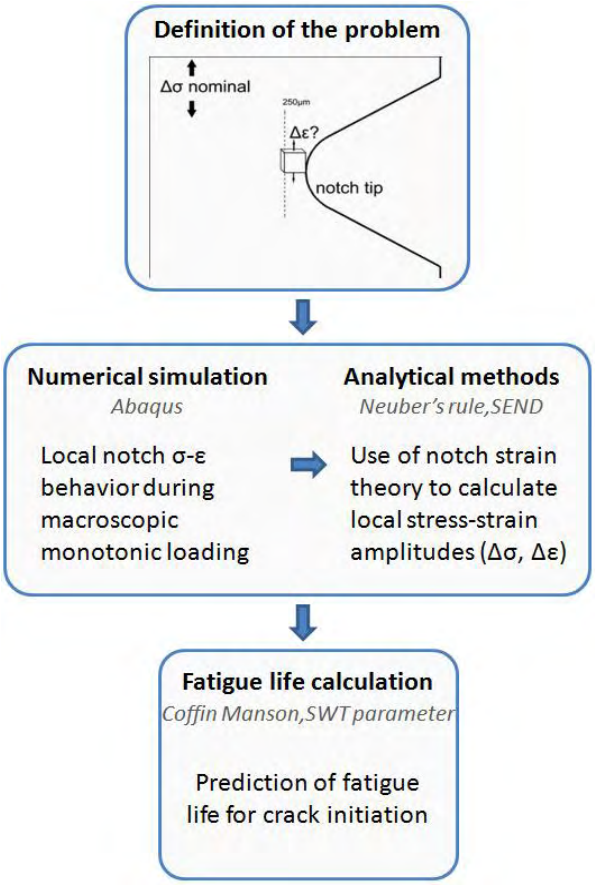

Figure 5.3 Methodology for estimation of crack initiation.

1. Determination of monotonic and cyclic material properties. Specifically the properties σ_y, E, n, K, n', K', σ_f', b, ε_f' and c as evaluated in Chapter 4 are required to provide the necessary material data for fatigue analysis.

2. Calculation of the localized stress-strain curve at the vicinity of the notch during external tensile loading. For this purpose an elastoplastic numerical analysis, with the true stress-strain data is performed using an appropriate FE model in order to relate the macroscopic stress-strain behaviour during the initial loading event of the cyclic history, to the local behaviour at the notch tip. The numerical model is described analytically in section 5.4.1.
3. The numerical results of step 2 are used as input in notched fatigue models for calculation of fatigue life for the specific loading conditions.

5.3.1 Assumptions of the methodology

Fatigue analysis for the prediction of crack initiation life adopts certain assumptions for simulating the involved damage mechanisms. The methodology considers that crack initiation from the notch tip is associated with failure of an elementary material volume adjacent to the notch root, which is subjected to low cycle fatigue conditions. The material element is located at the corner of the notch tip, at the free surface of the specimen as depicted in Figure 5.4, and has a width along the x-direction (plane of crack propagation), equal to 250μm (Fig. 5.4).

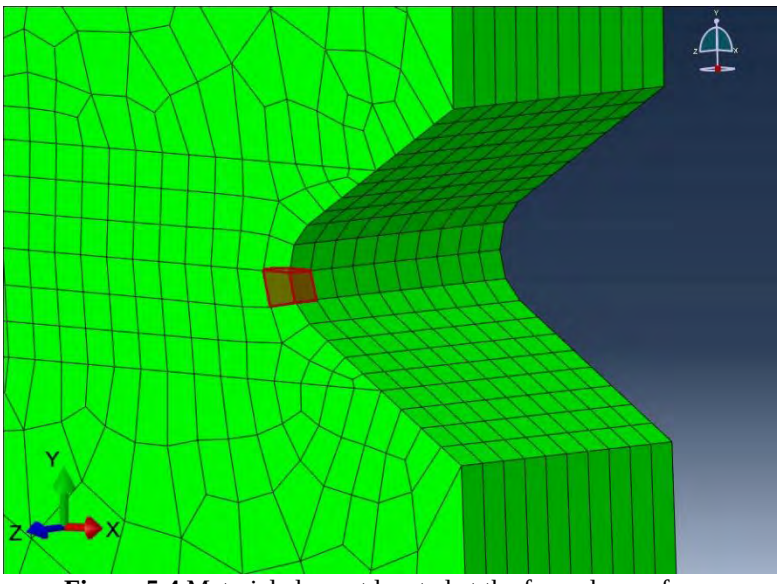

Figure 5.4 Material element located at the free edge surface.

The criteria for selecting the specific element location are based on the fractographic observations discussed in Chapter 4 according to the experimental findings (Figs. 4.26 - 4.27), cracks originate as corner cracks at the tip of the notch and then propagate radially before coalescence occurs into a single through thickness crack.

Selection of the 250μm width for the corner element satisfies the assumption that the size is large enough to consider conditions of an isotropic, homogeneous medium for valid implementation of fatigue equations, since it exceeds by far the magnitude of the critical microstructural parameter, which is the grain size of the materials.

Taking the above into account, fatigue failure of the material element designates crack initiation, which for the case examined is considered as the development of a 250μm corner crack at the tip of the notch on the outer specimen surface. In the analysis, based on the local strain approach (section 5.2.1), it is considered that the material element volume is subjected to equivalent fatigue damage as an individual specimen tested uniaxially in laboratory conditions. This hypothesis contains specific shortcomings due to i) the size effect involved, ii) the fact that the material element volume undergoes deformation constraints from adjacent elements, which are not present in laboratory conditions, iii) the deformation state in the material element is not strain controlled as in the case of the low cycle fatigue test. Strain triaxiality at the notch tip is not expected to be an influential factor in the fatigue behavior examined due to the selection of the corner element promoting plane stress conditions.

5.4 Numerical simulation of the local stress-strain behaviour at the notch tip

Analytical methods for calculation of the stress-strain field in the vicinity of the notch are based on assumptions which may not be valid in certain situations. For instance, Neuber' s rule does not account the multiaxial stress state present at the root of the notch. The latter

method provides quite accurate results for thin sheets (plane stress conditions) but is conservative by predicting strains higher than actually measured. Fatemi et al. [124] compared the elasto-plastic notch stress strain behaviour obtained by using Neuber's rule and SED method with experimental and finite element results for specimens with different K_t values. From their results it was clear that Neuber's rule works best when the vicinity of the notch is in a state of plane stress while Glinka's rule for plane strain conditions. Approximate relationships such as Neuber's rule and SED method are useful to provide first estimations of the notch root stress/strain behaviour, but a more accurate prediction would require further computational study with a finite element software. Furthermore, being macroscopic, analytical methods they do not account for certain microstructural influences, which control the material's plastic deformation behaviour. For instance, the phase transformation effect contributes to the plastic straining under external loading and is an important parameter on the TRIP steel behaviour.

5.4.1 Finite element model

To obtain a representative local stress-strain behaviour at the notch root, the elasto-plastic stress-strain behaviour of the material element of Fig. 5.4 was simulated numerically under external monotonic loading using the Abaqus finite element (FE) software. The element behavior was simulated for a monotonic loading corresponding to a maximum tensile stress of 200MPa, which is the quarter of a cycle in the fatigue test performed in Chapter 4. For the simulation where the specimen is subjected to a far-field tensile loading, a 3D finite element model was constructed and a step loading analysis was performed (Fig. 5.5).

The values of the elastic material properties used in the analysis are Poisson's ratio ν=0.3 and Young's Modulus E=205.9 GPa for the four steels examined. Beyond the elastic region an isotropic hardening behaviour was implemented to describe each material's stress-strain

behavior, which uses the calculated true stress-strain plastic curve data presented in section 4.2.

During loading a fixed constraint was applied in the upper bolt hole (Fig. 5.5), which simulates the conditions of specimen fixture during testing. The tensile loads resulting in the stress of 200MPa are 4396N and 3538N for steels (A) and (B), corresponding to a thickness of 1.75mm and 1.45mm respectively. For steels variants HTxI having a thickness of 0.75mm, the load is 1758 N.

In the numerical analysis linear hexahedral solid 3D elements were used. The element width at the notch tip was set to 250μm, the characteristic crack length assumed for crack initiation in section 4.5. The fine mesh consisted of a total number of 25650 and 30130 elements for steel (A) and (B), respectively. For the HTxI variants, one common solid model was used on account of similar specimen geometry, which consisted of 10047 linear hexahedral solid 3D elements. Optimization of the mesh in the model was performed by increasing the element size with increasing distance from the notch tip in order to reduce the computational time.

Mesh sensitivity validation has also been performed with the use of finer mesh. The element width in the vicinity of the notch was reduced to 25μm and the monotonic simulation was repeated. The deviation of predicted notch stress-strain values with the finer mesh was lower than 4% compared to the results of the 250μm width element mesh. The latter findings imply that a finer mesh will have negligible effect on evaluation of results.

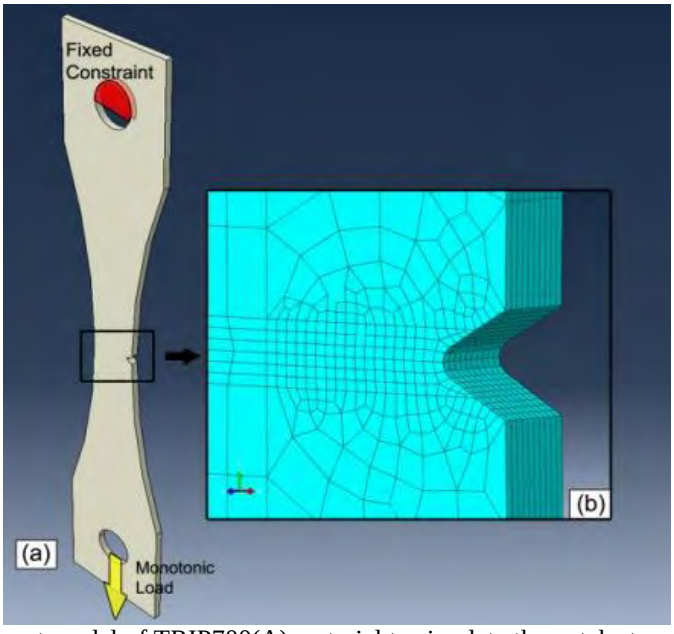

Figure 5.5 Finite element model of TRIP700(A) material to simulate the notch stress-strain behaviour. (a) Boundary conditions used in the simulation. (b) Meshing at the vicinity of the notch.

5.4.2 Numerical results

A stepped load increment was applied up to a far-field tensile stress of 200MPa. In Fig. 5.6 the calculated stress-strain behaviour of the corner element at the notch tip is presented for the examined TRIP materials, while in Figs. 5.7 - 5.8 details of the FE models with the distribution of normal stresses and strains in the loading direction are shown.

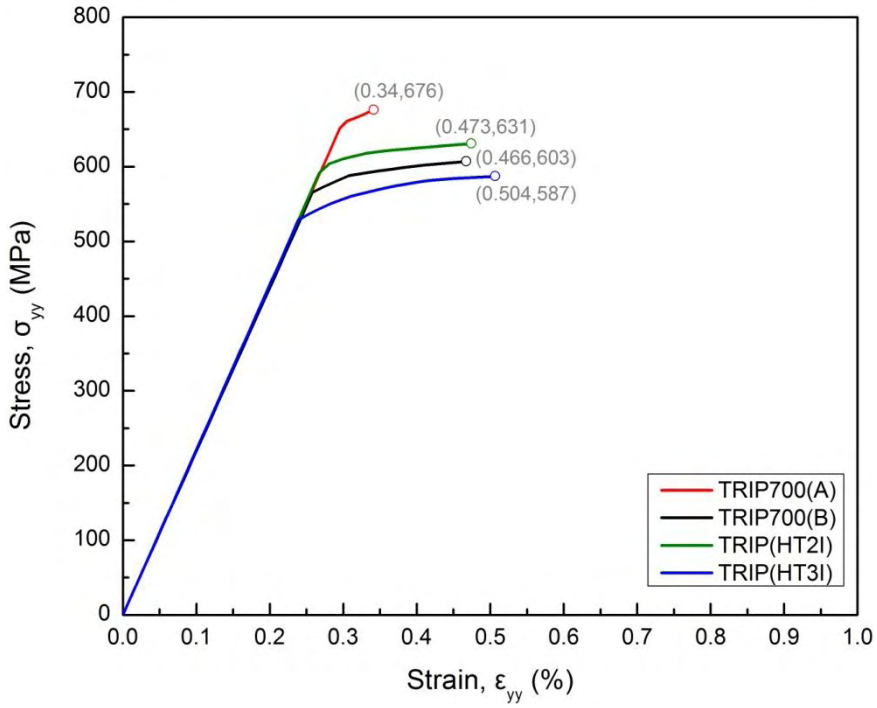

Figure 5.6 Normal stress-strain behaviour of the corner element at notch tip for TRIP700(A),(B),TRIP(HT2I) and TRIP(HT3I) steels.

The maximum stress and strain (Figs. 5.7 - 5.8) is σ_{yy} =675.9MPa - ε_{yy} =0.0034 for material (A), σ_{yy}=606.9MPa - ε_{yy}=0.0046 for material (B), σ_{yy}=631MPa - ε_{yy}=0.00473 for material (HT2I) and σ_{yy}=587MPa - ε_{yy}=0.00504 for material (HT3I). As shown in the results of Fig. 5.6 local yielding at the notch tip takes place.

The maximum stresses and strains at the notch root can be calculated using the Neuber method or SED criterion by solving simultaneously Eqs. (3), (11) and Eqs. (3), (16), for incremental monotonic loading. In Fig. 5.9 the analytical local stress-strain results obtained using the Neuber and SED method are compared with the numerical results obtained from the finite element model.

By examining the results presented in Fig. 5.9 it can be noticed that the analytical results underestimate the numerical findings. In TRIP700(A) material, for a maximum notch strain of 0.0034 the predicted notch stress with the Neuber or SED criterion is underestimated by 33.4% (FEA prediction=676MPa, Neuber/SED=450MPa), while for TRIP700(B) material the difference is 33.5%. For TRIP(HT2I) and (HT3I) materials the predicted maximum notch stresses from Neuber/SED criterion are underestimated 42% and 36.5% respectively.

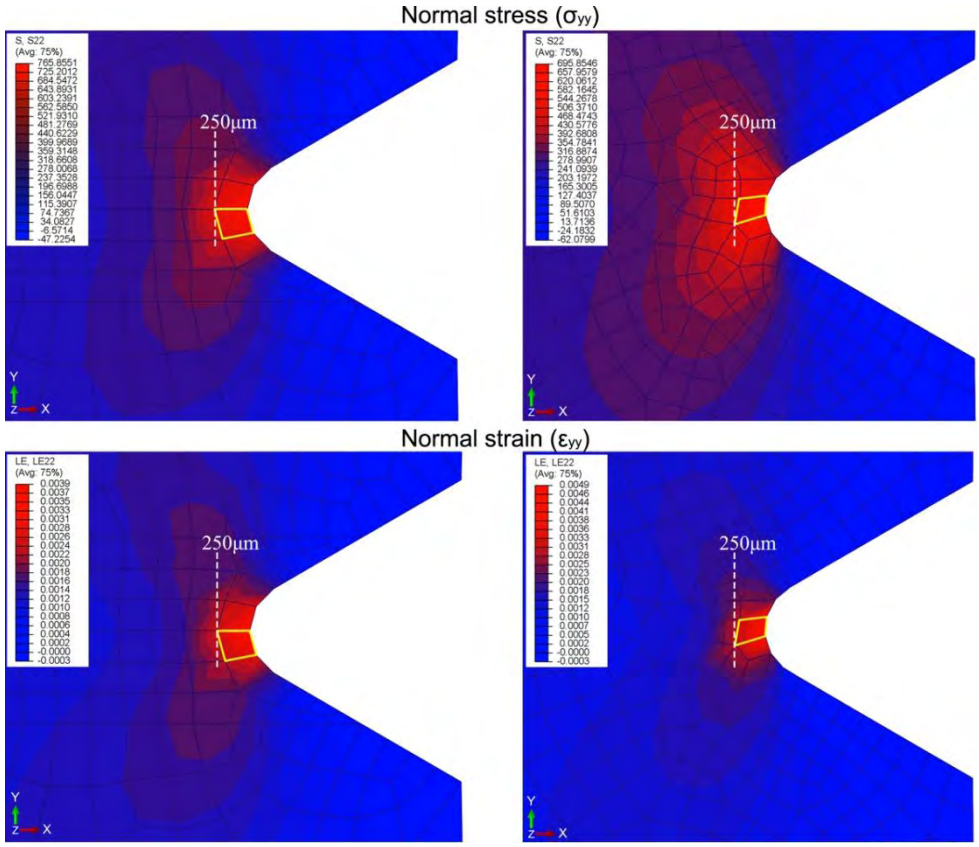

(a) **(b)**

Figure 5.7 Side view of the model. Normal stress and strain distribution at the vicinity of the notch for (a)TRIP700(A) and (b)TRIP700(B) material.

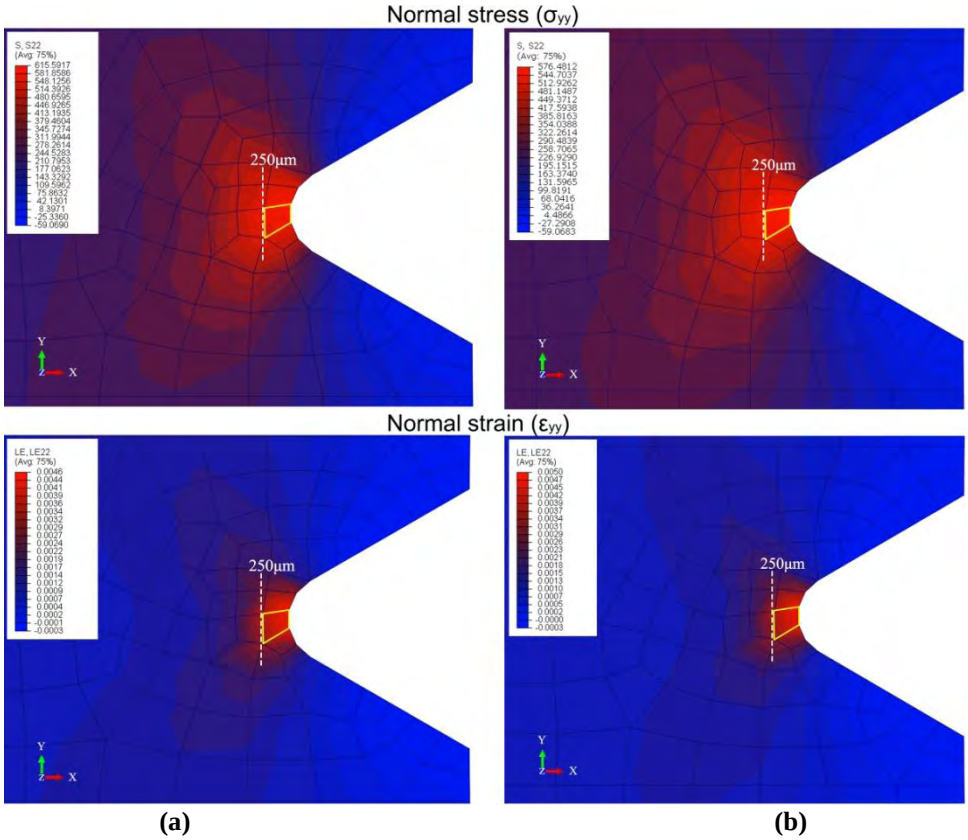

(a) **(b)**

Figure 5.8 Side view of the model. Normal stress and strain distribution at the vicinity of the notch for (a)TRIP(HT2I) and (b)TRIP(HT3I) material.

As discussed earlier, Neuber's rule may overestimate the notch root strains under multiaxial stress state conditions while it provides more reliable results for plane stress conditions. Comparison of the analytical approximations with the FE analysis showed that the Neuber method and the SED criterion provide almost identical results, which are conservative compared to the results of the FE model and hence may be better used as first estimations [124]. However, underestimation of notch root strains by quite large margins have been also reported elsewhere [118, 124].

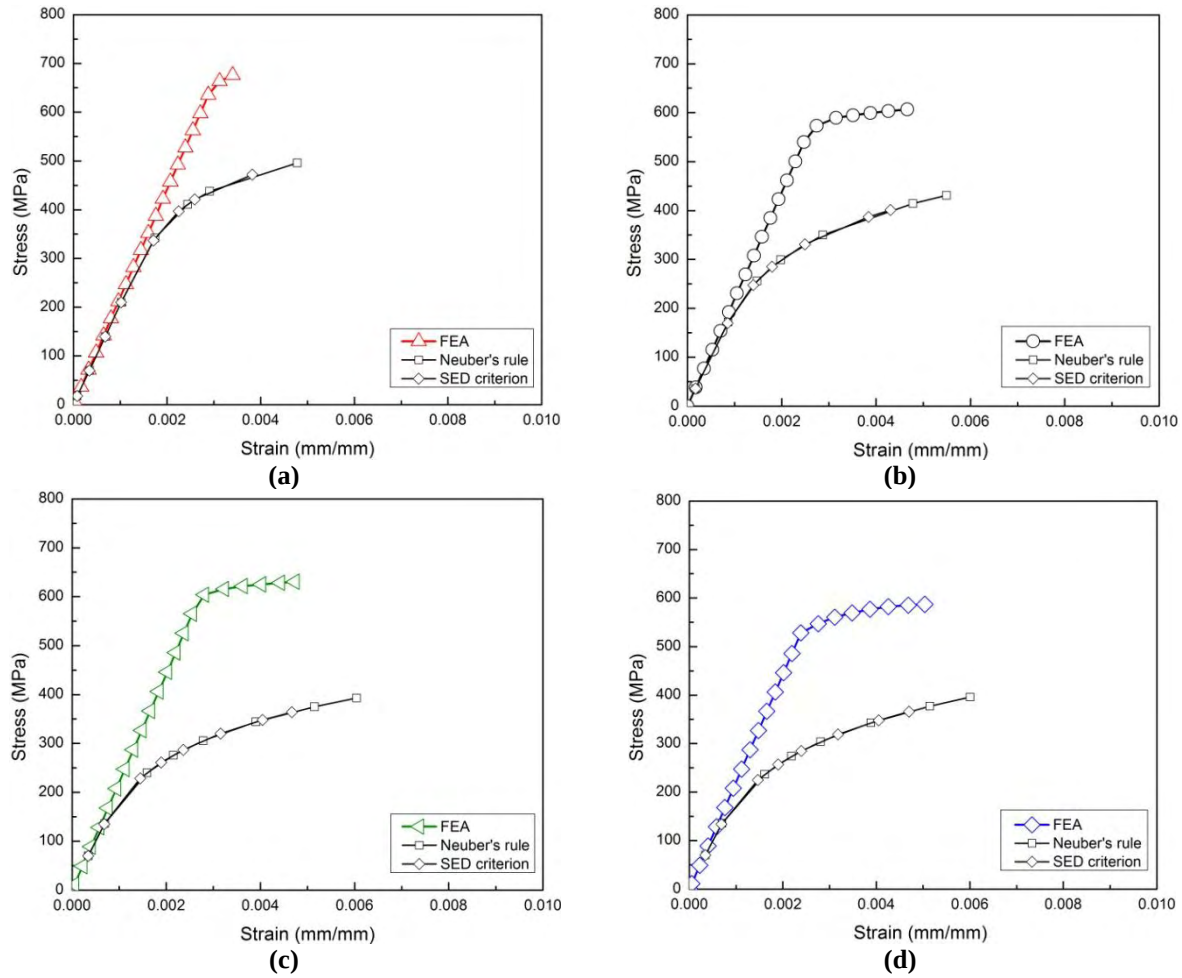

Figure 5.9 Notch root strains from FEA, Neuber's rule and SED criterion under monotonic tensile loading for, (a) TRIP700(A), (b) TRIP700(B), (c) TRIP(HT2I) and (d) TRIP(HT3I) steel.

5.5 Notched fatigue analysis

A notch fatigue analysis is performed next based on the numerical results of section 5.4.2 for calculation of the number of cycles for crack initiation, as explained in section 5.3.

Implementation of the numerical results in the fatigue analysis aims to provide a more reliable prediction due to a more accurate calculation of local strains at the vicinity of the notch compared to the analytical methods.

The case that was simulated analytically was the one studied experimentally in section 4.5. A flowchart of the analytical simulation for prediction of crack initiation life and the steps involved in the analysis is shown in **Fig.** 5.10.

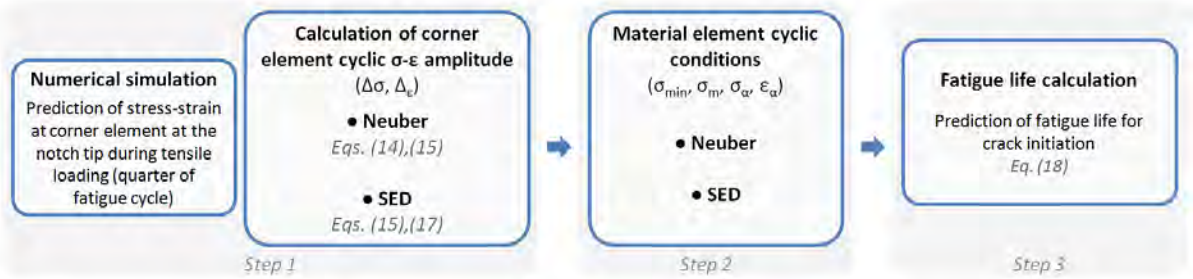

Figure 5.10 Flowchart of the steps used in the fatigue analysis for prediction of fatigue life corresponding to crack initiation.

The monotonic material properties σ_y, n, K from Table 4.2 and the cyclic properties n', K', σ_f', b, ε_f', c, K_t, K_f from Tables 4.5, 4.7 were used as input parameters in the analysis. Since there were no experimental data concerning the K_f values of (HT2I) and (HT3I) steels, the value of K_f=3.24 obtained experimentally for (A) and (B) materials was chosen also for the HT materials. The predicted fatigue lives in cycles for each material examined, is presented in Table 5.1

It is evident from the results of Table 5.1 that fatigue predictions are very sensitive to the calculated local stress-strain history at the notch root. Small differences in notch stress-strain of the order of 5-6% may result in significant differences in predicted fatigue life of the order of 34% of Table 5.1. This observation highlights the importance of a reliable prediction of the notch strain values as it is attempted here with the numerical analysis. The SED criterion predicts in general higher values of notch stress and strain compared to Neuber's method, leading to more conservative fatigue life predictions. Both methods overestimate the experimental results. The plane stress conditions corresponding to the element examined in

Fig. 5.4 do not seem to favor the prediction of the Neuber method here possibly due to other factors associated with the microstructure and TRIP effect. The above trend is in line with observations presented in literature, since Neuber's rule considers the stress state to be uniaxial at the notch root, which leads to less conservative results.

A comparison of predictions using in the fatigue analysis the numerical notch stress-strain results, and the results from the Neuber or SED method is performed in Table 5.2, using the experimental findings as verification. For the majority of materials examined, the numerical results improve the fatigue analysis and bring it closer to the experimental results compared to the analytical solutions, although some underestimation of the number of cycles for failure compared to the experiment is present.

The largest deviation between analysis (with numerical stress-strain notch results) and experimental results is observed for material HT2I, which exhibits the shortest fatigue life for initiation of the 250μm crack. For that case, a noticeable underestimation of the experimental fatigue life exists, whereas the analytical solutions, which in all other cases overestimate significantly the experiment here provide a good approximation. A possible explanation for the inferior fatigue performance of HT2I material may be the extensive cyclic softening under cyclic plastic strains, even when the plastic strain component is not prominent, as discussed in the experimental findings of section 4.3.3 (Fig. 4.15). This cyclic softening behavior, when extrapolated to the notch tip, in a stress controlled experiment may degrade the resistance to fatigue crack initiation due to the local, gradual increase of strain amplitude.

Table 5.1 Predicted fatigue life for the formation of a 250μm crack using FEA results.

	TRIP700(A)		TRIP700(B)		TRIP(HT2I)		TRIP(HT3I)	
	Neuber	**SED**	**Neuber**	**SED**	**Neuber**	**SED**	**Neuber**	**SED**
	Cyclic loading between 200-20Mpa							
Notch stress amplitude, σ_α (MPa) [a]	290	312.5	275.5	285	286.2	302	283	295.5
Notch strain amplitude, ε_α [a]	0.00141	0.00153	0.00149	0.00156	0.00144	0.00154	0.00146	0.00155
	Fatigue life for loading 200-20MPa							
Notch mean stress, σ_m (MPa)	385.7	363.2	327.4	317.9	344.5	328.7	303.9	291.4
Maximum notch stress, σ_{max} (MPa) [b]	676	676	603	603	631	631	587	587
Product of $\varepsilon_\alpha\sigma_{max}$	0.9525	1.0311	0.8964	0.9417	0.9089	0.9725	0.8553	0.9081
Predicted fatigue life, N_f (cycles) [c]	***53800***	***37890***	***104500***	***77500***	***16500***	***13090***	***51000***	***39050***

[a] Calculated with Eqs. (14),(15) for Neuber and (15),(17) for SED criterion, [b] Calculated with FE, [c] Solved with Eq. (18)

Table 5.2 Comparison of predicted fatigue life for crack initiation with experimental data.

	TRIP700(A)		TRIP700(B)		TRIP(HT2I)		TRIP(HT3I)	
	Neuber	**SED**	**Neuber**	**SED**	**Neuber**	**SED**	**Neuber**	**SED**
Predicted fatigue life without FE calculations, N_f (cycles) [a]	180000	130000	650000	560000	48300	40800	178000	151000
Predicted fatigue life with FE calculations, N_f (cycles)	53800	37890	104500	77500	16500	13090	51000	39050
Experimental investigation, N_{ini} (cycles)	***66040*** [b] ***80300*** [c]		***108970*** [b] ***114660*** [c]		***69630***		***91130***	

[a] Calculated with Eqs. (5), (13), (16) implemented in Eq. (18), [b] cycles with EDM method, [c] cycles with RM method

5.6 Prediction of crack initiation based on a fracture mechanics approach: A case study

In the concept described previously, crack initiation is considered as the onset of a 250μm crack due to failure of a material volume at the notch tip, which is subjected to LCF conditions. For a more comprehensive understanding of the fatigue crack initiation problem, a more rigorous approach based on fracture mechanics is attempted here and is presented as a case study. This approach is based on the prediction of the number of cycles required for a small crack (not microstructurally short) to initiate at the root of the notch and propagate to an increment of 250μm. To accomplish this, it is considered that crack initiation occurs as the onset of a corner crack at the free edge of the notch, as it has been experimentally observed in section 4.5.2 of the present Thesis, due to fatigue failure of a material element at the free edge. A more realistic approximation of fatigue crack initiation requires that the occurring fatigue damage resulting to failure of the material element takes place at a smaller scale; therefore the dimensions of the material element examined in the previous section (section 5.5) are reduced to 50x50μm. After onset, the corner crack propagates under in mode I until it reaches a final length of 250μm. To perform the analysis the calculation steps presented in sections 5.4 and 5.5 are used to predict the number of cycles for failure of the corner element (crack initiation), and then a fracture mechanics analysis is implemented to calculate the number of cycles for the growth of the crack until a final length of 250μm from the notch tip (crack propagation).

5.6.1 Crack initiation (onset of 50μm crack at the notch tip)

In Fig. 5.11(a) the finite element model developed in section 5.4.2 is presented with a finer mesh (25μm element size) to expand the notch stress- strain analysis at a characteristic distance of 50μm from the notch tip for a far field tensile stress of S=200MPa. In Figs. 5.11(b) and (c) the distribution of local stress and strain with the distance from the notch tip is

shown. The maximum stress and strain calculated at a distance of 50μm from the notch root are σ_{yy}=630MPa and ε_{yy}=0.007128. Using these values in the analytical model described in section 5.5 the cycles for failure of the material element, are 80300 and 60500 cycles with the Neuber and SED criterion, respectively.

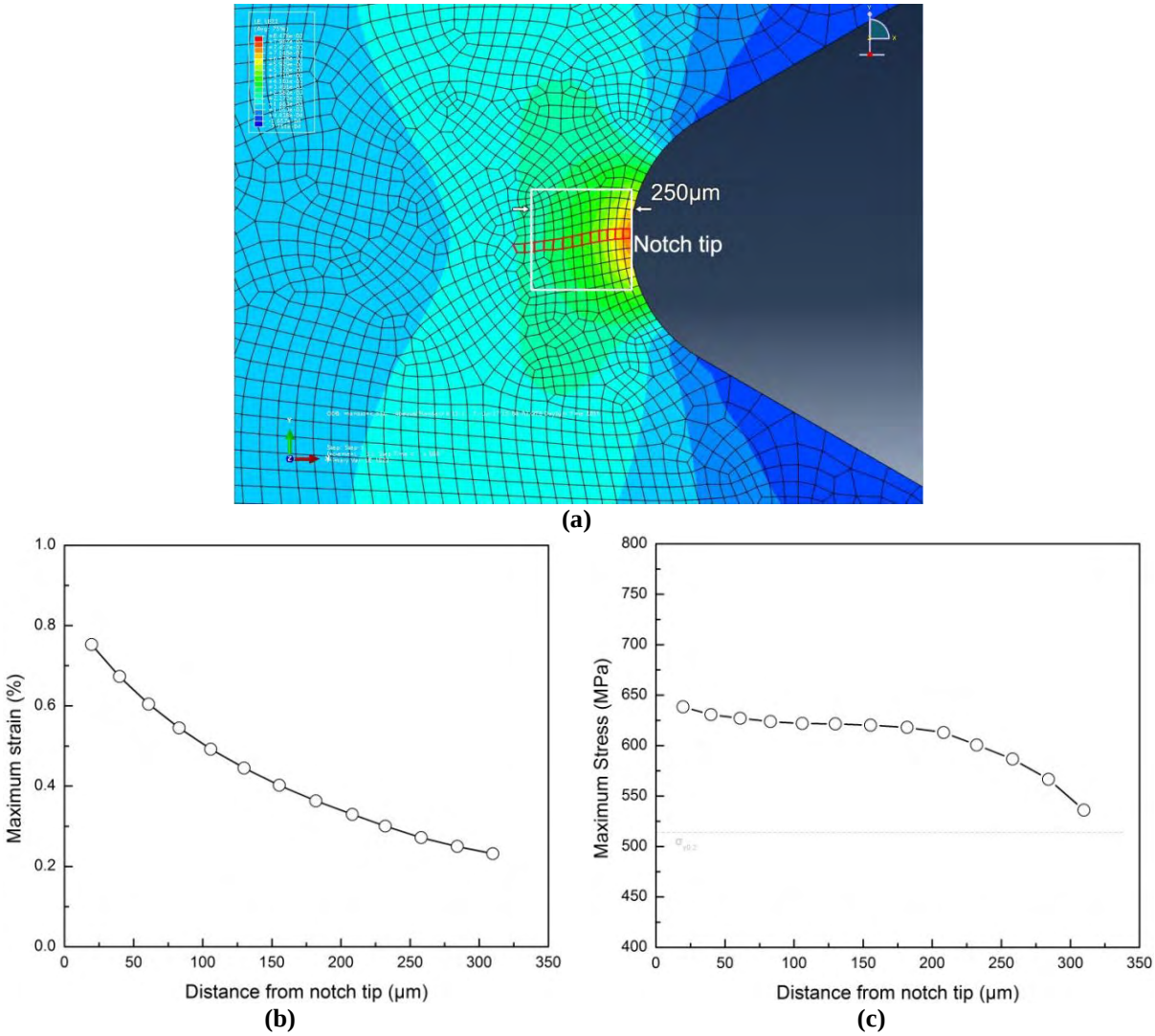

Figure 5.11 (a) Normal strain distribution in TRIP700(B) model with finer mesh (25μm element size), (b) maximum strain and (c) maximum stress distribution vs. distance from notch tip for a remote stress of 200MPa.

5.6.2 Crack propagation

5.6.2.1 LEFM limitations in fatigue crack growth behavior from notches

In many design situations, Linear Elastic Fracture Mechanics (LEFM) analyses allow a direct comparison of fatigue crack growth behavior between engineering components and

laboratory specimens using the stress intensity factor range, ΔK. Although this is an accepted methodology in the case of long cracks, for short crack problems limitations of continuum mechanics lead to underestimation of the fatigue crack growth rate [132]. The limitations may arise in the case of microstructurally short cracks due to the length of the crack being comparable to the microstructural scale of the material (e.g. grain size) or to the plastic zone size at the crack tip. For physically small cracks (typically smaller than 0.5 mm) with length exceeding the microstructural scale of the material, limitations may occur when the short crack is embedded within the plasticity of a notch [132, 133].

In the case examined here, the crack (50μm length) is significantly larger than the maximum grain size (9.47μm) and therefore cannot be considered to be microstructurally short. Also its cyclic plastic zone size $r_{cy}=1/8\pi(\Delta K/\sigma_{y0.2})^2$ =17.65μm [134] is smaller compared to its length. On the other hand the plastic zone at the notch root for a remote stress of 200MPa is approximately 300μm as calculated from Fig. 5.11 which means that the stage of short crack propagation takes place inside the plasticity of the notch.

Although originally developed for mostly elastic conditions, LEFM concepts can be used for short cracks embedded in the inelastic field induced by the presence of notch. Characteristic paradigms are the correlative model by Leis [133] which is explained in more detail in the next paragraph, the concept of El Haddad et al. [135, 136], which introduces a threshold crack length as minimum for applicability of LEFM and models based on the determination of short crack growth parameters [e.g. [137]]. The concept of Leis has been found to be more suitable for the current investigation, since the threshold crack length for applicability of LEFM exceeds the final crack length in the case examined.

5.6.2.2 LEFM correlative model of notched specimen and crack propagation

In the work of Leis [133] a correlation of LEFM concept has been proposed when the crack is completely submerged in the notch tip plastic zone and thus bulk plasticity conditions

dominate the growth behavior. Since the notch inelastic filed does not transmit the far field stress and stress cycle to the crack in the same manner as would an elastic field, it is reasonably assumed that for a notched specimen subjected to a far field constant stress amplitude (load controlled), there is a material volume at the tip of the notch with it's deformation being displacement controlled (Fig. 5.12).

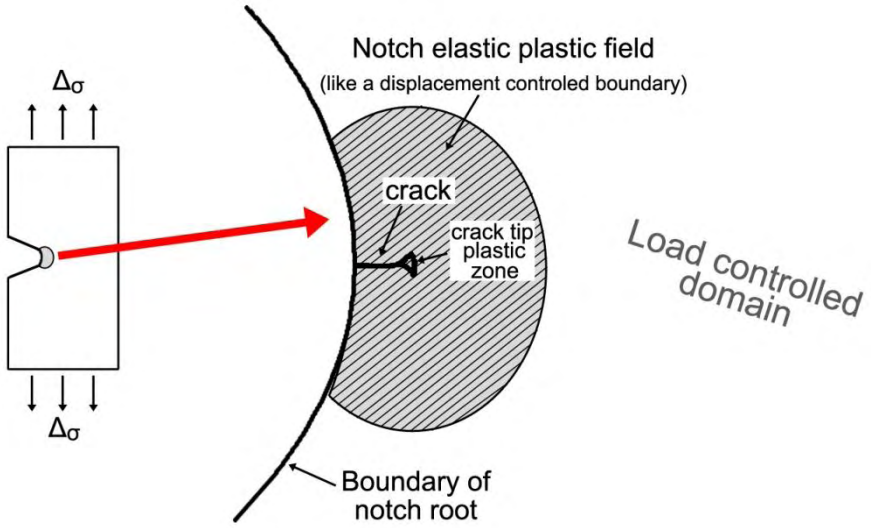

Figure 5.12 Displacement control of crack contained within notch plastic zone.

In the view of the above it is postulated by Leis [133] that the driving force for the above crack to grow in the notch inelastic field can be approximated by:

$$K_{mx} = 1.12\varepsilon_{mx}E_m\sqrt{\pi\alpha} \tag{19}$$

where ε_{mx} is the cyclically stable maximum strain in the material element at the depth of interest (in the absence of the crack), E_m is the monotonic modulus, 1.12 is the free surface correction factor and α is the length of the crack measured from the notch root. In Eq. (19) the product $\varepsilon_{mx}*E_m$ is primarily used to estimate a "pseudostress" in keeping with the linear elastic nature of LEFM. In [138], application of Eq. (19) in a pearlitic rail steel resulted in accurate prediction of the cracking behavior for cracks as small as 50μm.

Since the total fatigue crack would be fully embedded in the notch tip plastic zone and propagates under LCF conditions, the parameter ε_{mx} of Eq. (19) can be estimated as an average maximum strain within the length scale of 50μm to 250μm in Fig. 5.11 (b). Using Eq.

(19) with a maximum strain value of ε_{mx}=0.00417, E_m=205.9GPa and the crack length based on the size of the corner element α=0.00005m, the calculated stress intensity factor is K_{mx}= 12.05MPa√m.

The number of cycles for the crack to propagate from an initial length, α_{in}=50μm to a final length α_f=250μm (Fig. 5.13) for a uniaxial, mode I problem under a stress ratio R=0.1 and a maximum stress of σmax=200MPa can be calculated by integrating a Paris-Erdogan crack growth law [139]:

$$\frac{d\alpha}{dN} = C(\Delta K)^m = C\left(Y\Delta\sigma\sqrt{\pi\alpha}\right)^m \Rightarrow \int_0^{N_f} dN = \int_{\alpha_{in}}^{\alpha_f} \frac{d\alpha}{CY^m\Delta\sigma^m(\pi\alpha)^{\frac{m}{2}}}$$

$$\therefore N_f = \frac{1}{CY^m\Delta\sigma^m\pi^{\frac{m}{2}}}\left[\frac{\alpha_f^{1-\frac{m}{2}} - \alpha_{in}^{1-\frac{m}{2}}}{1-\frac{m}{2}}\right] \quad (20)$$

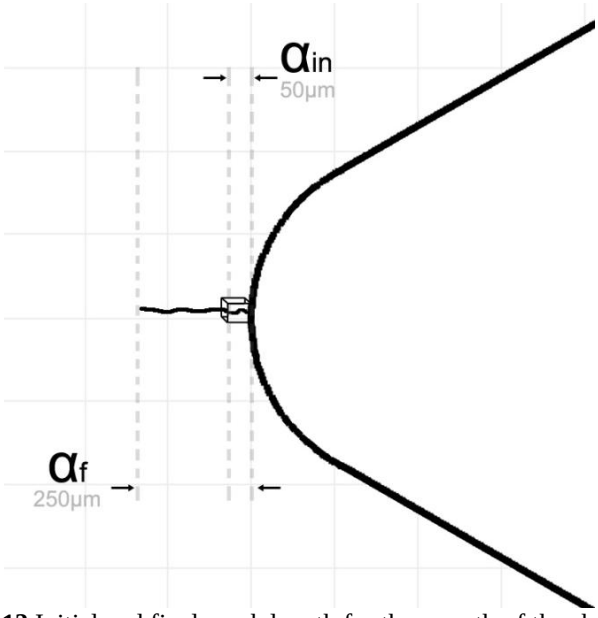

Figure 5.13 Initial and final crack length for the growth of the short crack.

The parameters C=1.81005e-13 and m=4.10051 for the TRIP700(B) steel have been taken from [140] and are used here under the assumption to be applicable for the short crack problem [130]. The "pseudostress" amplitude is Δσ=772MPa calculated from ε_m*E_m for R=0.1 and the free surface correction factor Y=1.12. Using the above values in Eq. (20), the

number of fatigue cycles for the crack to propagate to the critical length of 250μm is 12254 cycles. By adding the cycles calculated in section 5.6.1 for onset of the crack, the total fatigue life for development of a 250μm crack at the root of the notch is 92554 and 72754, with the Neuber and SED method respectively (Table 5.3) .

Table 5.3 Predicted fatigue life for the formation of a 250μm crack in TRIP700(B).

	Neuber	**SED**
Predicted fatigue life with FE calculations, for failure of a 50μm element, N_{ini} (cycles)	80300	60500
Crack advancement from 50μm to 250μm, N_{prop} (cycles)	12254	
Total fatigue life, N_f (cycles)	***92554***	***72754***

The problem of fatigue crack initiation assessment examined above is focused on sheet steel materials having a thickness under 2mm, which allows for the consideration of plane stress state. When the thickness increases, stress triaxiality effects can influence RA transformation [66, 114, 141-143] and hence the associated mechanical behaviour of TRIP steels.

By comparing the results of **Table** 5.3 with **Table** 5.2 it can be noticed that using the fracture mechanics approach in the present fatigue crack initiation analysis, the prediction of fatigue life for the onset of a 250 μm crack can be satisfactorily predicted.

5.6.3 RA transformation and fatigue crack growth

The fracture mechanics approach presented in section 5.6 can be modified appropriately, to support the inclusion of RA transformation, which has been found to influence fatigue crack initiation as well as crack growth. RA transformation is microstructurally accompanied by volume expansion [4-6] and may cause certain stress relaxation at the tip of a stress raiser due to the elastic surrounding material, thus extending the fatigue life prior to crack initiation. Additionally, phase transformation at the crack tip has been shown to be beneficial for fatigue

crack growth in a numerous studies [26-29, 91]. The main mechanism contributing to the retardation of crack growth is the stress relaxation imposed by the phase transformation during the volume change [6].

The above observation may be used to correlate the local stress relaxation with the induced crack closure, which reduces the effective driving force at the crack tip. Then an effective Stress Intensity Factor (SIF) range ΔK_{eff} (instead of the total range ΔK) in Eq. (20) may be obtained in the form:

$$\Delta K_{eff} = \Delta K_{max} - \Delta K_{op(TR)} \tag{21}$$

If an appropriate method is developed which allows for the experimental assessment of $\Delta K_{op(TR)}$ due to stress relaxation, the effective SIF range is a more reliable parameter for estimation of fatigue crack propagation. However the difficulty in the assessment of the SIF opening parameter is that it has to be carefully evaluated so that it can be distinguished from other mechanisms contributing to crack closure during fatigue crack growth (e.g. plasticity, surface roughness etc).

In that case, empirically, a quantification of the phase transformation effect on crack growth rate may be taken into account by using a modified expression of Eq. (21) first proposed by Elber [144] in the form:

$$\frac{d\alpha}{dN} = C\left(\Delta K_{eff}\right)^m = C\left(Y\Delta\sigma_{eff}\sqrt{\pi\alpha}\right)^m \tag{22}$$

where ΔK_{eff}, σ_{eff} are the effective values of SIF range and stress contributing to open crack surfaces. This analysis although not simple, is proposed as an idea for further investigation of the problem.

CHAPTER 6

Conclusions and Recommendations for further study

The effect of retained austenite transformation on the fatigue behaviour of Al- containing TRIP700 steels was investigated in the present Thesis. Transformation was quantitatively assessed under static loading as well as under different fatigue regimes including elastic and elastoplastic cyclic straining and its role on the materials tensile and cyclic properties was evaluated. The influence of characteristic microstructural parameters such as particle size and phase volume fraction was considered in the investigation. Furthermore, the crack initiation behavior of TRIP materials was investigated experimentally and analytically including a discussion of the role of RA transformation on the material behavior. The main findings of the investigation can be summarized in the following:

1) The tensile behavior is associated with the TRIP effect, which controls the magnitude of uniform elongation and thus necking in the material. A smaller RA particle size, which is

associated with higher stability against transformation, contributes to higher uniform elongation, delaying necking in the material. The delayed necking behavior is accompanied by a moderate strain hardening exponent (around the value 0.2) of TRIP materials. RA transformation potential is also related to the ferrite size. As the ferrite size increases the measured % RA transformation at fracture increases. Finally, a correlation seems to exist between RA transformation and strain hardening capacity with the materials having high % RA transformation exhibiting higher strain hardening exponents.

2) The high cycle fatigue behavior of TRIP steels is characterized by high fatigue limits, close to the materials' yield strength. The fatigue limit increases with decreasing % RA transformation indicating that fatigue behavior under elastic strains is superior in TRIP materials with low RA transformation levels. Under Low Cycle Fatigue conditions the trend is opposite. In the fatigue regime close to the transition life, where the plastic strain component is comparable to the elastic component, superior LCF performance seems to be related to higher amounts of RA transformation.
3) The cyclic behavior of TRIP steels is characterized by cyclic softening at small plastic strain amplitudes and a progressive transition to cyclic hardening at larger plastic strain amplitudes. Low levels of RA transformation under cyclic plastic strains were found to be associated with pronounced cyclic softening of the material.
4) Although there were no RA measurements at the fatigue crack initiation location in the present Thesis, from the material behavior observed, high resistance to fatigue crack initiation is obtained from TRIP (B) material with a moderately stable RA microstructure under cyclic strains, which promotes a progressive cyclic hardening mechanism. Materials exhibiting cyclic softening associated with less transformation potential as TRIP (A) steel, have been found to be less damage tolerant with regard to the notched fatigue behaviour.

5) The analytical results showed that existing fatigue models may be successfully combined with FE analysis at the tip of the notch to provide an improvement in the prediction of onset of a short crack at the notch root. A damage tolerance approach for the assessment of crack initiation at the notch root is also proposed with an option to extend the analysis for including the phase transformation effect in the assessment of fatigue crack growth.

6.1 Recommendations for further study

In this paragraph, some propositions for further study are included regarding the effect of RA transformation on fatigue and damage tolerance behaviour of TRIP steels. Ideas for further study may include:

a) Development of a quantitative correlation between the RA stability (through the determination of M_s^{σ} temperature), with microstructural features and the observed trends regarding the mechanical behavior of materials.

b) Investigation of the fatigue crack growth behavior in the medium ΔK regime, i) to obtain a more global view of the damage tolerance behavior of materials including short and long crack behavior and ii) to attempt an experimental assessment of the opening stress intensity range $\Delta K_{op(TR)}$ associated with the transformation effect.

c) Development of fatigue models in combination with point b) for the prediction of the transformation effect on fatigue crack growth rate of TRIP materials.

References

1. Ma, M. and H. Yi, *Lightweight Car Body and Application of High Strength Steels.* Advanced steels, 2011: p. 187-198.
2. Opbroek, E., *Advanced high strength steel application guidelines*. 2006, Technical report. International Iron and Steel Institute.
3. Cadoni, E., H. Pham, and T. Iwamoto, *An experimental investigation of energy absorption in TRIP steel under impact three-point bending deformation.* EPJ Web of Conferences, 2015. 94: p. 02004.
4. Sugimoto, K.-I., et al., *Effects of fine particle peening on fatigue strength of a TRIP-aided martensitic steel.* International Journal of Fatigue, 2017. 100: p. 206-214.
5. Sugimoto, K.I., M. Kobayashi, and S.-I. Yasuki, *Cyclic deformation behavior of a transformation-induced plasticity-aided dual-phase steel.* Metallurgical and Materials Transactions A, 1997. 28(12): p. 2637-2644.
6. Olson, G.B., *Transformation Plasticity and Toughening.* Le Journal de Physique IV, 1996. 06(C1): p. C1-407-C1-418.
7. Müller-Bollenhagen, C., M. Zimmermann, and H.J. Christ, *Very high cycle fatigue behaviour of austenitic stainless steel and the effect of strain-induced martensite.* International Journal of Fatigue, 2010. 32(6): p. 936-942.
8. Chatterjee, S., *Transformations in TRIP-assisted steels: microstructure and properties*. 2006, University of Cambridge.
9. Pyshmintsev, I.Y., et al., *The influence of the stress state on the plasticity of transformation induced plasticity-aided steel.* Metallurgical and Materials Transactions A, 2002. 33(6): p. 1659-1667.
10. Olson, G.B. and M. Azrin, *Transformation behavior of TRIP steels.* Metallurgical Transactions A, 1978. 9(5): p. 713-721.
11. Lacroix, G., *On the Relationships Between Microstructure and Mechanical Properties of TRIP-Assisted Multiphase Steels: Strength, Ductility, Fracture and Fatigue (Ph.D. Thesis)*. 2007, Université catholique de Louvain (UCL): Belgium.
12. Keeler, S. and M. Kimchi, *Advanced High Strength Steel (AHSS) Application Guidelines*, in *WorldAutoSteel Technical Report,v 5.0*. 2014.
13. Tamarelli, C.M., *AHSS 101-The Evolving Use of Advanced High-Strength Steels for Automotive Applications*. 2011: Steel Market Development Institute.
14. Hilditch, T., et al., *Role of microstructure in the low cycle fatigue of multi-phase steels.* Materials Science and Engineering a-Structural Materials Properties Microstructure and Processing, 2012. 534: p. 288-296.
15. Weidner, A., A. Glage, and H. Biermann, *In-situ characterization of the microstructure evolution during cyclic deformation of novel cast TRIP steel.* Procedia Engineering, 2010. 2(1): p. 1961-1971.
16. Glage, A., A. Weidner, and H. Biermann, *Effect of austenite stability on the low cycle fatigue behavior and microstructure of high alloyed metastable austenitic cast TRIPsteels.* Procedia Engineering, 2010. 2(1): p. 2085-2094.
17. Glage, A., et al., *Low cycle fatigue behavior and microstructure of a high alloyed metastable austenitic cast TRIP-steel.* 2009.
18. Hu, Z.G., P. Zhu, and J. Meng, *Fatigue properties of transformation-induced plasticity and dual-phase steels for auto-body lightweight: Experiment, modeling and application.* Materials & Design, 2010. 31(6): p. 2884-2890.

19. Dan, W.J., Z.G. Hu, and W.G. Zhang, *Influences of cyclic loading on martensite transformation of TRIP steels.* Metals and Materials International, 2013. 19(2): p. 251-257.
20. Kang, J., et al., *Low cycle fatigue behavior in a medium-carbon carbide-free bainitic steel.* Materials Science and Engineering: A, 2016. 666: p. 88-93.
21. Yokoi, T., et al., *Fatigue properties of high strength steels containing retained austenite.* JSAE Review, 1996. 17(2): p. 210-212.
22. Sugimoto, K.I., D. Fiji, and N. Yoshikawa, *Fatigue strength of newly developed high-strength low alloy TRIP-aided steels with good hardenability.* Procedia Engineering, 2010. 2(1): p. 359-362.
23. Abareshi, M. and E. Emadoddin, *Effect of retained austenite characteristics on fatigue behavior and tensile properties of transformation induced plasticity steel.* Materials & Design, 2011. 32(10): p. 5099-5105.
24. Haidemenopoulos, G.N., et al., *On the effect of austenite stability on high cycle fatigue of TRIP 700 steel.* Materials Science and Engineering: A, 2013. 573: p. 7-11.
25. Olson, G.B., et al., *Fatigue Strength of TRIP Steels.* Metallurgical Transactions A, 1980. 11(6): p. 1069-1071.
26. Nam, S.W., et al., *Fatigue Strength of Formable Ultra High-Strength TRIP-Aided Steels with Bainitic Ferrite Matrix* Key Engineering Materials, 2007: p. 247-250.
27. Jacques, P., et al., *On the role of martensitic transformation on damage and cracking resistance in TRIP-assisted multiphase steels.* Acta Materialia, 2001. 49(1): p. 139-152.
28. Hu, Z.Z., et al., *The effect of austenite on low cycle fatigue in three-phase steel.* International Journal of Fatigue, 1997. 19(8): p. 641-646.
29. Bhadeshia, H.K.D.H. and D.V. Edmonds, *Bainite in Silicon Steels: A New Composition-Property approach. Part I.* Metal Science, 1983. 17: p. 411-419.
30. Matsumura, O., Y. Sakuma, and H. Takechi, *Enhancement of elongation by retained austenite in intercritical annealed 0.4C-1.5Si-0.8Mn steel.* Transactions of the Iron and Steel Institute of Japan, 1987. 27(7): p. 570-579.
31. Jacques, P.J., *Transformation-induced plasticity for high strength formable steels.* Current Opinion in Solid State and Materials Science, 2004. 8(3-4): p. 259-265.
32. Kim, S.-J., et al., *Effects of heat treatment and alloying elements on the microstructures and mechanical properties of 0.15 wt pct C transformation-induced plasticity-aided cold-rolled steel sheets.* Metallurgical and Materials Transactions A, 2001. 32(3): p. 505-514.
33. Zhao, L., et al., *Influence of intercritical annealing temperature on phase transformations in a high aluminum TRIP steel*, in *International Conference on TRIP-Aided High Strength Ferrous Alloys,* B.C. De Cooman, Editor. 2002: Mainz. p. 141-145.
34. Ranjan, R., et al., *Thermo-mechanical Processing of TRIP-Aided Steels.* Metallurgical and Materials Transactions A, 2015. 46(7): p. 3232-3247.
35. Bleck, W., *Using the TRIP effect - the dawn of a promising group of cold formable steels*, in *International Conference on TRIP-Aided High Strength Ferrous Alloys*. 2002: Bad Harzburg, Germany. p. 13-23.
36. Girault, E., et al., *Comparison of the effects of silicon and aluminium on the tensile behaviour of multiphase trip-assisted steels.* Scripta Materialia, 2001. 44(6): p. 885-892.
37. De Cooman, B.C., *Structure–properties relationship in TRIP steels containing carbide-free bainite.* Current Opinion in Solid State and Materials Science, 2004. 8(3-4): p. 285-303.

38. Traint, S., et al., *Low-alloyed dual-phase and multiphase steel strip*, in *Steels and Materials for Power Plants*, P. Neumann, D. Allen, and E. Tenckhoff, Editors. 1999, Wiley-VCH Verlag GmbH & Co.: Weinheim. p. 71-76.
39. Meyer, M.D., D. Vanderschueren, and B.C.D. Cooman, *The Influence of the Substitution of Si by Al on the Properties of Cold Rolled C-Mn-Si TRIP Steels.* ISIJ International, 1999. 39(8): p. 813-822.
40. Timokhina, I.B., *The Microstructure and Mechanical Properties of Thermomechanically Processed TRansformation Induced Plasticity (TRIP) Steels*. 2003, Deakin University.
41. Bellhouse, E.M., A.I.M. Mertens, and J.R. McDermid, *Development of the surface structure of TRIP steels prior to hot-dip galvanizing.* Materials Science and Engineering: A, 2007. 463(1-2): p. 147-156.
42. Vasilakos, A.N., et al., *Low-alloy TRIP steels: A correlation between mechanical properties and the retained austenite stability.* Steel Research, 2002. 73(6-7): p. 249-252.
43. Mamalis, A.G. and G.N. Haidemenopoulos, *Aspects of ductility, toughness and formability of steel sheet in relation to transformation plasticity.* Journal of Materials Processing Technology, 1992. 30(2): p. 211-230.
44. Takahashi, M., *Development of High Strength Steels for Automobiles*, in *Nippon Steel Technical Report*. 2003. p. 2-7.
45. Dan, W.J., et al., *A model for strain-induced martensitic transformation of TRIP steel with strain rate.* Computational Materials Science, 2007. 40(1): p. 101-107.
46. Timokhina, I.B., P.D. Hodgson, and E.V. Pereloma, *Effect of microstructure on the stability of retained austenite in transformation-induced-plasticity steels.* Metallurgical and Materials Transactions a-Physical Metallurgy and Materials Science, 2004. 35A(8): p. 2331-2341.
47. Lee, C.G., et al., *Effects of volume fraction and stability of retained austenite on formability in a 0.1C-1.5Si-1.5Mn-0.5Cu TRIP-aided cold-rolled steel sheet.* Materials Science and Engineering a-Structural Materials Properties Microstructure and Processing, 2004. 371(1-2): p. 16-23.
48. Tamura, I., *Deformation-induced martensitic transformation and transformation-induced plasticity in steels.* Metal Science, 1982. 16: p. 245-253.
49. Shen, Y.F., et al., *Effects of retained austenite volume fraction, morphology, and carbon content on strength and ductility of nanostructured TRIP-assisted steels.* Materials Science and Engineering: A, 2015. 636: p. 551-564.
50. Cai, Z.H., et al., *Significance of control of austenite stability and three-stage work-hardening behavior of an ultrahigh strength–high ductility combination transformation-induced plasticity steel.* Scripta Materialia, 2013. 68(11): p. 865-868.
51. Shen, Y.F., et al., *Improved ductility of a transformation-induced-plasticity steel by nanoscale austenite lamellae.* Materials Science and Engineering: A, 2013. 583: p. 1-10.
52. Zhu, R., et al., *Phase constitution effect on the ductility of low alloy multiphase transformation induced plasticity steels.* Materials Science and Engineering: A, 2013. 569: p. 137-143.
53. Hatami, M.K., et al., *Towards ultra-high ductility TRIP-assisted multiphase steels controlled by strain gradient plasticity effects.* Journal of the Mechanics and Physics of Solids, 2017. 98: p. 201-221.
54. Reisner, G., et al., *The modeling of retained austenite in low-alloyed TRIP steels.* JOM, 1997. 49(9): p. 62-65.

55. Sakuma, Y., O. Matsumura, and O. Akisue, *Influence of C content and annealing temperature on microstructure and mechanical properties of 400◦C transformed steel containing retained austenite.* ISIJ International, 1991. 31(11): p. 1348–1353.
56. Varshney, A., et al., *Superior work hardening behavior of moderately high carbon low alloy super strong and ductile multiphase steels with dispersed retained austenite.* Materials & Design, 2016. 99: p. 439-448.
57. Glage, A., A. Weidner, and H. Biermann, *Cyclic Deformation Behaviour of Three Austenitic Cast CrMnNi TRIP/TWIP Steels with Various Ni Content.* steel research international, 2011. 82(9): p. 1040-1047.
58. Basuki, A. and E. Aernoudt, *Influence of rolling of TRIP steel in the intercritical region on the stability of retained austenite.* Journal of Materials Processing Technology, 1999. 89–90: p. 37-43.
59. Koh, H.J., et al., *Effect of Hot Rolling Conditions on the Microstructure and Mechanical Properties of Fe-C-Mn-Si Multiphase Steels.* Scripta Materialia, 1998. 38(5): p. 763-768.
60. Sugimoto, K.-i., et al., *Effects of Second Phase Morphology on RetainedAustenite Morphology and Tensile Properties in a TRIP-aided Dual-phase Steel Sheet.* ISIJ International, 1993. 33(7): p. 775-782.
61. Matsuda, H., et al. *Effect of Retained Austenite Stability on Mechanical Properties of 590MPa Grade TRIP Sheet Steels* in *6th International Conference on Processing and Manufacturing of Advanced Materials – THERMEC*. 2010.
62. Chiang, J., J.D. Boyd, and A.K. Pilkey, *Effect of microstructure on retained austenite stability and tensile behaviour in an aluminum-alloyed TRIP steel.* Materials Science and Engineering: A, 2015. 638: p. 132-142.
63. Jacques, P.J., et al., *Multiscale mechanics of TRIP-assisted multiphase steels: I. Characterization and mechanical testing.* Acta Materialia, 2007. 55(11): p. 3681-3693.
64. Lacroix, G., et al., *Influence of Retained Austenite on The Fracture Strain and Toughness in TRIP-Assisted Multiphase Steels*. 2003.
65. Furnémont, Q., F. Delannay, and P.J. Jacques, *Experimental investigation of the influence of the stress state on the mechanical stability of austenite in multiphase steels.* Journal de Physique IV (Proceedings), 2003. 112: p. 421-424.
66. Yu, H.Y., G.Y. Kai, and M. De Jian, *Transformation behavior of retained austenite under different deformation modes for low alloyed TRIP-assisted steels.* Materials Science and Engineering: A, 2006. 441(1-2): p. 331-335.
67. Lani, F., et al., *Multiscale mechanics of TRIP-assisted multiphase steels: II. Micromechanical modelling.* Acta Materialia, 2007. 55(11): p. 3695-3705.
68. Soliman, M. and H. Palkowski, *On Factors Affecting the Phase Transformation and Mechanical Properties of Cold-Rolled Transformation-Induced-Plasticity–Aided Steel.* Metallurgical and Materials Transactions A, 2008. 39(10): p. 2513-2527.
69. Godet, S., et al., *Effect of hot-rolling conditions on the tensile properties of multiphase steels exhibiting a TRIP effect.* Steel Research, 2002. 73(6-7): p. 280-286.
70. Blondé, R., et al., *Mechanical stability of individual austenite grains in TRIP steel studied by synchrotron X-ray diffraction during tensile loading.* Materials Science and Engineering: A, 2014. 618: p. 280-287.
71. Zhou, Q., et al., *Low-cycle fatigue behavior and microstructural evolution in a low-carbon carbide-free bainitic steel.* Materials & Design, 2015. 85: p. 487-496.
72. Ackermann, S., et al., *Biaxial in-phase and out-of-phase cyclic deformation and fatigue behavior of an austenitic TRIP steel.* International Journal of Fatigue, 2014. 67: p. 123-133.

73. Man, J., et al., *Stability of austenitic 316L steel against martensite formation during cyclic straining.* Procedia Engineering, 2011. 10: p. 1279-1284.
74. Topic, M., R. Tait, and C. Allen, *The fatigue behaviour of metastable (AISI-304) austenitic stainless steel wires.* International Journal of Fatigue, 2007. 29(4): p. 656-665.
75. Basu, K., et al., *Effect of grain size on austenite stability and room temperature low cycle fatigue behaviour of solution annealed AISI 316LN austenitic stainless steel.* Materials Science and Technology, 2007. 23(11): p. 1278-1284.
76. Grosse, M., et al., *Influencing parameters on martensite transformation during low cycle fatigue for steel AISI 321.* Materials Science and Engineering: A, 2006. 437(1): p. 109-113.
77. Baudry, G. and A. Pineau, *Influence of strain-induced martensitic transformation on the low-cycle fatigue behavior of a stainless steel.* Materials Science and Engineering: A, 1977. 28(2): p. 229-242.
78. Smaga, M., F. Walther, and D. Eifler, *Deformation-induced martensitic transformation in metastable austenitic steels.* Materials Science and Engineering: A, 2008. 483-484: p. 394-397.
79. Hilditch, T.B., et al., *Cyclic Deformation of Advanced High-Strength Steels: Mechanical Behavior and Microstructural Analysis.* Metallurgical and Materials Transactions A, 2009. 40(2): p. 342-353.
80. Franke, G. and C. Altstetter, *Low_Cycle Fatigue Behavior of Mn-N Stainless Steels.* Metallurgical Transactions A, 1976. 7A: p. 1719-1727.
81. Yu, D., et al., *Revealing the cyclic hardening mechanism of an austenitic stainless steel by real-time in situ neutron diffraction.* Scripta Materialia, 2014. 89: p. 45-48.
82. Sugimoto, K.I., *Fracture strength and toughness of ultra high strength TRIP aided steels.* Materials Science and Technology, 2009. 25(9): p. 1108-1117.
83. Sugimoto, K., et al., *Fatigue-hardening Behavior of TRIP-aided Bainitic Steels.* Tetsu-to-Hagane, 1999. 85(11): p. 856-862.
84. Song, S.-M., et al., *Effects of Prestraining on High-Cycle Fatigue Strength of High-Strength Low Alloy TRIP-Aided Steels.* Journal of the Society of Materials Science, Japan, 2003. 52(9Appendix): p. 223-229.
85. Zhao, P., et al., *The significance of ultrafine film-like retained austenite in governing very high cycle fatigue behavior in an ultrahigh-strength MN–SI–Cr–C steel.* Materials Science and Engineering: A, 2015. 645: p. 116-121.
86. Yoshikawa, N., J. Kobayashi, and K. Sugimoto, *Notch-Fatigue Properties of Advanced TRIP-Aided Bainitic Ferrite Steels.* Metallurgical and Materials Transactions a-Physical Metallurgy and Materials Science, 2012. 43A(11): p. 4129-4136.
87. Diego-Calderón, I.d., et al., *Effect of microstructure on fatigue behavior of advanced high strength steels produced by quenching and partitioning and the role of retained austenite.* Materials Science and Engineering: A, 2015. 641: p. 215-224.
88. Huo, C.Y. and H.L. Gao, *Strain-induced martensitic transformation in fatigue crack tip zone for a high strength steel.* Materials Characterization, 2005. 55(1): p. 12-18.
89. Krupp, U., C. West, and H.J. Christ, *Deformation-induced martensite formation during cyclic deformation of metastable austenitic steel: Influence of temperature and carbon content.* Materials Science and Engineering: A, 2008. 481-482: p. 713-717.
90. Roth, I., et al., *Crack initiation and short crack growth in metastable austenitic stainless steel in the high cycle fatigue regime.* Procedia Engineering, 2010. 2(1): p. 941-948.
91. Cheng, X., et al., *Fatigue crack growth in TRIP steel under positive R-ratios.* Engineering Fracture Mechanics, 2008. 75(3-4): p. 739-749.

92. De, A.K., J.G. Speer, and D.K. Matlock, *Color tint-etching for multiphase steels.* Advanced Materials & Processes, 2003. 161(2): p. 27-30.
93. Girault, E., et al., *Metallographic Methods for Revealing the Multiphase Microstructure of TRIP-Assisted Steels.* Materials Characterization, 1998. 40(2): p. 111-118.
94. Russ, J.C., *The Image Processing Handbook*. Sixth ed. 2011, Boca Raton FL: CRC Press.
95. E. Wirth, et al. *Determination of the volume amount of retained austenite and ferrite in small specimens by magnetic measurements*. in *Proc. Int. Conf. on TRIPaided High Strength Ferrous Alloys*. 2002. Ghent, Belgium.
96. Ramberg, W. and W.R. Osgood, *(1943) Description of stress–strain curves by three parameters. National advisory committee for aeronautics (reprinted Rasmussen KJR. Full-range stress–strain curves for stainless steel alloys.* Journal of Constructional Steel Research, 2003. 59(1): p. 47-61.
97. SEP(1240), *Testing and Documentation Guideline for the Experimental Determination of Mechanical Properties of Steel Sheets for CAE Calculations.* 1st edn., 2006. Institute VDEh, Dusseldorf, Germany.
98. Noda, N.A. and H. Nisitani, *Stress concentration of a strip with a single edge notch.* Engineering Fracture Mechanics, 1987. 28(2): p. 223-238.
99. Li, Z. and D. Wu, *Influence of hot rolling conditions on the mechanical properties of hot rolled TRIP steel.* Journal of Wuhan University of Technology-Mater. Sci. Ed., 2008. 23(1): p. 74-79.
100. Callister, W.D. and D.G. Rethwisch, *Materials Science and Engineering: An Introduction*. 2009: John Wiley & Sons.
101. Godet, S., P. Harlet, and P.J. Jacques, *Grain Refinement of TRIP-Assisted Multiphase Steels through Strain-Induced Phase Transformation.* steel research international, 2006. 77(4): p. 271-275.
102. Yu, Q.B., *Effect of Ferrite Grain Size on the Yield-Strength Ratio of Low-Carbon Alloy Steel.* Advanced Materials Research 2012. 535-537: p. 545-548
103. Zhang, J., et al., *Enhanced stability of retained austenite and consequent work hardening rate through pre-quenching prior to quenching and partitioning in a Q–P microalloyed steel.* Materials Science and Engineering: A, 2014. 611: p. 252-256.
104. Takahashi, M., et al., *High Strength Hot-rolled Steel Sheets for Automobiles*, in *Nippon Steel Technical Report*. 2003. p. 8-12.
105. Chiang, J., et al., *Effect of microstructure on retained austenite stability and work hardening of TRIP steels.* Materials Science and Engineering: A, 2011. 528(13-14): p. 4516-4521.
106. Jimenez-Melero, E., et al., *Martensitic transformation of individual grains in low-alloyed TRIP steels.* Scripta Materialia, 2007. 56(5): p. 421-424.
107. Mark, A.F.L., *Microstructural effects on the stability of retained austenite in transformation induced plasticity steels*. 2008, Queen's University.
108. Ennis, B.L., et al., *Metastable austenite driven work-hardening behaviour in a TRIP-assisted dual phase steel.* International Journal of Plasticity, 2017. 88: p. 126-139.
109. de Diego-Calderón, I., et al., *Deformation behavior of a high strength multiphase steel at macro- and micro-scales.* Materials Science and Engineering: A, 2014. 611: p. 201-211.
110. Dowling, N.E., *Mechanical Behavior of Materials: Engineering Methods for Deformation, Fracture, and Fatigue*. 3rd ed. 2006: Prentice Hall.
111. Lucas, J.P. and W.W. Gerberich, *Cyclic strain hardening of polygonal and acicular ferrite/bainite microstructures in microalloyed steels in the temperature range − 150°C to 27°C.* International Journal of Fatigue, 1985. 7(1): p. 31-38.

112. Ye, D., et al., *The low-cycle fatigue, deformation and final fracture behaviour of an austenitic stainless steel.* Materials Science and Engineering: A, 2006. 415(1–2): p. 104-117.
113. Bellas, I.I., *Study of strain-induced transformation in low-alloy TRIP steels (M.Sc. Thesis)*, in *Department of Mechanical Engineering*. 2015, University of Thessaly: Greece.
114. Zhou, Q., et al., *Inconsistent effects of mechanical stability of retained austenite on ductility and toughness of transformation-induced plasticity steels.* Materials Science and Engineering: A, 2013. 578: p. 370-376.
115. Song, C., et al., *The stability of retained austenite at different locations during straining of I&Q&P steel.* Materials Science and Engineering: A, 2016. 670: p. 326-334.
116. Wang, J.J. and S. van der Zwaag, *Stabilization mechanisms of retained austenite in transformation-induced plasticity steel.* Metallurgical and Materials Transactions a-Physical Metallurgy and Materials Science, 2001. 32(6): p. 1527-1539.
117. Suresh, S., *Fatigue of Materials (Cambridge Solid State Science Series)*. Second ed. 1998: Cambridge University Press.
118. James, M.N., C. Dimitriou, and H.D. Chandler, *Low cycle fatigue lives of notched components.* Fatigue & Fracture of Engineering Materials & Structures, 1989. 12(3): p. 213-225.
119. Manson, S. and M. Hirschberg. *Crack initiation and propagation in notched fatigue specimens*. in *Proceedings of the First International Conference on Fracture*. 1966.
120. Guo, Y., et al., *Controlling deformation and microstructure on machined surfaces.* Acta Materialia, 2011. 59(11): p. 4538-4547.
121. Jeelani, S. and K. Ramakrishnan, *Subsurface plastic deformation in machining 6Al-2Sn-4Zr-2Mo titanium alloy.* Wear, 1983. 85(1): p. 121-130.
122. Jeelani, S. and K. Ramakrishnan, *Subsurface plastic deformation in machining annealed 18% Ni maraging steel.* Wear, 1982. 81(2): p. 263-273.
123. Uthaisangsuk, V., U. Prahl, and W. Bleck, *Modelling of damage and failure in multiphase high strength DP and TRIP steels.* Engineering Fracture Mechanics, 2011. 78(3): p. 469-486.
124. Fatemi, A. and Z. Zeng, *Elasto-plastic stress and strain behaviour at notch roots under monotonic and cyclic loadings.* The Journal of Strain Analysis for Engineering Design, 2001. 36(3): p. 287-300.
125. Ye, D., O. Hertel, and M. Vormwald, *A unified expression of elastic–plastic notch stress–strain calculation in bodies subjected to multiaxial cyclic loading.* International Journal of Solids and Structures, 2008. 45(24): p. 6177-6189.
126. Topper, T., R. Wetzel, and J. Morrow, *Neuber's rule applied to fatigue of notched specimens.* Journal of materials 1969. 4(1): p. 200-209.
127. Molski, K. and G. Glinka, *A method of elastic-plastic stress and strain calculation at a notch root.* Materials Science and Engineering, 1981. 50(1): p. 93-100.
128. Glinka, G., W. Ott, and H. Nowack, *Elastoplastic Plane Strain Analysis of Stresses and Strains at the Notch Root.* Journal of Engineering Materials and Technology, 1988. 110(3): p. 195-204.
129. Sharpe, J.W.N., C.H. Yang, and R.L. Tregoning, *An Evaluation of the Neuber and Glinka Relations for Monotonic Loading.* Journal of Applied Mechanics, 1992. 59(2S): p. S50-S56.
130. Stephens, R.I., et al., *Metal Fatigue in Engineering*. 2nd ed. 2000: Wiley-Interscience.
131. Smith, K.N., P. Watson, and T.H. Topper, *A stress-strain function for the fatigue of metals.* Journal of Materials, 1970. 4: p. 767-778.

132. Suresh, S. and R.O. Ritchie, *Propagation of short fatigue cracks.* International Materials Reviews, 1984. 29(1): p. 445-475.
133. Leis, B.N., *Displacement controlled fatigue crack growth in inelastic notch fields: Implications for short cracks.* Engineering Fracture Mechanics, 1985. 22(2): p. 279-293.
134. Dugdale, D.S., *Yielding of steel sheets containing slits.* Journal of the Mechanics and Physics of Solids, 1960. 8(2): p. 100-104.
135. El Haddad, M.H., K.N. Smith, and T.H. Topper, *Fatigue Crack Propagation of Short Cracks.* Journal of Engineering Materials and Technology, 1979. 101(1): p. 42-46.
136. El Haddad, M.H., K.N. Smith, and T.H. Topper. *A Strain Based Intensity Factor Solution for Short Fatigue Cracks Initiating from Notches*. in *Smith CW (ed) Fracture mechanics: Proceedings of the eleventh national symposium on fracture mechanics: part I, ASTM STP 677*. 1979.
137. Ahmad, H.Y. and J.R. Yates, *An Elastic-Plastic Model for Fatigue Crack Growth at Notches.* Fatigue & Fracture of Engineering Materials and Structures, 1994. 17(6): p. 651-660.
138. Leis, B.N. *Microcrack initiation and growth in a pearlitic steel - Experiment and analysis*. in *15th National Fracture Symposium*. 1982. University of Maryland.
139. Paris, P. and F. Erdogan, *A critical analysis of crack propagation laws.* Journal of Fluids Engineering, 1963. 85(4): p. 528-533.
140. Gonidakis, S., *The effect of heat treatment procedure in fracture behavior of aluminum containing TRIP steel (M.Sc. Thesis)*, in *Department of Mechanical Engineering*. 2017, University of Thessaly: Greece.
141. Blondé, R., et al., *The mechanical stability of retained austenite in low-alloyed TRIP steel under shear loading.* Materials Science and Engineering: A, 2014. 594: p. 125-134.
142. Lani, F., et al. *On the stress-dependence of the TRIP-effect in multiphase steels*. in *8th ESAFORM Conference on material forming*. 2008. Cluj, Romania.
143. Haidemenopoulos, G.N., N. Aravas, and I. Bellas, *Kinetics of strain-induced transformation of dispersed austenite in low-alloy TRIP steels.* Materials Science and Engineering: A, 2014. 615: p. 416-423.
144. Elber, W. *The significance of fatigue crack growth* in *ASTM STP*. 1971.